1-1-2016

Finite Element and Probabilistic Analysis of Soft Tissue Structures of the Human Lumbar Spine

Dana Joseph Coombs
University of Denver

Finite Element and Probabilistic Analysis of Soft Tissue Structures of the Human Lumbar Spine

Abstract

Human lumbar spine mechanics are influenced by soft tissue structures. Understanding and properly modeling these structures can help determine pathology, treatment, and implant design and performance. Finite element models of the L4-L5 level of the lumbar spine are often used, which include a representation of the intervertebral disc and spinal ligaments. Validation of these models are typically based on torque rotation data from a single subject or the models use average properties reported in literature. However, experimental testing reports variation up to 40% in ligament stiffness and even greater variability for annulus fibrosis properties. Probabilistic approaches enable consideration of the impact of intersubject variability on model outputs. However, they often require lengthy computation times.

The first objective of this dissertation was to develop a methodology to better calibrate constitutive models of the disc using displacement data of intradiscal points across the mid-transverse plane of an L4-L5 lumbar spine disc in addition to kinematics. It was hypothesized that this will result in a more accurate constitutive model. The second objective was to develop a comprehensive probabilistic representation to characterize variability in the parameters describing the soft tissue structures and to develop efficient Monte Carlo simulations methods of a finite element model of the L4-L5 functional spinal unit.

The data used to calibrate constitutive models at intradiscal points across the disc was collected from compression, extension, flexion, and lateral bending. Optimization was used to calibrate the model parameters. Constitutive model types and the number of zones were compared. The best combination was a linear elastic constitutive model representing the nucleus pulposis and a Holzapfel-Gasser-Ogden model representing the annulus fibrosis divided into anterior, right lateral, left lateral, and posterior zones. The probabilistic representation of the ligaments and disc was determined based on direct mechanical test data as found in the literature. A single stiffness parameter was defined to characterize each ligament, with the anterior longitudinal ligament being the stiffest, while the posterior longitudinal ligament and interspinous ligament had the greatest coefficient of variation of 0.65 and 0.64, respectively. The posterior portion of the annulus fibrosis had the greatest stiffness and greatest variation up to 300% in circumferential loading. This probabilistic representation was used to evaluate the Sobol and descriptive variance reduction sampling methods, which were assessed for efficiency and accuracy in comparison to traditional random Monte Carlo sampling. Comparisons were based on output torque-rotation curves at the 10th and 90th percentile for flexion, extension, axial rotation, and lateral bending. The descriptive sampling technique best matched the random sampling technique, at the extremes of rotation, with a 3.6% mean difference. This was achieved with a 10X reduction in the number of iterations and computation time.

Applications of a more accurately calibrated constitutive model of the NP and AF could be the development of nucleus replacement materials that more closely match the natural NP and prediction of activities which could cause disc herniation. The resulting probabilistic representation can be utilized to include intersubject variability in biomechanics evaluations. The improvements in efficiency of Monte Carlo simulations enable intersubject variability to be considered in a variety of biomechanical evaluations, including design-phase screening of orthopedic implants.

Document Type

Dissertation

FINITE ELEMENT AND PROBABILISTIC ANALYSIS OF SOFT TISSUE STRUCTURES OF THE HUMAN LUMBAR SPINE

A Dissertation

Presented to

The Faculty of

the Daniel Felix Ritchie School of Engineering and Computer Science

University of Denver

In Partial Fulfillment

of the Requirements for the Degree

Doctor of Philosophy

---

by

Dana Joseph Coombs

March 2016

Advisor: Dr. Paul J. Rullkoetter

Author: Dana J. Coombs
Title: FINITE ELEMENT AND PROBABILISTIC ANALYSIS OF SOFT TISSUE STRUTURES OF THE HUMAN LUMBAR SPINE
Advisor: Dr. Paul J. Rullkoetter
Degree Date: March 2016

ABSTRACT

Human lumbar spine mechanics are influenced by soft tissue structures. Understanding and properly modeling these structures can help determine pathology, treatment, and implant design and performance. Finite element models of the L4-L5 level of the lumbar spine are often used, which include a representation of the intervertebral disc and spinal ligaments. Validation of these models are typically based on torque rotation data from a single subject or the models use average properties reported in literature. However, experimental testing reports variation up to 40% in ligament stiffness and even greater variability for annulus fibrosis properties. Probabilistic approaches enable consideration of the impact of intersubject variability on model outputs. However, they often require lengthy computation times.

The first objective of this dissertation was to develop a methodology to better calibrate constitutive models of the disc using displacement data of intradiscal points across the mid-transverse plane of an L4-L5 lumbar spine disc in addition to kinematics. It was hypothesized that this will result in a more accurate constitutive model. The second objective was to develop a comprehensive probabilistic representation to characterize variability in the parameters describing the soft tissue structures and to develop efficient Monte Carlo simulations methods of a finite element model of the L4-L5 functional spinal unit.

The data used to calibrate constitutive models at intradiscal points across the disc was collected from compression, extension, flexion, and lateral bending. Optimization was used

to calibrate the model parameters. Constitutive model types and the number of zones were compared. The best combination was a linear elastic constitutive model representing the nucleus pulposis and a Holzapfel-Gasser-Ogden model representing the annulus fibrosis divided into anterior, right lateral, left lateral, and posterior zones. The probabilistic representation of the ligaments and disc was determined based on direct mechanical test data as found in the literature. A single stiffness parameter was defined to characterize each ligament, with the anterior longitudinal ligament being the stiffest, while the posterior longitudinal ligament and interspinous ligament had the greatest coefficient of variation of 0.65 and 0.64, respectively. The posterior portion of the annulus fibrosis had the greatest stiffness and greatest variation up to 300% in circumferential loading. This probabilistic representation was used to evaluate the Sobol and descriptive variance reduction sampling methods, which were assessed for efficiency and accuracy in comparison to traditional random Monte Carlo sampling. Comparisons were based on output torque-rotation curves at the 10th and 90th percentile for flexion, extension, axial rotation, and lateral bending. The descriptive sampling technique best matched the random sampling technique, at the extremes of rotation, with a 3.6% mean difference. This was achieved with a 10X reduction in the number of iterations and computation time.

Applications of a more accurately calibrated constitutive model of the NP and AF could be the development of nucleus replacement materials that more closely match the natural NP and prediction of activities which could cause disc herniation. The resulting probabilistic representation can be utilized to include intersubject variability in biomechanics evaluations. The improvements in efficiency of Monte Carlo simulations enable intersubject variability to be considered in a variety of biomechanical evaluations, including design-phase screening of orthopedic implants.

ACKNOWLEDGEMENTS

I am very thankful for all the time, guidance, wisdom, and encouragement that I received from Dr. Paul J. Rullkoetter and Dr. Peter J. Laz. I am grateful for the relationship that developed while being a student and also continuing to work on spine research and trauma orthopedic research. This PhD started when Dr. Laz suggested that I register for and complete a PhD program while working on spine research at the University of Denver that was sponsored by Synthes Spine. I would like to thank Dr. Anthony Tsantrizos for his time, effort, encouragement, and sharing data from his PhD research. I am also thankful to Dr. Milind Rao for providing files, data, and answering questions based on FSU model developed during his PhD research. I am grateful to Synthes Spine for funding this PhD program. Finally, I would like to thank my wife and two daughters who encouraged me and helped me balance the time to be a husband, father, full time employee, and student while also doing many other activities.

TABLE OF CONTENTS

LIST OF FIGURES

LIST OF TABLES

CHAPTER 1 - INTRODUCTION

The intervertebral disc (IVD) has many functions in the human lumbar spine. It mostly carries compressive loads during activities of daily living. However, other loads can be applied to the IVD such as tension and shear due to certain motions of flexion, extension, lateral bending, and axial rotation. Combined loads can occur with combined motions. Short duration, high amplitude loads (such as a traumatic event) can cause failure of the IVD. The behavior and properties of the IVD tissue is rate dependent. However, long duration, low level loads can also cause a fatigue failure of the IVD (White and Panjabi, 1990). In addition, degeneration is age dependent. Miller et al. (Miller et al., 1988) visually graded lumbar IVD's for degeneration on a scale from 1 to 4. They concluded that degeneration starts in males in their 20's and in females in their 30's. They also concluded that by age 50, 97% of all IVD's are degenerated and the most degenerated segments are L3-L4, L4-L5, and L5-S1. With continued loading, the nucleus pulposis (NP) can herniate through the weakened annulus fibrosis (AF). Disc herniation can be classified relative to the location in the spinal canal; central, paracentral, foraminal, or far lateral. The most common location is paracentral (Shapiro et al. 2014), and L4-L5 is one of the most commonly treated level for disc herniation and disc degeneration (Humphreys et al, 1999). The clinical issues associated with disc degeneration and herniation has led to the development of spinal implants such as fusion

systems containing spacers, pedicle screws, and rods. Motion preservation implants replace the IVD as a total joint system and nucleus replacements replace the NP.

A motion preservation device replaces the diseased disc with a synthetic joint. The goal is to restore healthy kinematic motion as closely as possible and eliminate pain. Two examples of total disc implants are Charite (formerly DePuy Spine Inc., Raynham, MA) and ProDisc L (formerly Synthes, West Chester, PA). Each implant has a different design, but both have a ball-in-socket feature with a fixed center of rotation.

The nucleus replacement approach is less invasive since less native tissue is removed and replaced. The goal is to restore the healthy biomechanical function of the disc while removing pain. It can be applied earlier in the disc degeneration process while the AF is not severely damaged. Several companies have introduced nucleus replacement materials such as polycarbonate urethane elastomer, semicrystalline polyvinyl alcohol, hydrogel, and polyurethane. Some of these materials are injectable. This technology has had many clinical challenges and many companies have stopped selling nucleus replacement or are no longer in business. One company that still offers an injectable hydrogel is SpineWave (Shelton, CT).

1.1 Aims and Objective of this Work

There are three main aims of this dissertation. The first is to provide a methodology to define better constitutive models of the IVD for the use of finite element (FE) models. The second is to characterize the uncertainty of the parameters that define the soft tissue structures (IVD and ligaments) of an L4-L5 functional spinal unit. The third is to

determine an efficient method to perform probabilistic studies and measure the uncertainly of output parameters of an L4-L5 functional spinal unit.

For the first aim, constitutive models were based on experimental data which included the displacement of intradiscal points during flexion, extension, lateral bending, and simple compression. This was in addition to the rotation data. Having a more accurate definition of constitutive models could provide a way to more accurately measure strain or stress in the NP and AF. This could be useful to determine if certain loads or activities of daily living could cause herniation or failure of the AF. Shirazi- Adl (Shirazi-Adl, 1989) provided an early estimate of failure limits of the annulus, showing that asymmetric lifting with bending and rotation produces annulus fiber strains over 20%. Fiber rupture initiated in the inner posterolateral annulus and propagated as a radial tear. FE models can provide a measure of strains and be used to predict AF failure. A more accurate constitutive model of the AF would provide detailed information around damaged tissue after an AF repair, using suturing techniques (Cuterl et al. 2013). Another important application is to use the constitutive model to develop nucleus replacement materials that better match intact, healthy NP tissue.

The second and third aims allow for a probabilistic representation of the soft tissues in an FE model of an L4-L5 FSU. This allows spinal implant designs to be efficiently evaluated over a population based on measures related to the implants. Examples include stress or strain in the implant, kinematic evaluation for motion preserving implants, and positioning of the implant in the spinal anatomy.

CHAPTER 2 – BACKGROUND & MOTIVATION

This chapter provides a basic background on human lumbar spine anatomy, biomechanics of the lumbar spine, and the computational methods used in this dissertation. Specific background and literature review on the different topics are included in their respective sections.

2.1 Anatomy and Biomechanics of the Lumbar Spine

It is important to first define anatomical directions and planes to help distinguish anatomy. The anterior direction points toward the front, the posterior direction points toward the back. The superior direction points toward the head or above another part, the inferior direction points toward the feet or below another part. The medial direction points towards the midline of the body from the left or right side, the lateral direction points away from the midline to the left or right (Fig. 2.1). The transverse plane divides the body into top and bottom, the frontal plane divides the body into front and back, and the sagittal plane divides the body into left and right.

The vertebral column is composed of vertebrae, discs, ligaments, and muscles. The basic function of the spine is to provide mobility and stability of the torso. The vertebral column also protects the spinal cord and nerve roots. The lumbar spine contains 5 vertebrae called L1, L2, L3, L4, and L5, from superior to inferior (Fig 2.2). The L5 vertebra is connected to the sacrum and L1 is connected to the thoracic spine. The lumbar spine has a lordotic curve in a lateral view. The lordotic curve is defined as the

convexity of the spine pointing anteriorly. This curve allows shock absorption during axial loading.

The boney anatomy of each vertebra can be categorized in two main parts. The solid anterior portion called a vertebral body and a posterior arch. The vertebral body is the largest part. The superior and inferior surfaces connect to the discs. It is composed of spongy cancellous bone with a thin layer of dense cortical bone. The posterior arch is made of the pedicle, lamina, spinous process, transverse process, and articular processes (Fig. 2.3). There are two superior articular processes, and two inferior articular processes. Each have articulating surfaces with cartilage called facets. The facet orientation in the lumbar spine resists axial rotation, but allows flexion and extension and some lateral bending.

The ligamentous structure of the spine provides stability. There are seven major ligaments in the lumbar spine; the anterior longitudinal ligament (ALL), posterior longitudinal ligament (PLL), supraspinous ligament (SSL), interspinous ligament (ISL), ligamentum flavum (LFL), intertransverse ligament (ITL), and facet capsule (FCL). The ALL begins at the occipital bone and is attached to the anterior surface of all the vertebrae. The PLL runs over all the posterior surfaces of the vertebral bodies. The ALL and PLL stabilize the spine in flexion and extension. The SSL attaches the tip of each spinous process. The ISL connects between each spinous process. The ligmantum flavum is also known as the yellow ligament and connects the borders of the lamina. It has lots of elastic fibers and is the most purely elastic tissue in the human body (Fig. 2.4).

The intervertebral discs are fibrocartilagenous structures that represent about one quarter of the height of the spine. Their function is to absorb and distribute force. The

disc is made of two main structures; the soft gel-like center is the nucleus pulposis (NP), and the tough outer ring is called the annulus fibrosis (AF). The AF contains rings of fibers that alternate direction relative to the transverse plane of the disc. It is thicker in the anterior region (White and Panjabi, 1990).

2.2 Implicit Finite Element Analysis

Finite element analysis (FEA) was used in each of the topics in this dissertation. This method solves the spatial distribution of a measure such as stress, strain, and displacement. In many situations a closed form, analytical solution cannot be determined because of complex geometry. A finite element model represents the geometry with discrete, finite elements. The spatial distribution of the measure in each element is can be determined. Elements are connected at nodes and the combined elements are defined as a mesh. The number of elements in the mesh can directly affect how closely the FEA model matches the true solution. A process of mesh refinement can be used to converge closer to the true solution.

The general FEA process includes the following steps (Logan et al. 1992). This example assumes the spatial distribution measure is displacement, stress, and strain.

1. Define the mesh and select element types
2. Select a displacement function. This function is defined within the element using the nodal values of the elements.
3. Define the strain-displacement and stress-strain relationships. The stress-strain relationship is also called the constitutive law.

4. Derive the element stiffness matrix and equations, which relates the nodal displacement to the nodal forces.
5. Assemble the element equations to obtain the global equations, which include the global stiffness matrix. Boundary conditions are used to define some of nodal forces and displacements in the matrices.
6. Solve for the unknown degrees of freedom in the displacement vector using an elimination numerical method.
7. Solve for the element strains and stresses based on relationships defined in step 3.

An implicit solver was used for the models in this dissertation. All of the models contained a non-linear, hyperelastic constitutive model to represent part of the disc. In nonlinear implicit analysis, the solution requires a series of trial solutions (iterations) to establish equilibrium between the externally applied loads and the nodal point forces within a certain tolerance. Each trial solution adds a small amount of force or displacement to the boundary conditions. Convergence of the force equilibrium and the number and size of the iterations is determined by using a Newton-Raphson method (Cook et al. 2002).

2.3 Probabilistic Methods

Spine biomechanics contain uncertainty, such anthropometry, kinematics, loading, and material properties, causing variability in output parameters. A deterministic approach does not offer any information on the sensitivity of output parameters to the input parameters. This section provides a brief overview of the probabilistic methods using in this dissertation.

In probabilistic analyses, input parameters are represented as distributions to determine a distribution of output parameters. The probability density function (PDF) is a function that describes the probability for a random parameter to have a certain value (Fig. 2.5) (Haldar et al., 2000 P.38). The area under the PDF curve for some interval gives the probability that the parameter will lie within that interval. The cumulative distribution function (CDF) is the integral of the PDF and determines the probability of the parameter occurring at or below a specified value (Figure 2.5). The PDF indicates the nature of the randomness. To calculate the probability of the parameter having a value between two numbers, the area under the PDF between these two limits needs to be calculated. The CDF always ranges in value from 0 to 1, representing a 0% probability at the lower bound and a 100% probability at the upper bound (Haldar et al. 2000).

A commonly applied probabilistic approach is the Monte Carlo simulation method. This method randomly simulates the process, using the stochastic properties of the input parameter by using the input parameter's CDF to determine the value of the parameter from the PDF. The output parameters are calculated for each trial. This is done for a number of trials to represent the variability in the input parameters and determine the variability in the output parameters. The Monte Carlo method will converge to the correct solution if enough trials are used.

Three sampling techniques were used in this dissertation. The traditional random sampling technique generates a large sample of uniformly distributed random numbers between 0 and 1 for each random input parameter and obtaining corresponding values from each input parameter distribution. Traditional random sampling is the basic, most commonly used Monte Carlo simulation technique.

The general steps for implementing a Monte Carlo simulation using traditional random sampling are as follows (Isight 5.7 Component Guide):

1. Identify the input parameters. Assume appropriate distributions, and define properties for each (mean, standard deviation, or coefficient of variation).
2. Specify the number of simulations to be executed (often on the order of thousands of simulations).
3. Generate uniformly distributed random numbers for each input parameter.
4. Convert each uniform random number to a input parameter value corresponding to the appropriate distribution.
5. Simulate the design/process (execute model) using the current values for input parameters.
6. Repeat Step 3 through Step 5 for the number of simulations specified in Step 2.
7. Perform post processing by analyzing statistics of output parameters (mean, standard deviation, range, and distribution shape).

The traditional random sampling technique can require a large number of trails, which is computationally expensive.

Other sampling techniques were used to reduce computation time and evaluated for accuracy. Variance reduction techniques reduce the variance of the statistical estimates derived from the Monte Carlo simulation output data. These sampling techniques were developed to reduce the sample size (number of simulations) without sacrificing the quality of the statistical description of the behavior of the model or system. As a result, the error in estimates is reduced for the same number of simulations or fewer points are needed to obtain error or confidence levels similar to those obtained through

simple random sampling. The Descriptive sampling and Sobol sampling variance reduction techniques were used.

The Descriptive sampling technique (Saliby, 1990) generates sample points by dividing each input parameter distribution into subsets of equal probability, and the analysis is performed with each subset of each random variable only once. Each subset of one input parameter is combined with only one subset of each other input parameters (Fig. 2.6). Descriptive sampling technique is similar to the Latin Hypercube DOE technique.

Sobol sampling is a quasi-random sequence of numbers that are more uniformly distributed than both simple random sampling and descriptive sampling. In other words, samples obtained using Sobol's sequences exhibit a probability density function that is closer to the true density function (Fig. 2.7). A Sobol sequence generates numbers as binary fractions of appropriate length from a set of special binary fractions. The Sobol sampling technique also considers previously sampled points to avoid clusters and gaps (Burhenne et al., 2011).

2.4 Optimization Methods

The optimization method that was ultimately used in this research was the simulating annealing algorithm. This was chosen because it is a global search optimization algorithm. The name is representative of cooling materials to establish a crystalline structure. This algorithm is very well-suited for solving highly nonlinear problems when finding the global optimum is more important than a quick improvement of the design. Each iteration in the SA perturbates the current solution by a random step

size that is chosen based on a probability that depends upon the difference between corresponding function values and a global parameter (Ingber, L., 1993). This allows the direction to occasionally increase the value of the objective function, which can escape a local minimum. The likelihood of uphill steps reduces as the process progresses. As a result, the global minimum can be found (Venkataraman et al., 2009).

2.5 Modeling Software and Automation

Simulia, Dassault Systemes (Johnston, RI) software, including Abaqus and Isight, was chosen because it was available at the University of Denver Center of Orthopedic Biomechanics and also available at DePuy Synthes. This software is also widely used for life science and orthopedic applications. Abaqus CAE was used for most of the preprocessing, job execution, and post processing. Isight was used for optimization, sensitivity, and probabilistic analysis and is directly integrated with Abaqus. In addition, Pro/MECHANICA (PTC, Needham, MA) was used for initial mesh setup and node numbering for the study of calibration of finite element constitutive models for the lumbar spine disc based on intradiscal displacement data.

Workflows were created in Isight to automate the optimization and Monte Carlo probabilistic studies. The Abaqus input file is selected and any parameters defined in the input file can be used as input parameters, while history output in the input file can be tracked as objective functions or output parameters for the optimization and Monte Carlo studies. Isight automatically ran a number of iterations based on a specified number or until a convergence criteria was met.

The Holzapfel Ogden Gasser constitutive model was used to represent the AF throughout this dissertation. This model is an anisotropic hyperelastic continuum model with mathematically defined fiber properties in addition to matrix material properties. Parameters can be defined to represent the stiffness, orientation, and dispersion of the fibers and can be oriented in two directions to represent the AF. This enabled optimization, Monte Carlo, and sensitivity studies to include the fiber behavior. The strain energy function is represented by the following equations.

$$U = C_{10}(\overline{I}_1 - 3) + \frac{1}{D}\left(\frac{(J^{e\ell})^2 - 1}{2} - \ln J^{e\ell}\right) + \frac{k_1}{2k_2}\sum_{\alpha=1}^{N}\left\{\exp[k_2\langle\overline{E}_\alpha\rangle^2] - 1\right\}$$

$$\overline{E}_\alpha \overset{\text{def}}{=} \kappa(\overline{I}_1 - 3) + (1 - 3\kappa)(\overline{I}_{4(\alpha\alpha)} - 1)$$

The matrix stiffness is defined by C10 and the incompressibility is defined by D. The matrix is perfectly incompressible when D equals 0. The fiber stiffness is defined by k_1 and the nonlinear behavior of the fiber stiffness is defined by k_2. The dispersion of the fibers is defined by κ. The fibers are perfectly aligned when κ is set to 0 and isotropically dispersed when κ is set to 1/3.

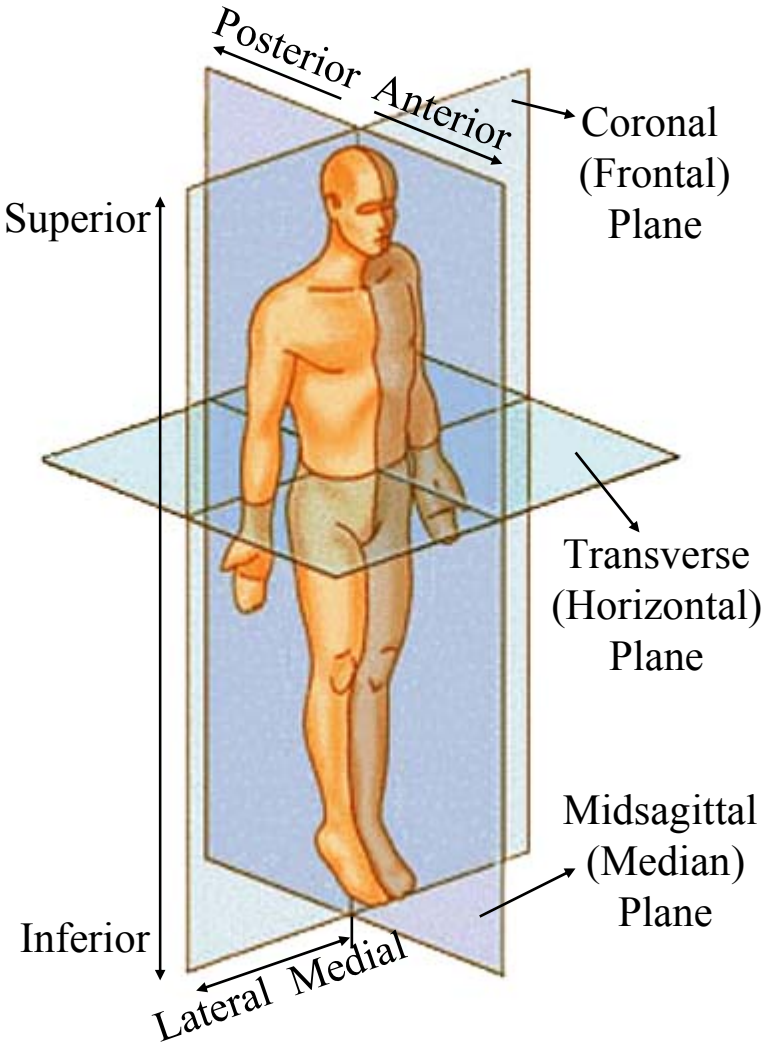

Figure 2.1. Clinical terms for anatomical direction and planes (SEER's Training Website, 2004)

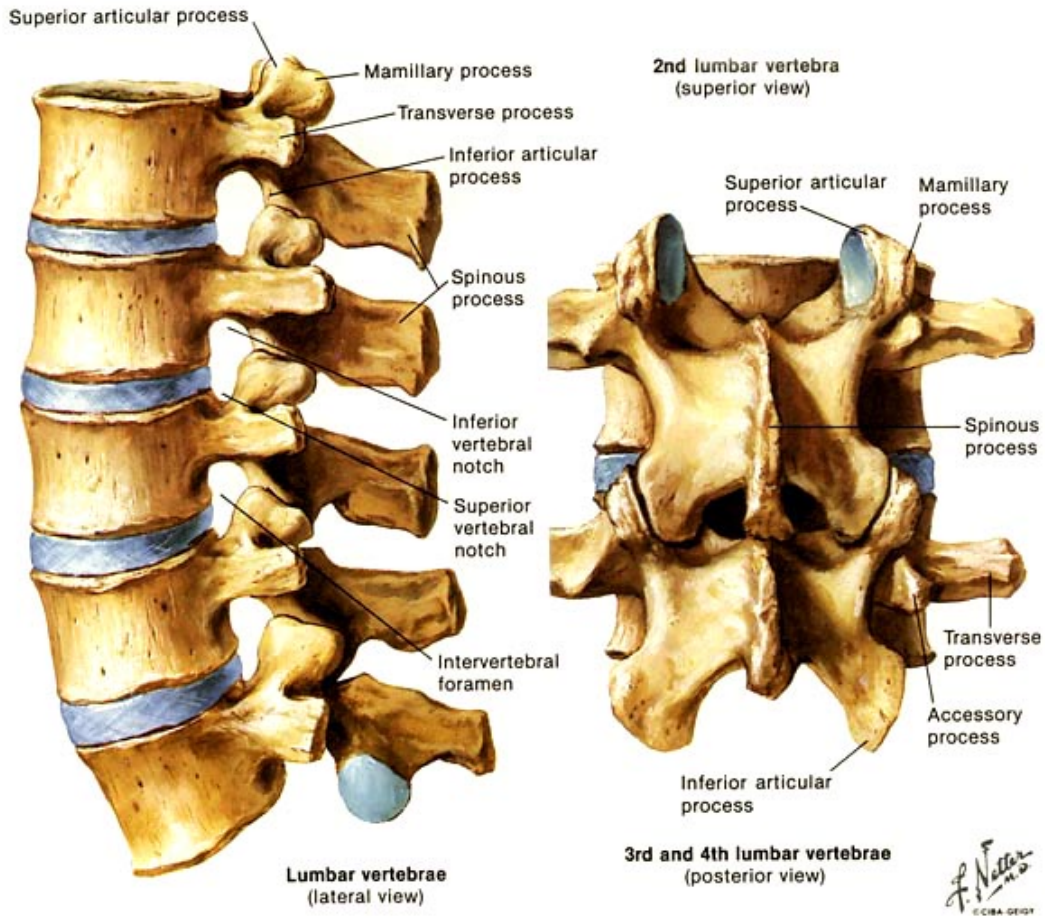

Figure 2.2. Anatomy of lumbar spine, artwork by Frank H. Netter (adapted from Department of Radiology, University of Wisconsin School of Medicine and Public Health website)

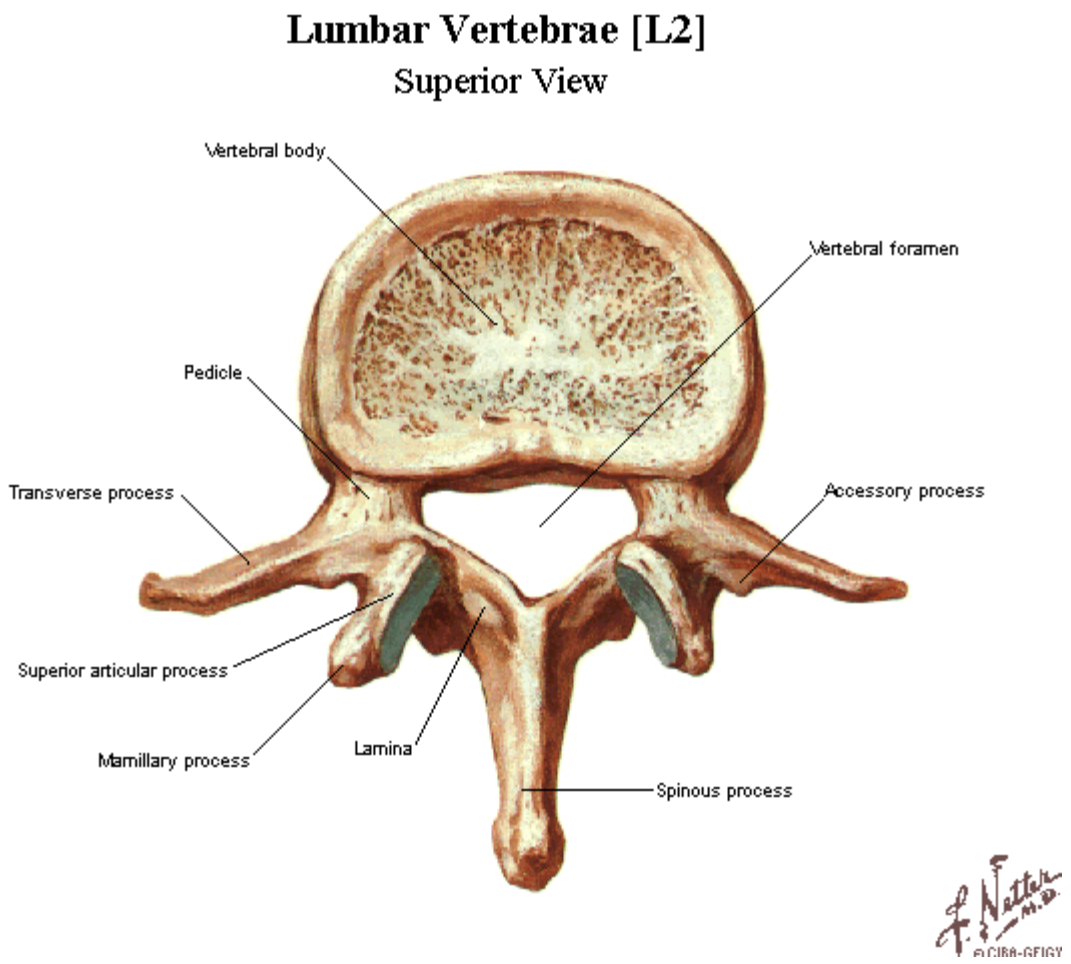

Figure 2.3. Boney anatomy of lumbar vertebrae, artwork by Frank H. Netter (adapted from https://www.studyblue.com/notes/note/n/ot-ot601-study-guide-2013-14-lutchmanpessina/deck/11442794)

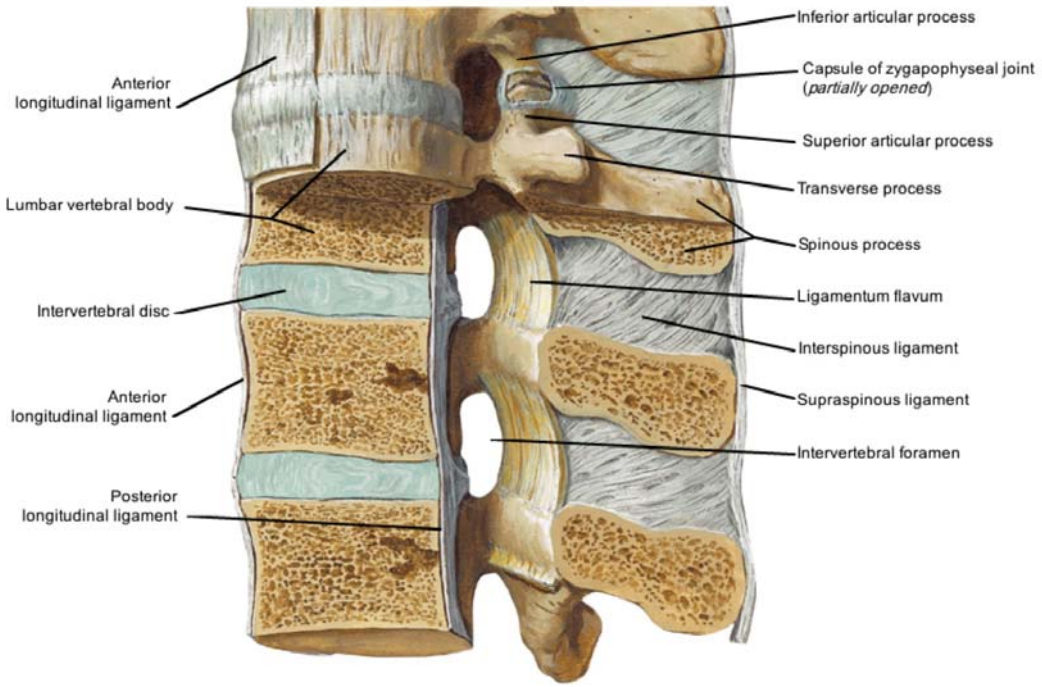

Figure 2.4. Ligaments of the lumbar spine, artwork by Frank H. Netter (adapted from https://www.studyblue.com/notes/note/n/ot-ot601-study-guide-2013-14-lutchmanpessina/deck/11442794).

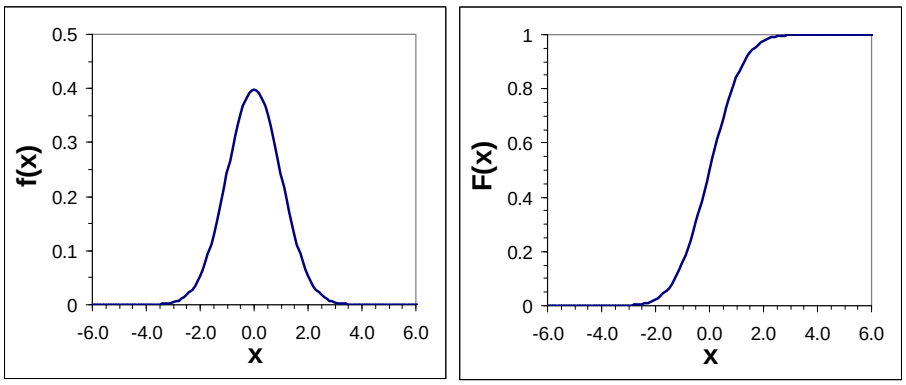

Figure 2.5. A probability distribution function (PDF), f(x) and its corresponding cumulative distribution function (CDF), F(x).

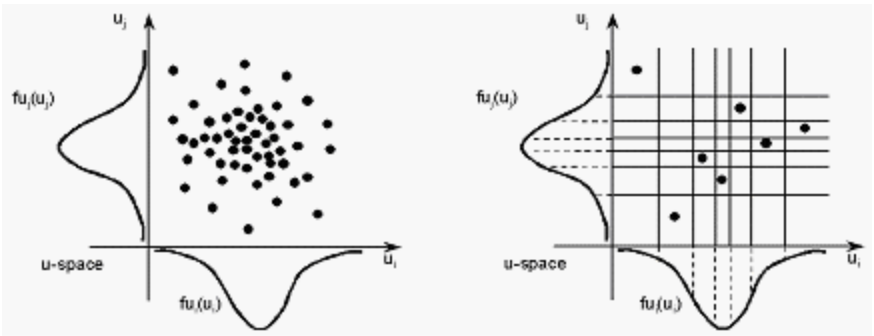

(a) (b)

Figure 2.6. Example of Monte Carlo sampling based on two input parameters using (a) traditional random sampling and (b) descriptive sampling. (Isight 5.7 Component Guide, Dassault Systèmes Simulia Corp., Johnstown, Rhode Island, 202, page 562).

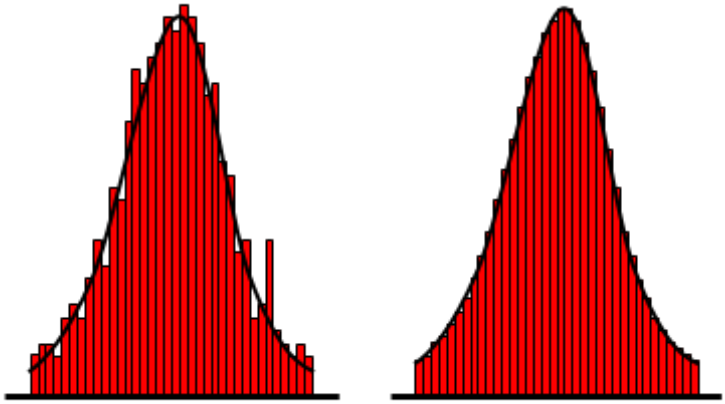

Figure 2.7. Distribution of an input parameter used in a Monte Carlo simulation based on (a) traditional random sampling and (b) Sobol sampling (Isight 5.7 Component Guide, Dassault Systèmes Simulia Corp., Johnstown, Rhode Island, 202, page 562).

CHAPTER 3 – CALIBRATION OF FINITE ELEMENT CONSTITUTIVE MODELS FOR THE LUMBAR SPINE DISC BASED ON INTRADISCAL DISPLACEMENT DATA

3.1 Background and Motivation

Several constitutive models of the human lumbar intervertebral disc have been calibrated based on kinematics. This chapter focuses on a method to calibrate constitutive models using displacement data at intradiscal points across the disc, in addition to angular kinematic data. The data was collected from compression, extension, flexion, and lateral bending on an L4L5 lumbar disc. Optimization was used to calibrate the model parameters. It was hypothesized that using intradiscal displacement data would result in a better constitutive model of the disc.

3.2 Introduction

The intervertebral disc acts as a joint between vertebrae and influences the kinematics of the human spine. Research has been performed to understand failure mechanisms of the lumbar disc, such as herniation, based on activities (Marras et al. 1993) and understand how failure relates to degeneration (Adams et al. 2000). Strain has been calculated by spatially measuring displacement in the disc during applied shear, pure moment, and compression (Tsantrizos et al. 2005, Costi et al. 2007).

Finite element (FE) models of the lumbar spine have been used to evaluate spine biomechanics and spinal implant performance, such as fusion cages (Tsuang et al. 2009), posterior fusion rods, and total disc replacement (Zhong et al. 2008). The evaluation can be based on kinematic data such as torque vs. rotation for each level of the spine. These models can be used to measure strain in the annulus fibrosis (AF) and pressure in the nucleus pulposis (NP). These models have been limited to calibration from kinematic data found in literature or based on biomechanics testing, including torque vs. rotation in flexion, extension, lateral bend, and axial rotation (Guan et al. 2006). Some models include the translation of each vertebra (Coombs et al. 2013).

The objective of the present study was to develop a methodology to calibrate constitutive models of the NP and AF using displacement data of intradiscal points across the mid-transverse plane of a level 4-5 lumbar spine disc. The calibration also used rotation data. To the author's knowledge, intradiscal displacement has not been used for such a calibration. It is hypothesized that this will result in a more accurate constitutive model by more accurately predicting the displacement and strain throughout the NP and AF since the model will be tuned using intradiscal displacement data. A better calibrated constitutive model of the NP and AF could be used to determine better nucleus replacement materials by comparing how the nucleus replacement displaces in the disc compared to the natural displacement of an intact disc. Another application could be to predict strain in the posterior lateral area of the AF based on known activities to understand how herniation occurs.

3.3 Methods

3.3.1 Specimen Preparations

A wire insertion device was used to insert nine and seven copper wires (0.170 mm diameter) in the IVD midtransverse plane parallel to the anterior-posterior and lateral IVD directions, using a needle. The inter-wire spacing was normalized to the IVD's anterior-posterior and lateral dimensions to define the complete mid-transversal plane. An intradiscal grid was formed using wire intersections as markers. The mid-transverse outer contour was defined with 24 lead beads (0.5 mm diameter). Sixteen beads were glued at the entrances and exits of wires from the IVD, and 8 beads were glued at equally spaced anterior-lateral and osteriorlateral IVD locations (Tsantrizos et al., 2005).

Biomechanical tests were conducted by Tsantrizos et al. (Tsantrizos et al., 2005) on several healthy lumbar functional spinal units without posterior anatomy and spinal pathology. One L4-L5 level was chosen for this study with the following characteristics: Thompson Grade 1, 26 years, female, mean intervertebral disc (IVD) height 9 (mm), mean BMD 0.665 (g/cm3).

3.3.2 Mechanical Testing

The mechanical testing of the FSU was performed (Tsantrizos et al. 2005) with a custom designed mechanical testing device which applied loads and moments using pneumatic cylinders with an accuracy of ±23.7N in compressive loads and ±0.16Nm in flexural moments. Cranial-caudal radiographs of constant magnification were captured during successive unload and load steps in this sequence: (i) unloaded and 1000 N axial

compression; (ii) unloaded and 10 Nm of extension with 500 N axial compression; (iii) unloaded and 10 Nm of flexion with 500 N axial compression; and (iv) unloaded and 10 Nm of left lateral bending with 500 N axial compression. Radiographs at peak load were acquired within five seconds after the load application in order to minimize creeping effects. The maximum angular bending during each load step was measured with a goniometer. All loads simulated the physiological loading experienced by the adult lumbar spine during standing, sitting, or lifting activities (Dolan et al. 1994).

3.3.3 Test Data Analysis

The radiographs were converted into digital images. The Cartesian coordinates of markers were measured with a 0.042mm precision. The marker projection for each loaded image was trigonometrically corrected based on the goniometer readings (Fig. 3.1). Relative marker displacements were calculated in the anterior-posterior and lateral IVD directions in the midtransverse plane (Tsantrizos et al. 2005).

3.3.4 Finite Element Model

A Pro/ENGINEER Wildfire 4.0 (PTC, Needham, MA) model was created with datum points representing the internal and external markers based on the unloaded disc. An image of the disc after being dissected across the mid-transverse plane was mapped to the same plane as the marker points. This image was scaled and rotated to match the external lead beads to the corresponding datum points. This image was then used to define a flat surface representing the mid-transverse cross section of the disc. Datum curves were created for the boundary separating the AF and NP. Datum curves were also created to define zones within the AF representing the anterior, posterior, left lateral, and

right lateral. Additional datum curves were created between the outer and inner NP boundaries to aid in meshing. This was done to represent the entire midtransverse cross section (Fig. 3.1) and for symmetric models about the sagittal plane, which were used for symmetric loading conditions. The Pro/MECHANICA FEM module (PTC, Needham, MA) was used to create nodes at the datum points and control the node numbering to match the numbering from the experimental data. The surface was meshed with quadratic triangular shell elements (Fig. 3.2) and imported into Abaqus CAE (Simulia, Johnston, RI). A separate mesh was defined for each load case because the marker points did not return to the same unloaded position between each unloading and loading step during mechanical testing. A 3D solid mesh was generated by offsetting the shell elements in the superior (+Z) direction resulting in four layers of C3D15 quadratic wedge elements. This represented the superior half of the disc. Element sets were defined for the NP and each zone of the AF. A node set was defined for the nodes representing the markers in the mid-transverse plane. This mesh represented a disc with parallel ends and was adjusted to include a lordotic angle. Only the average disc height and the midtransverse plane geometry were known, therefore geometry relationships of the lumbar spine (Gilad & Nissan 1986) were used to determine an average lordotic angle. The total lordotic angle is defined as the total angle between the endplates of the intervertebral disc. This angle was calculated as 7.13° using trigonometric relationships described in the equations below, where a is the width of the inferior face of L4, c is the width of the superior face of L5, g is the anterior disc height, h is the posterior disc height, θ_1 is the superior disc lordotic angle relative to the transverse plane, and θ_2 is the inferior lordotic angle relative to the transverse plane.

$$\theta_1 = \sin^{-1}\left[\frac{\frac{(g-h)}{2}}{a}\right] = \sin^{-1}\left[\frac{\frac{(12.7-7.7)}{2}}{34.9}\right] = 3.53^\circ$$

$$\theta_2 = \sin^{-1}\left[\frac{\frac{(g-h)}{2}}{c}\right] = \sin^{-1}\left[\frac{\frac{(12.7-7.7)}{2}}{34.2}\right] = 3.6^\circ$$

Total angle = 7.13 º

This total disc angle was then used to correct the node locations based on trigonometric relationships at each layer of the mesh (Fig. 3.2).

An orientation was defined for the elements in the AF, which was used to define the directions of the AF fibers. Direction 1 was tangent to the external edges of the disc and direction 2 was along the axial superior direction (Z) (Fig. 3.3). The angles of the two fiber directions were +/- 38º from the direction 1 vector.

A reference point was defined on the superior end of each mesh and a kinematic coupling constraint was defined between the reference point and the superior nodes. A symmetry model about the sagittal plane was created for compression, extension, and flexion load cases. For all models, the midtransverse plane was constrained with a symmetry constraint. For the full lateral bend model, the superior reference point was constrained in Z rotation, and the origin node was constrained in X and Y translation. For the symmetry model, the origin node was constrained in X translation and the sagittal plane was constrained with a symmetry constraint (Fig. 3.4). Loads were applied to the reference point on the superior surface for each model (Table 3.1). The loads in the

symmetry models were half of the load used in the mechanical test. For all models, the X and Y displacements of the marker point nodes and the angular displacement of the reference point on the superior surface were measured throughout the analysis.

3.3.5 Optimization

Constitutive models were assigned to the disc zones. In all but the one zone model, a Holzapfel-Gasser-Ogden anisotropic hyperelastic model, was used for the AF because it mathematically represents the fibers in the tissue (Gerhard et al. 2000; Gasser et al. 2006), which did not require a radially layered mesh and discrete fiber elements. This model also has the advantage of using parameters to describe fiber angles and dispersion during optimization, which would be difficult with discrete fiber elements. The Holzapfel-Gasser-Ogden model contains 5 parameters (D, C10, κ, k_1, k_2). However, kappa (κ), which represents the fiber dispersion, was set to 0 representing perfect fiber alignment in both directions. The Mooney Rivlin hyperelastic model was used for the NP and for single zone model. It contains three parameters (D1, C10, C01). The linear elastic model was also used for the NP and contains 2 parameters (E, ν).

Each model was assigned various combinations of constitutive models for each zone (Table 3.2). The models are presented in order of complexity and number of parameters. The first model was a single Mooney Rivlin constitutive model for the entire disc, which only contained 3 parameters. Second, the AF was defined as a Holzapfel-Gasser-Ogden model and the NP was defined as linear elastic model. Third, the NP was defined as a Mooney Rivlin model. Fourth, separate Holzapfel-Gasser-Ogden models were defined for each AF zone (anterior, lateral, and posterior). The lateral left and right

zones were assumed to have the same Holzapfel-Gasser-Ogden model. The NP was defined as a linear elastic model. The final model was similar to the fourth but defined the NP as a Mooney Rivlin model. Isight 5.7 (Simulia, Johnston, RI) was used to calibrate the values of the parameters using a simulated annealing optimization algorithm because it is a global exploratory algorithm and well suited for multiple parameters. The objective function was a least squares sum of all the errors between the displacements of each marker point node in the FE model and the mechanical testing data for the anterior-posterior (X) direction and the lateral (Y) direction, measured in the midtransverse plane. The compression, flexion, and extension models were symmetry models with 45 marker point nodes. Therefore, the objective function was a sum of 90 squared errors for each of the loading conditions. The lateral bend model contained all 81 marker point nodes and the objective function was a sum of 162 squared errors. The total sum of errors measured was 432. Bounds were placed on the input parameters and side constraints were defined for the angular displacement in each load case with a +/- 0.25º bound around the targets of 0° for compression, -4° for extension, 6° for flexion, and -3° for left lateral bending. These angles are half the values measured in the mechanical test because only the superior model was created using the midtransverse plane as a symmetry plane. Isight workflows were defined such that the compression, extension, flexion, and lateral bend models ran in parallel based on the input parameters for the constitutive models (Fig. 3.5). The error was calculated for the X and Y displacements for each model, resulting in 8 objective functions. The penalty was calculated based on the angular side constraints.

3.4 Results

All optimization runs converged on the objective and penalty functions and the results of the objective function and penalty were summarized (Table 3.3). The optimized parameter values for each model were also summarized (Table 3.4). The objective and penalty for each model showed a trend in reducing the objective and penalty as the number of parameters increases, which also corresponds to more complex constitutive models (Fig. 3.6a). There was a marginal improvement in the objective and marginal increase in the penalty when using a Mooney Rivlin model compared to a linear elastic model for the NP. In addition, a 4 zone NP greatly reduces the error in angular displacement (Fig. 3.6b). The displacement of marker point nodes is visually different between different constitutive model combinations for compression, extension, and lateral bending (Fig. 3.7 through 3.10), especially in the anterior quadrant during flexion (Fig. 3.9). This is more apparent when visualizing the displacement fringe plots (Fig. 3.11 through 3.14) and displacement vector plots (Fig. 3.15 through 3.18). For comparison purposes, the 4 zone model with a linear elastic NP was optimized using the target angles as the objective function without regard for the marker displacements. This model converged to angle errors less than 0.1° but had a total displacement error of 68.82mm^2.

A visual difference can also be seen for the maximum principal strain, especially in the anterior quadrant of the AF (Fig. 3.19 through 3.22). The anterior AF is bulging in the anterior and posterior directions relative to the center of the AF, as was measured

experimentally by Tsantrizos et al. Similar differences can be seen for compression, extension, and lateral bending.

The resulting, optimized constitutive parameters from the 4 zone AF models were compared to literature values. Several examples were found using a linear elastic model for the NP and AF with fibers modelled as discrete elements (Table 3.5). The values of the Young's Modulus (E) for the NP ranged from $1x10^{-6}$ to 4 MPa. The value of E from the linear elastic NP 4 zone AF model was 2.157 MPa. The value of the Poisson's Ratio (ν) for the NP was 0.5 or 0.4999, which is nearly incompressible. The value of ν from the linear elastic NP 4 zone AF model was 0.309, which is more compressible than the literature models. Examples using a Holzapfel-Gasser-Ogden model were not found, but examples were found using a Mooney Rivlin model for the NP and AF with fibers modelled as separate elements (Table 3.5). The range of C_{10} and C_{01} parameters for the NP was reported between 0.12 and 0.19, and between 0.03 and 0.09 respectively. The optimized values of C_{10} and C_{01} from the 4 zone NP model was 0.532 and 0.035 respectively. The value of C_{10} was about 2.5 times greater than the greatest value reported in literature and the value of C_{01} was in the range of values reported in literature. The value D_1 for the AF found in literature was reported as 1 or as a Poisson's Ratio of 0.4999, which is nearly incompressible. The value of D_1 from the 4 zone AF with a Mooney Rivlin NP model was 0.348, which falls in the range of the literature.

To compare the AF models, further consideration was needed. The Holzapfel-Gasser-Ogden model is similar to a reduced polynomial hyperelastic constitutive model with additional terms to define the fiber behavior. The initial shear modulus (μ_0) and bulk modulus (K_0) could be used to compare the parameters from the Holzapfel-Gasser-

Ogden model to the Mooney Rivlin model based on the following relationships (Abaqus 6.12 Analysis User's Manual, 2012, Holzapfel et al. 2000, Gasser et al. 2006):

Initial Shear Modulus:

$$\textit{Holzapfel: } \mu_0 = 2C_{10}, \quad \textit{Mooney Rivlin: } \mu_0 = 2(C_{10} + C_{01})$$

$$\textit{Therefore, } C_{10_{Holzapfel}} = (C_{10} + C_{01})_{Mooney\,Rivlin}$$

Bulk Modulus:

$$\textit{Holzapfel: } K_0 = \frac{2}{D}, \quad \textit{Mooney Rivlin: } K_0 = \frac{2}{D_1}$$

$$\textit{Therefore, } \quad D_{Holzapfel} = D_{1_{Mooney\,Rivlin}}$$

Based on this relationship, the sum of C_{10} and C_{01} from the Mooney Rivlin models found in literature ranged between 0.225 and 0.7. The values of C_{10} from the 4 zone AF with a linear elastic NP model was between 0.599 and 1.073. The values of C_{10} from the 4 zone AF with a Mooney Rivlin NP model was between 0.724 and 0.948. The value D_1 for the AF found in literature was reported as 1 or as a Poisson's Ratio of 0.45, which is nearly incompressible (Holzapfel-Gasser-Ogden D parameter approaching zero). The values of D from the 4 zone AF with a linear elastic NP model was between 0.021 and 0.747, which falls in the range of the literature. The values of D from the 4 zone AF with a Mooney Rivlin NP model was between 0.07 and 1.993, which falls in the range of the literature for some zones and outside of range for other zones. Unfortunately, the parameters that describe the fiber behavior in the Holzapfel-Gasser-Ogden model (K_1, K_2, and κ) could not be compared to the models found in literature because there was incomplete information describing the discrete fiber elements that were used in the

models found in the literature. Stiffness or Young's Modulus with cross sectional area was often reported, but the number of fiber elements was not reported. However, the fiber parameters vary greatly between the 4 Zone AF models and between each zone, indicating the behavior of these models is not highly sensitive to these fiber definitions.

3.5 Discussion

The displacement errors, as measured by the objective function, in the midtransverse plane were not very sensitive the number of zones in the annulus. In fact, the 1 zone AF model with a linear elastic and Mooney Rivlin NP had an objective function of 64.602 and 66.165 respectively, while the 4 zone AF model with a linear elastic and Mooney Rivlin NP had an objective function of 63.080 and 63.989 respectively. However if a 4 zone model is only optimized based on angle, the displacement errors become larger.

The error in the angular rotation was much more sensitive to the number of zones. This would be expected since the stiffness of the AF tissue changes from anterior to the posterior regions (Elliot & Setton 2001; Guerin & Elliot 2006). Therefore, moment-rotation data must be considered during calibration. The objective function did not decrease significantly from a 2 zone to a 4 zone model.

A linear elastic material model is sufficient to model the NP. The linear elastic model slightly improved the displacement error result but slightly decreased the angular displacement error result. Including marker point displacement reduced error compared to using only angular displacement.

This study presents a process to calibrate constitutive models of the NP and AF using displacement data of intradiscal points across the mid-transverse plane of a level 4-5 lumbar spine disc. However, there are several limitations. This study was based on one specimen, but several specimens would show how closely these constitutive models calibrate across various healthy specimens. The experimental data was based on the assumption that the displacement remained in the mid-transverse plane. Three dimensional displacement data may improve calibration which has been experimentally collected (Costi et al. 2007). Also, the disc model presented in this study assumed flat end plates with a lordotic angle based on literature. MRI data could define actual 3 dimensional geometry, if it were available. Regarding the annulus, it was assumed that the Holzapfel-Gasser-Ogden model had perfectly aligned fibers and the fiber angle was held constant. The fiber dispersion and fiber angle could be included in the calibration, but would add two more parameters to each AF zone.

3.6 Conclusion

This calibration process, using optimization techniques on intradiscal displacement data, is a way to better define constitutive models for spine disc models than using kinematic data alone. A four zone AF is needed to reduce rotational displacement error in addition to the internal displacement error, using a Holzapfel-Gasser-Ogden constitutive model. A linear elastic constitutive model is sufficient to model the NP. These models can be used to more accurately measure strain and provide more insight on how the IVD behaves. There are several potential applications for these models. Based on activities of daily living and understanding failure criterion for AF

tissue, it would be possible to understand what activities would cause herniation. Another application would be the development of nucleus replacement materials to better match the strain behavior of the disc.

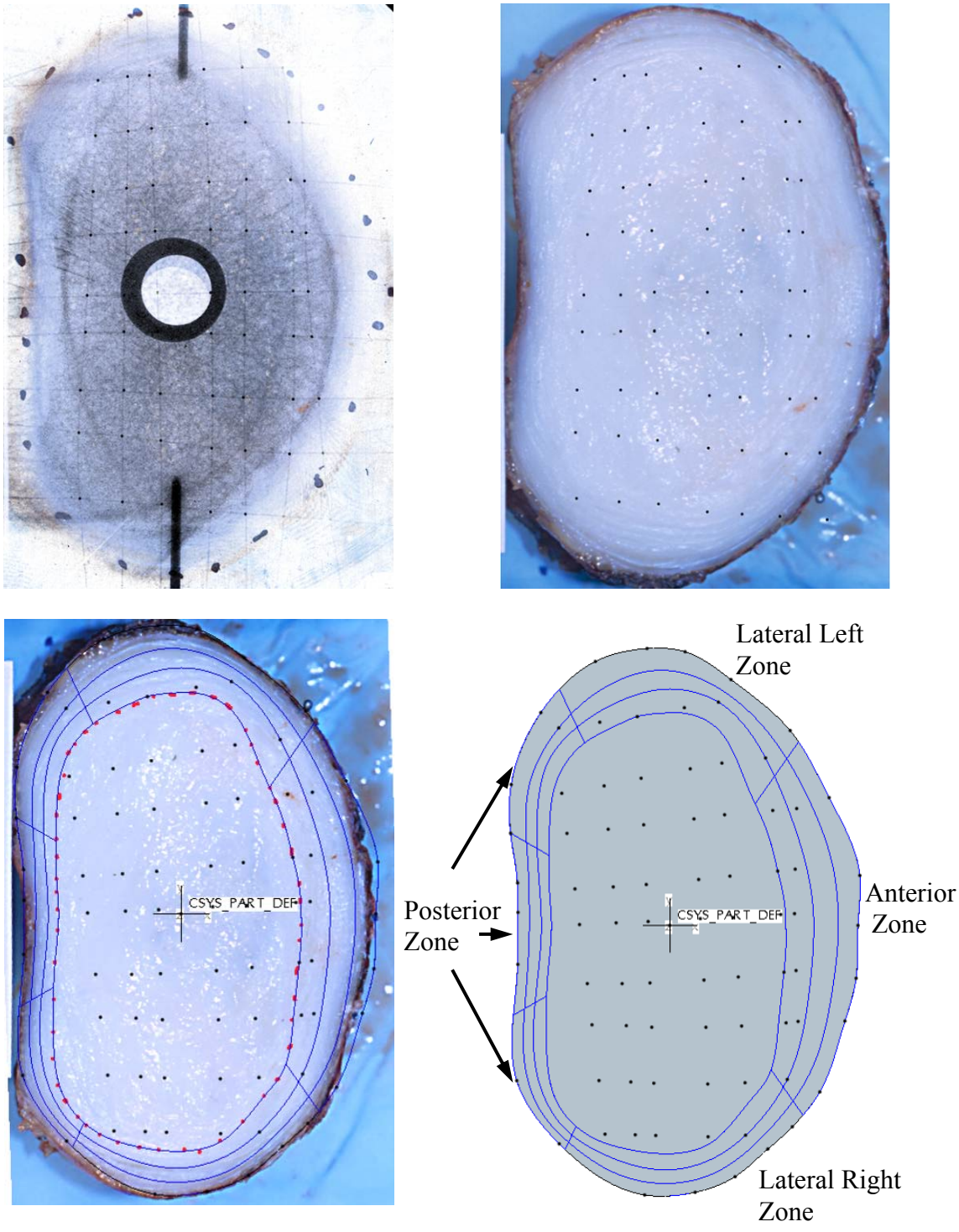

Figure 3.1. Model definition process: radiographs to marker points to AF and NP zones. The AF is divided into anterior, posterior, and lateral zones

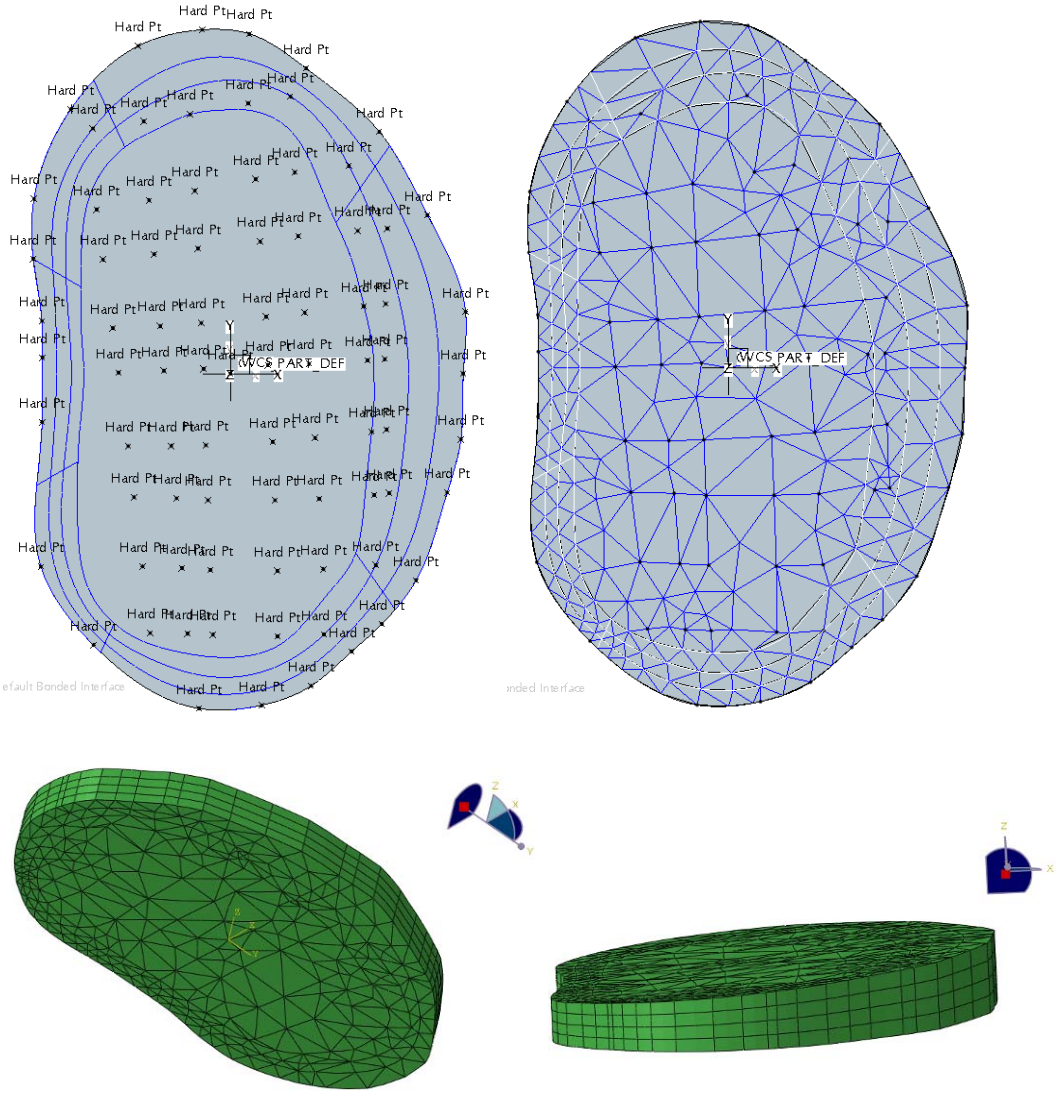

Figure 3.2. Model definition process: Marker points defined as nodes in the 2D Mesh which was extruded to create a 3D mesh (symmetric about the mid-transverse plane) and then adjusted for the lordotic angle

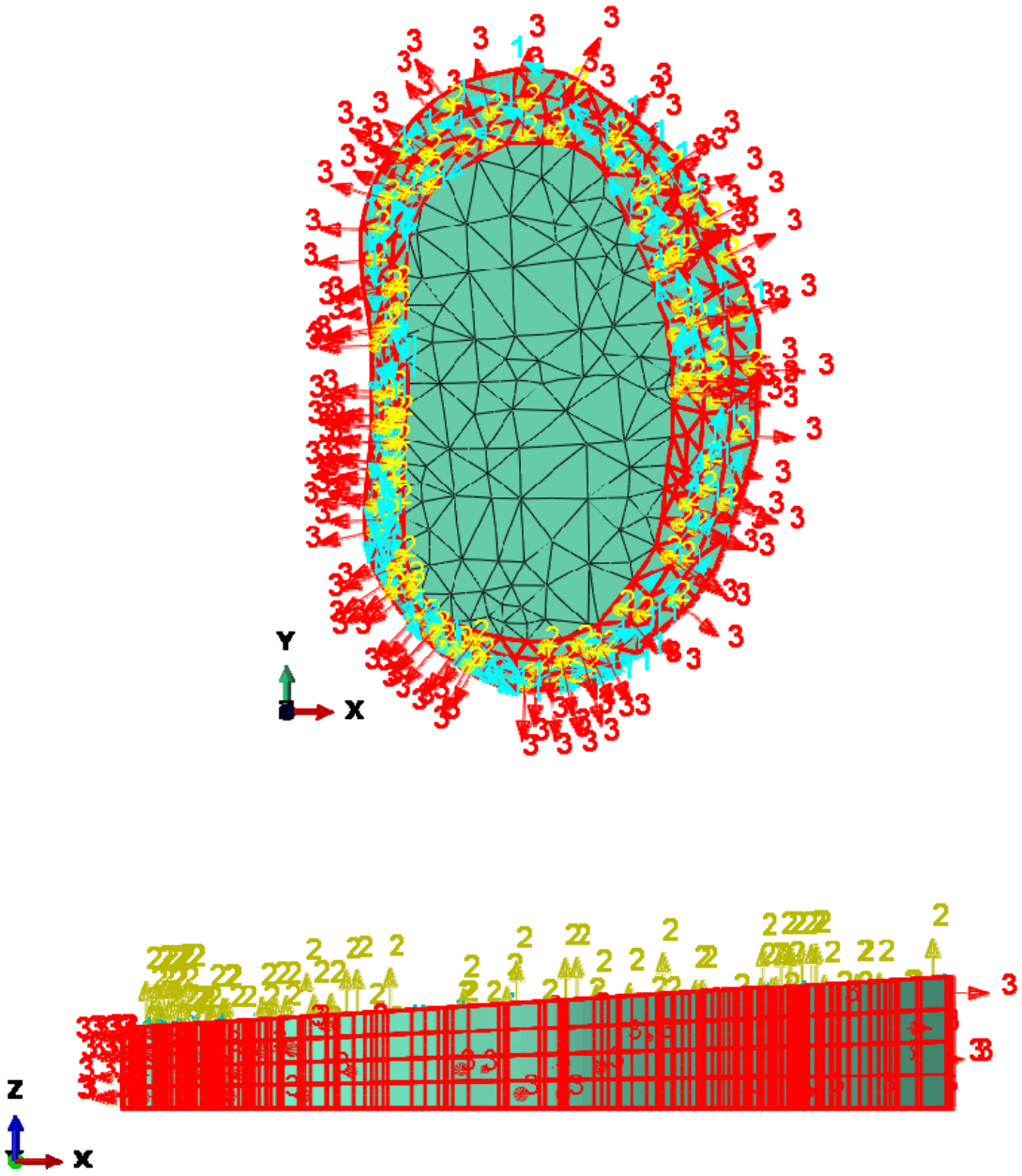

Figure 3.3. Orientation definition in annulus fibrosis to define fiber directions

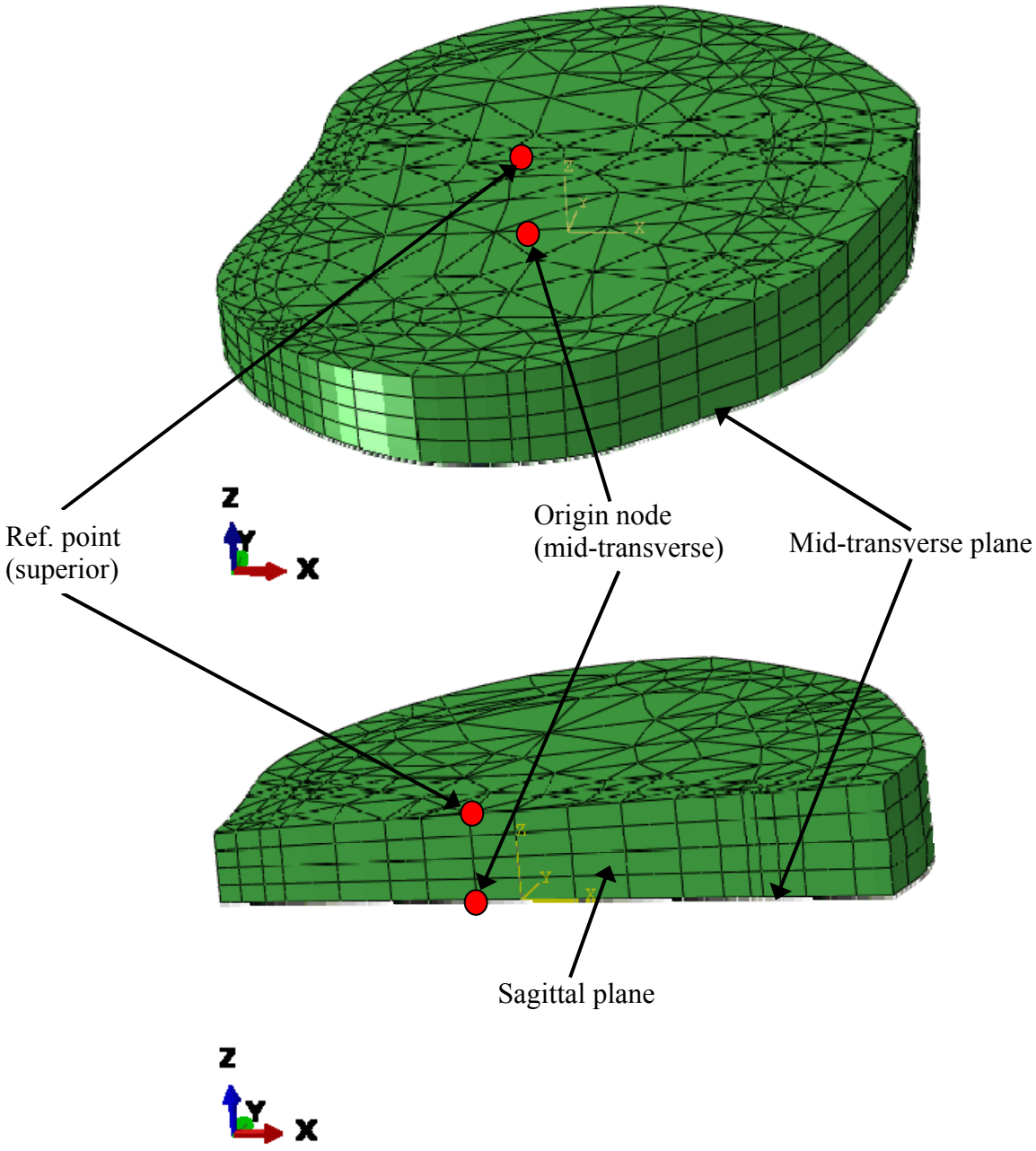

Figure 3.4. Boundary conditions for full and symmetric discs

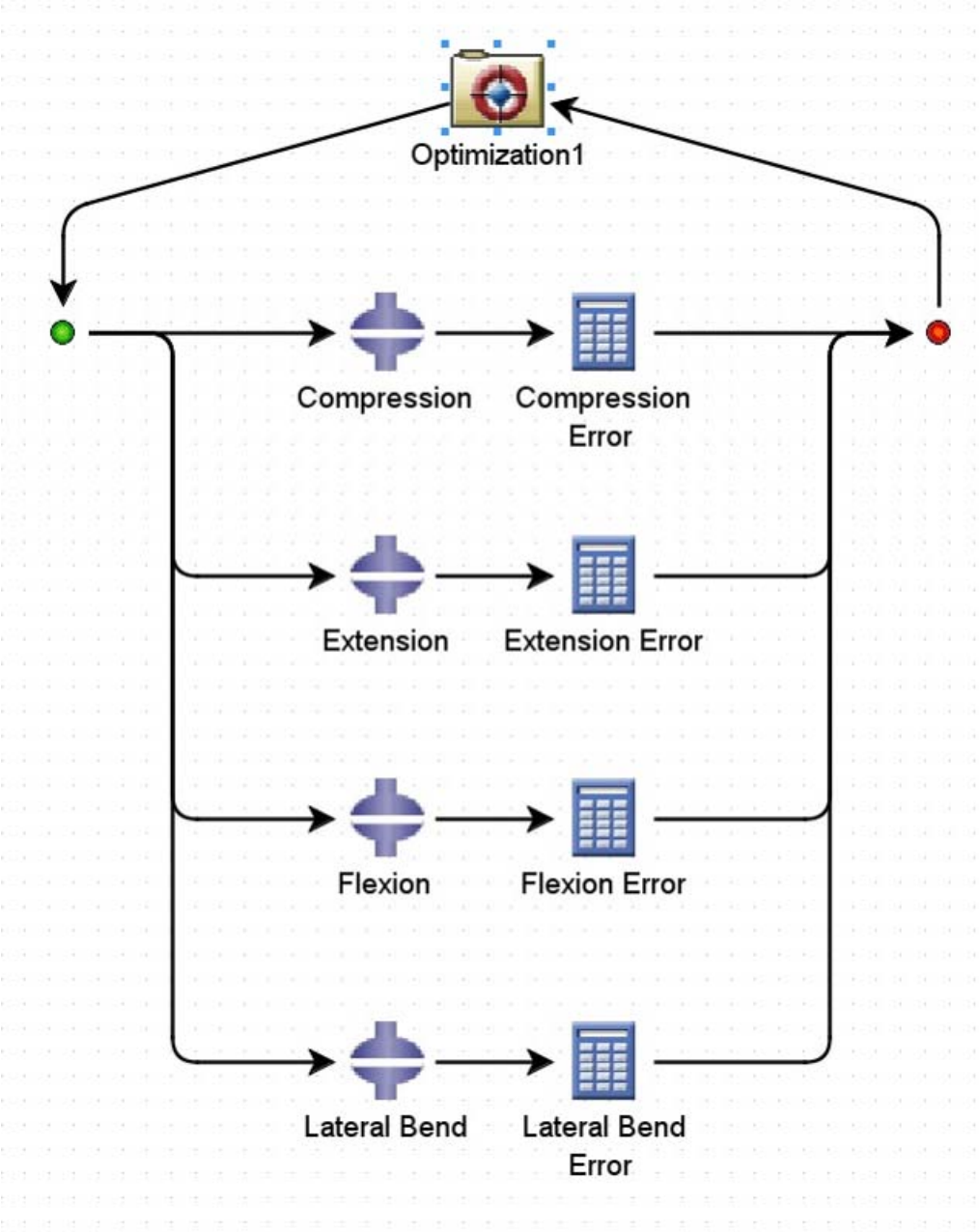

Figure 3.5. Typical Isight workflow used for each combination of constitutive models

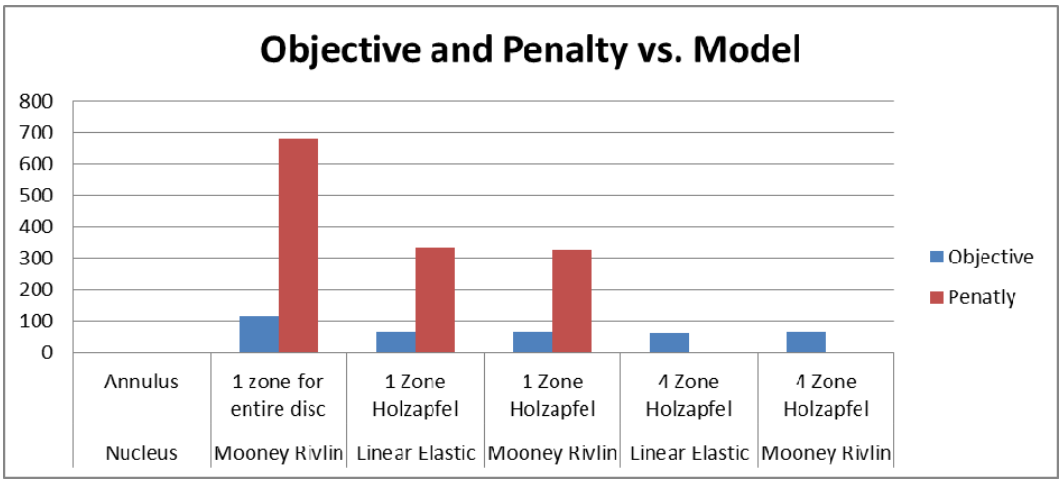

(a)

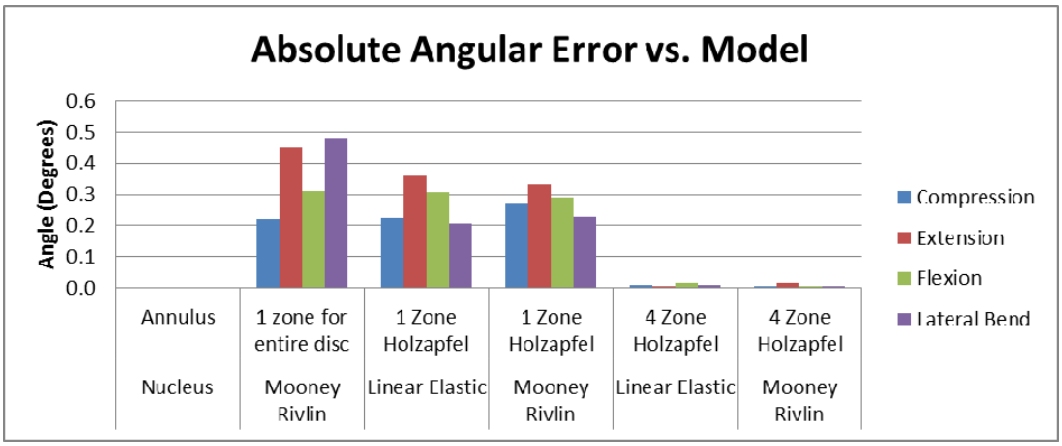

(b)

Figure 3.6. Graph of objective and penalty (a) Graph of the absolute angular error; (b) both as a function of constitutive model combinations of the NP and AF

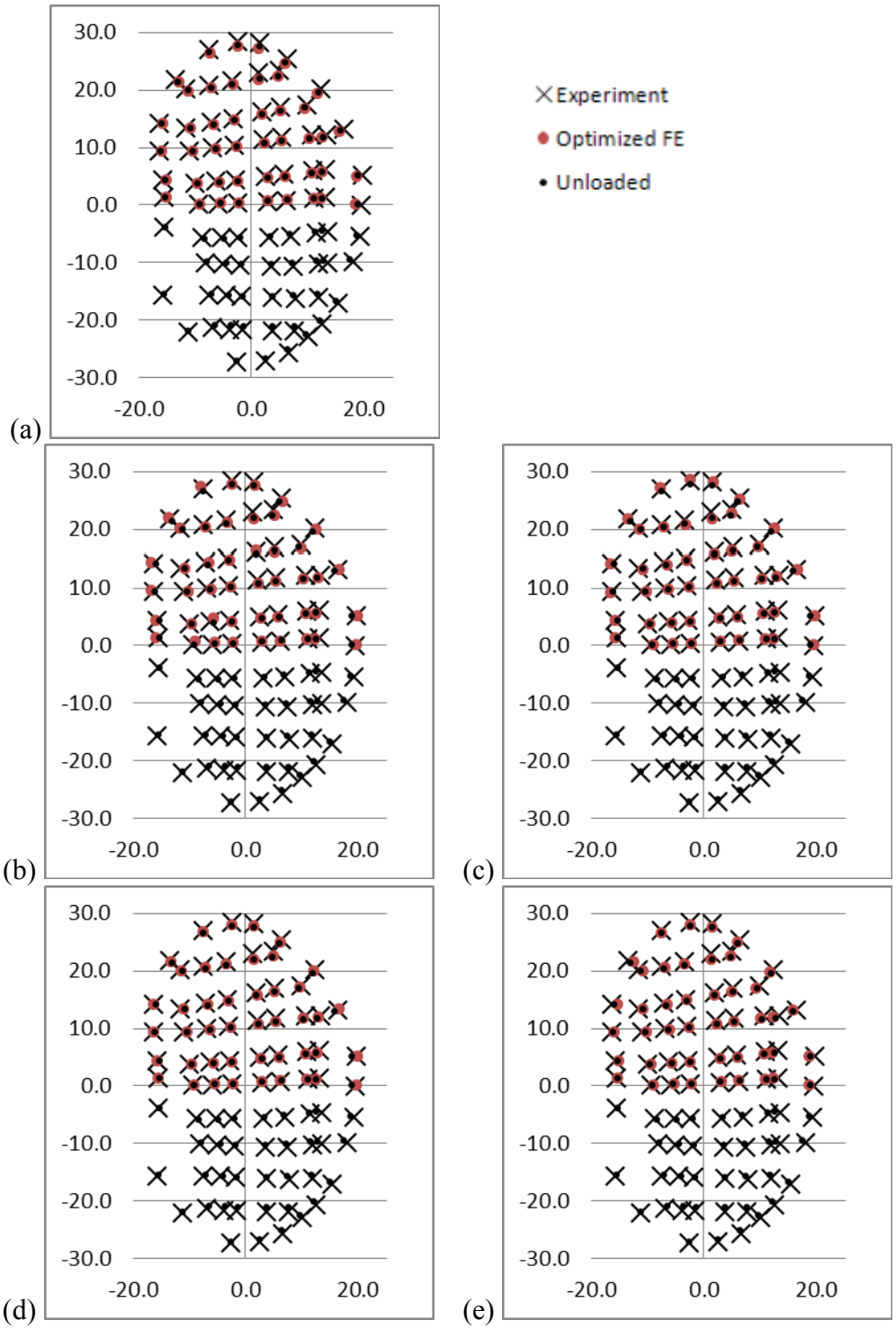

Figure 3.7. Graphs of ***compression*** displacement of marker points (a) single zone, Mooney Rivlin; (b) 1 zone annulus, linear elastic nucleus; (c) 1 zone annulus, Mooney Rivlin nucleus; (d) 4 zone annulus, linear elastic nucleus; (e) 4 zone annulus, Mooney Rivlin nucleus

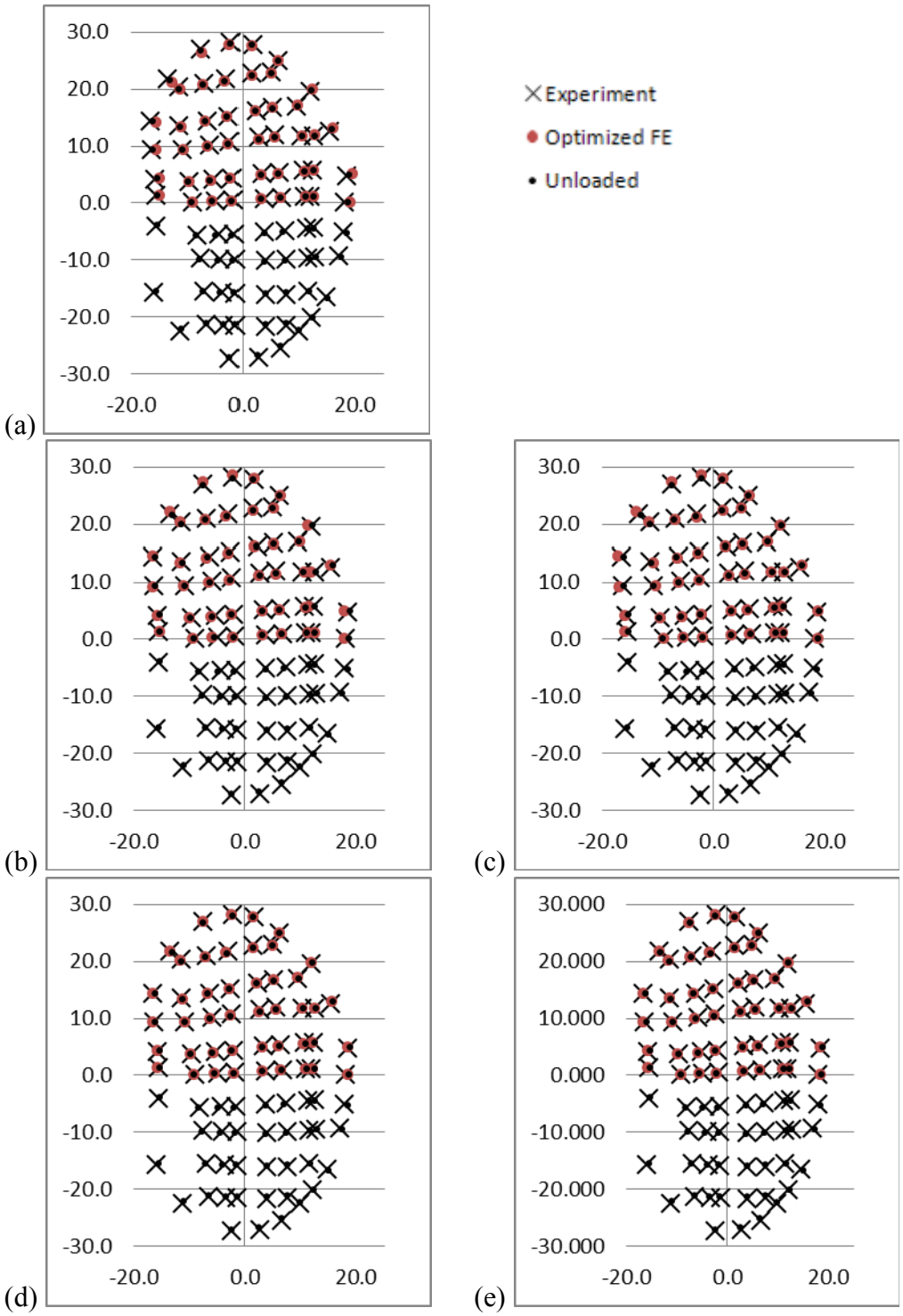

Figure 3.8. Graphs of extension displacement of marker points (a) single zone, Mooney Rivlin; (b) 1 zone annulus, linear elastic nucleus; (c) 1 zone annulus, Mooney Rivlin nucleus; (d) 4 zone annulus, linear elastic nucleus; (e) 4 zone annulus, Mooney Rivlin nucleus

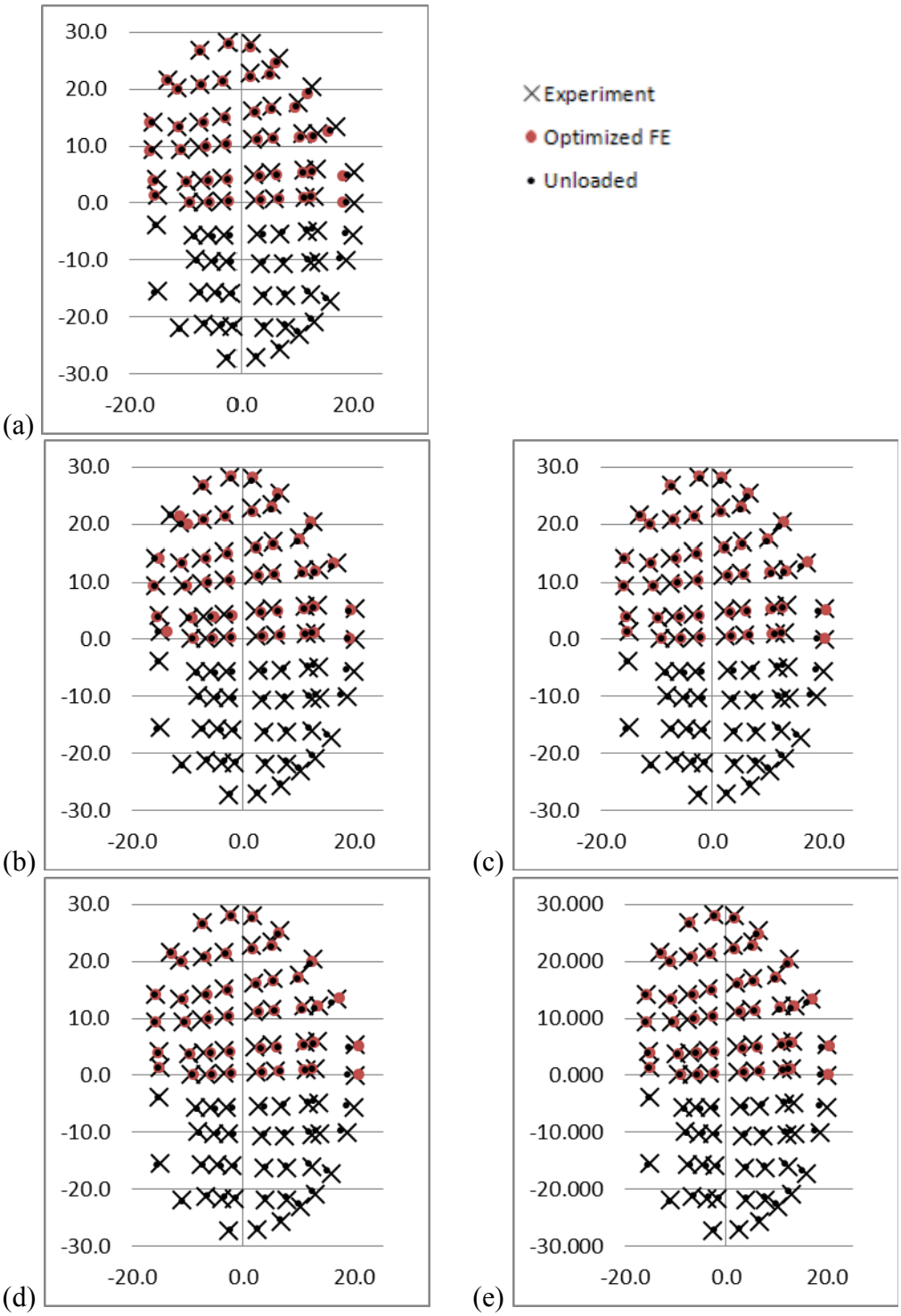

Figure 3.9. Graphs of flexion displacement of marker points (a) single zone, Mooney Rivlin; (b) 1 zone annulus, linear elastic nucleus; (c) 1 zone annulus, Mooney Rivlin nucleus; (d) 4 zone annulus, linear elastic nucleus; (e) 4 zone annulus, Mooney Rivlin nucleus

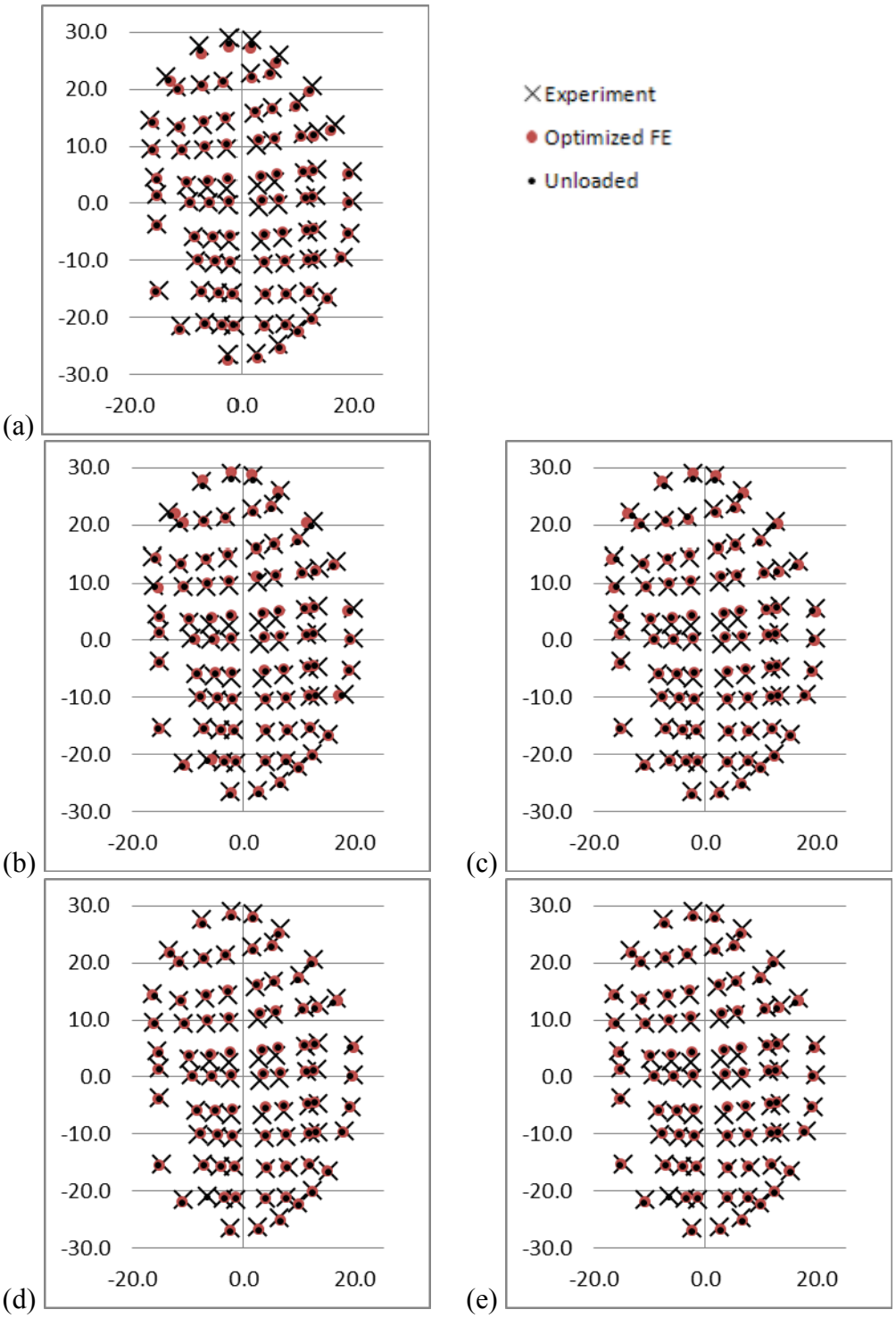

Figure 3.10. Graphs of ***lateral bending*** displacement of marker points (a) single zone, Mooney Rivlin; (b) 1 zone annulus, linear elastic nucleus; (c) 1 zone annulus, Mooney Rivlin nucleus; (d) 4 zone annulus, linear elastic nucleus; (e) 4 zone annulus, Mooney Rivlin nucleus

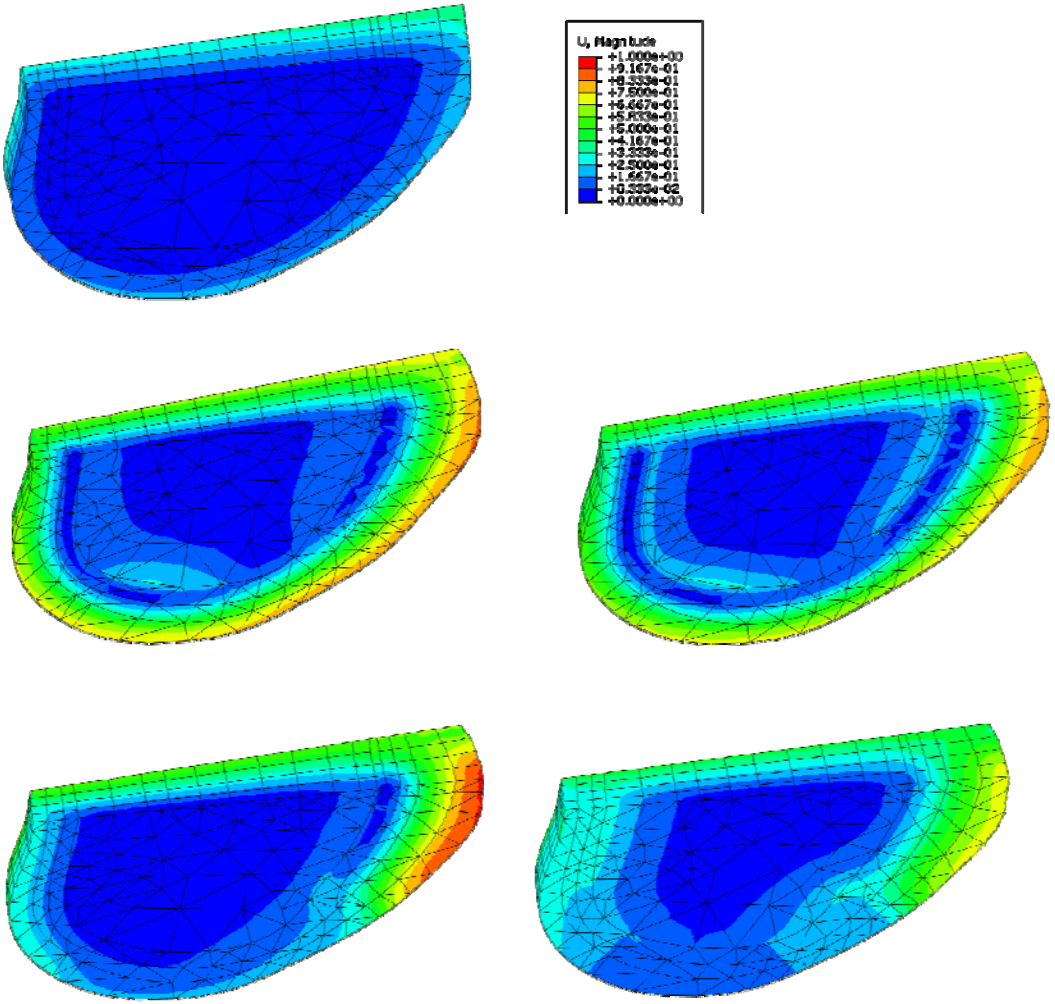

Figure 3.11. Fringe plots of ***compression*** total displacement (a) single zone, Mooney Rivlin; (b) 1 zone annulus, linear elastic nucleus; (c) 1 zone annulus, Mooney Rivlin nucleus; (d) 4 zone annulus, linear elastic nucleus; (e) 4 zone annulus, Mooney Rivlin nucleus

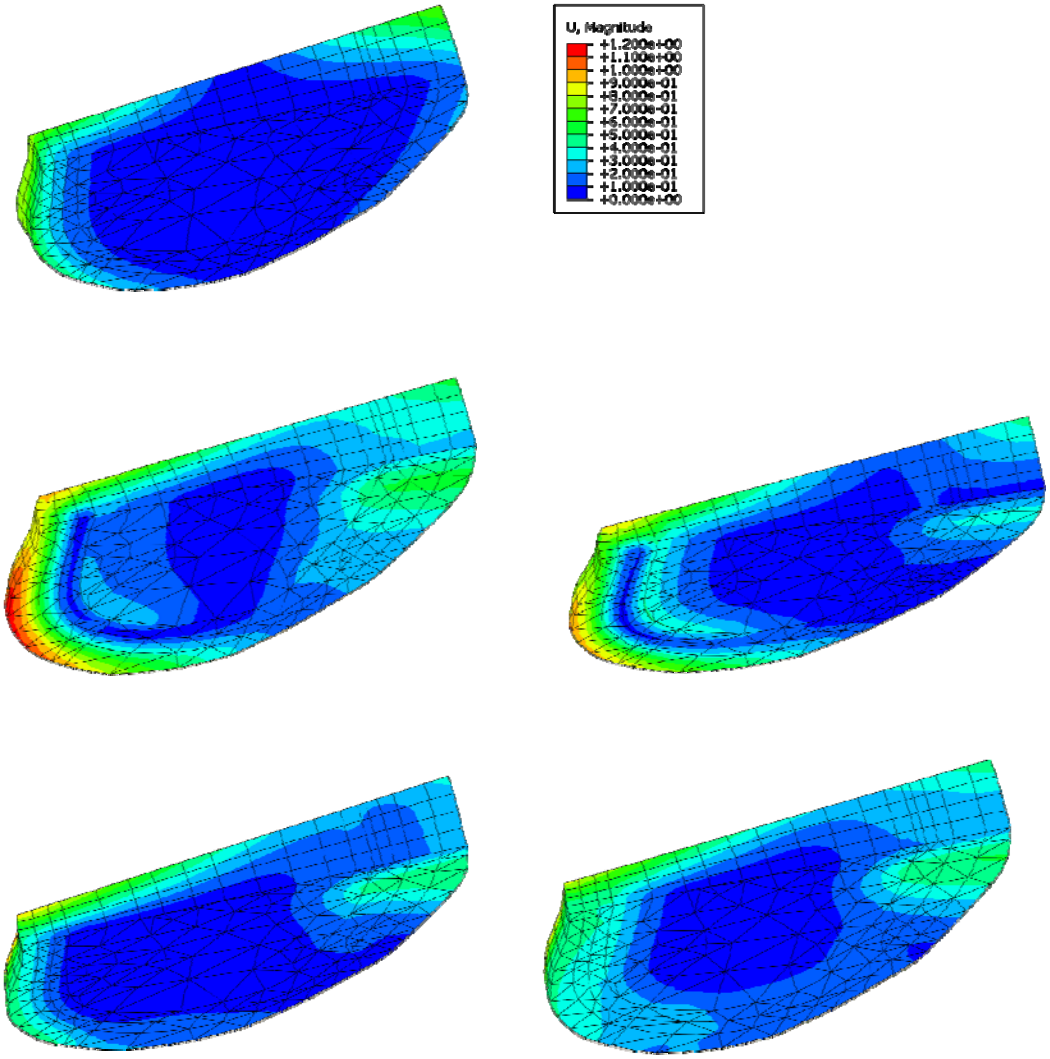

Figure 3.12. Fringe plots of ***extension*** total displacement (a) single zone, Mooney Rivlin; (b) 1 zone annulus, linear elastic nucleus; (c) 1 zone annulus, Mooney Rivlin nucleus; (d) 4 zone annulus, linear elastic nucleus; (e) 4 zone annulus, Mooney Rivlin nucleus

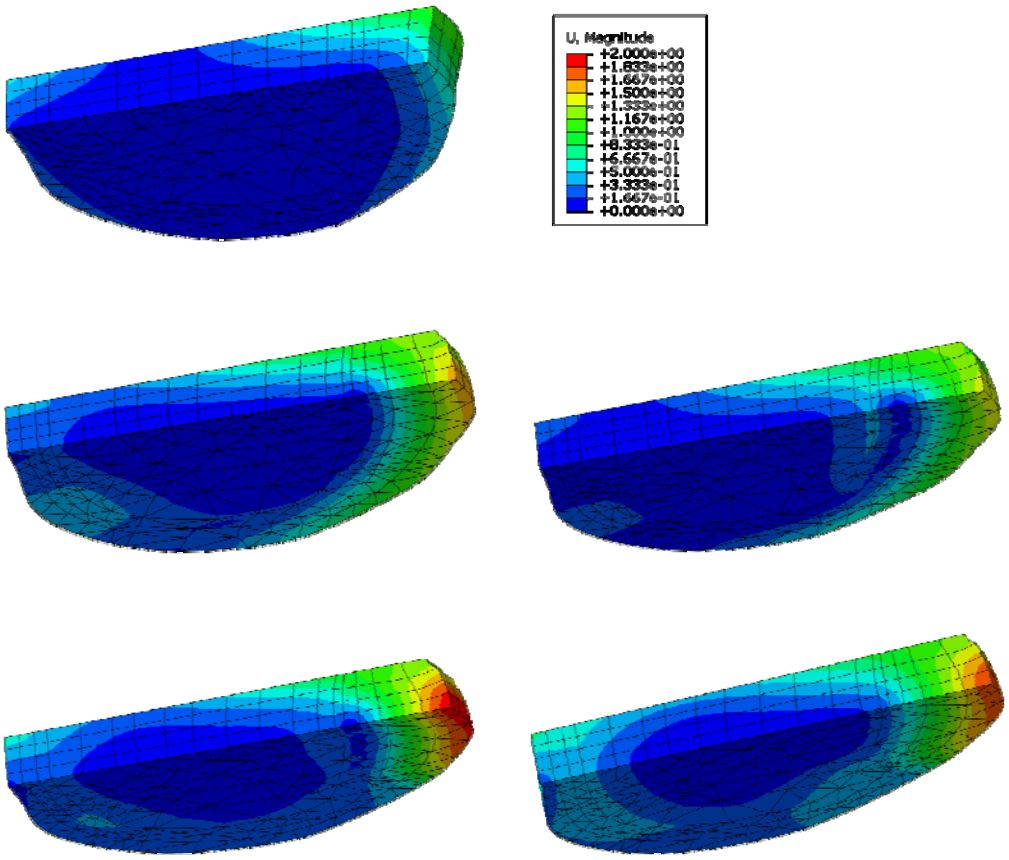

Figure 3.13. Fringe plots of ***flexion*** total displacement (a) single zone, Mooney Rivlin; (b) 1 zone annulus, linear elastic nucleus; (c) 1 zone annulus, Mooney Rivlin nucleus; (d) 4 zone annulus, linear elastic nucleus; (e) 4 zone annulus, Mooney Rivlin nucleus

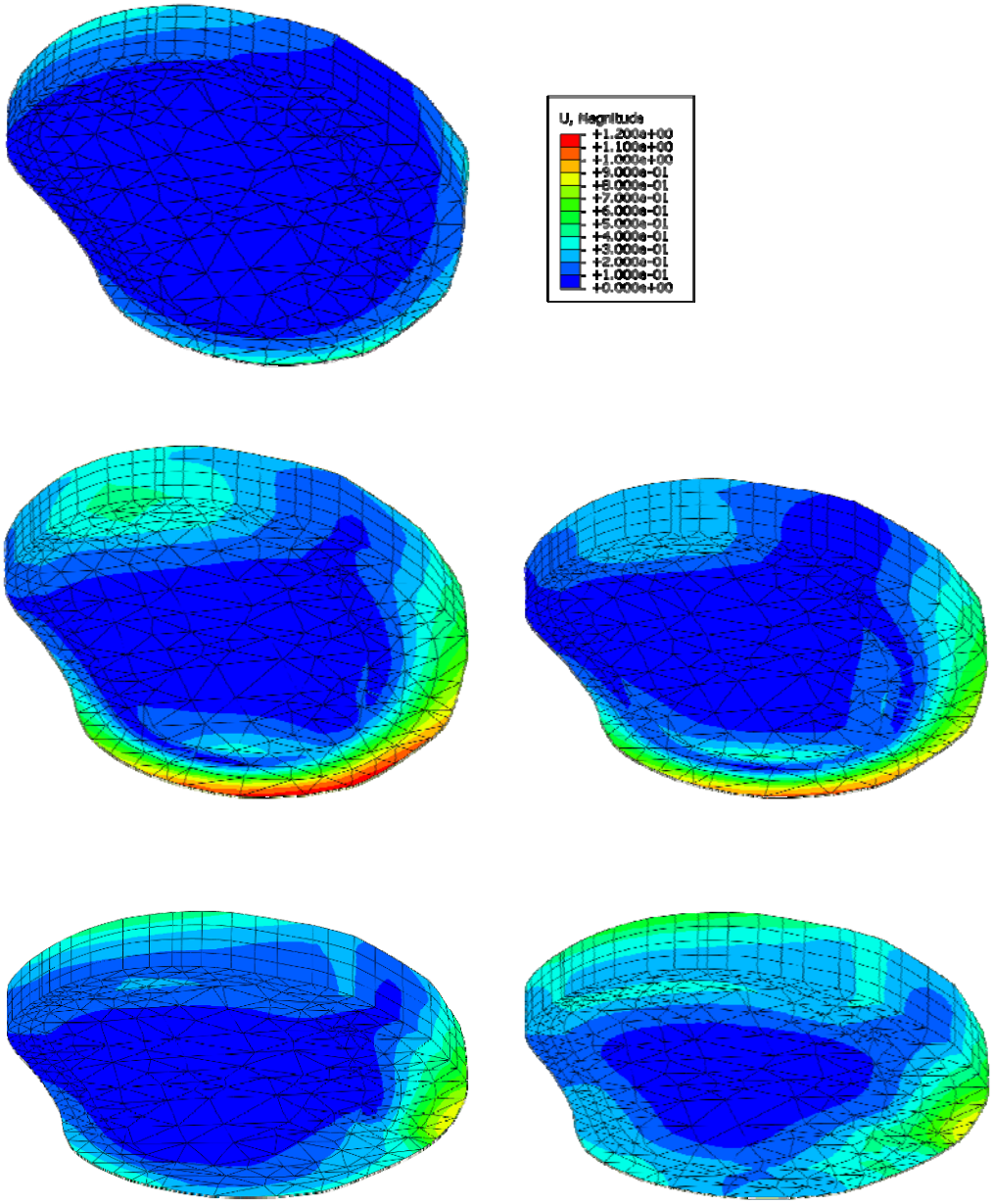

Figure 3.14. Fringe plots of ***lateral bend*** total displacement (a) single zone, Mooney Rivlin; (b) 1 zone annulus, linear elastic nucleus; (c) 1 zone annulus, Mooney Rivlin nucleus; (d) 4 zone annulus, linear elastic nucleus; (e) 4 zone annulus, Mooney Rivlin nucleus

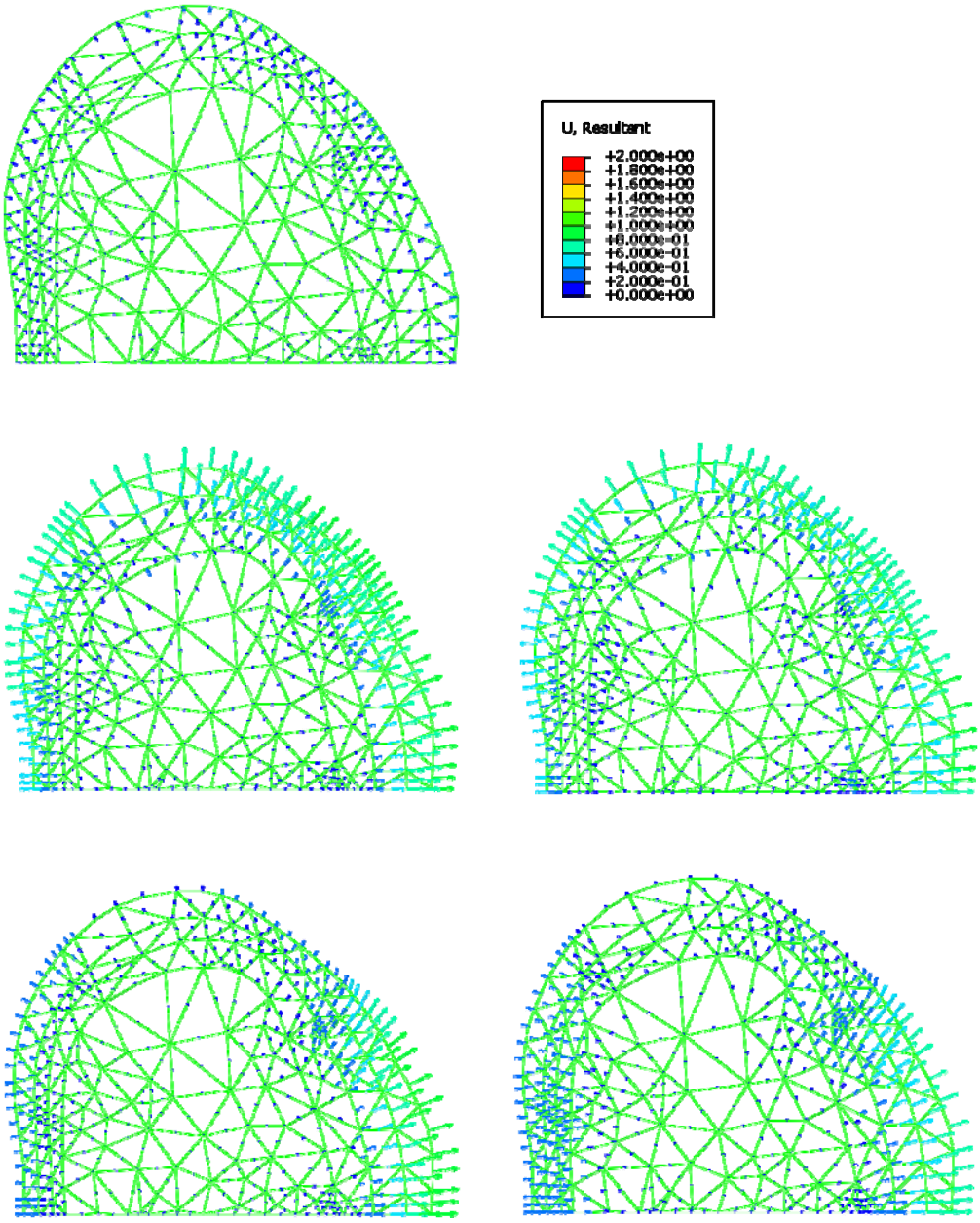

Figure 3.15. Vector plots of ***compression*** total displacement (a) single zone, Mooney Rivlin; (b) 1 zone annulus, linear elastic nucleus; (c) 1 zone annulus, Mooney Rivlin nucleus; (d) 4 zone annulus, linear elastic nucleus; (e) 4 zone annulus, Mooney Rivlin nucleus

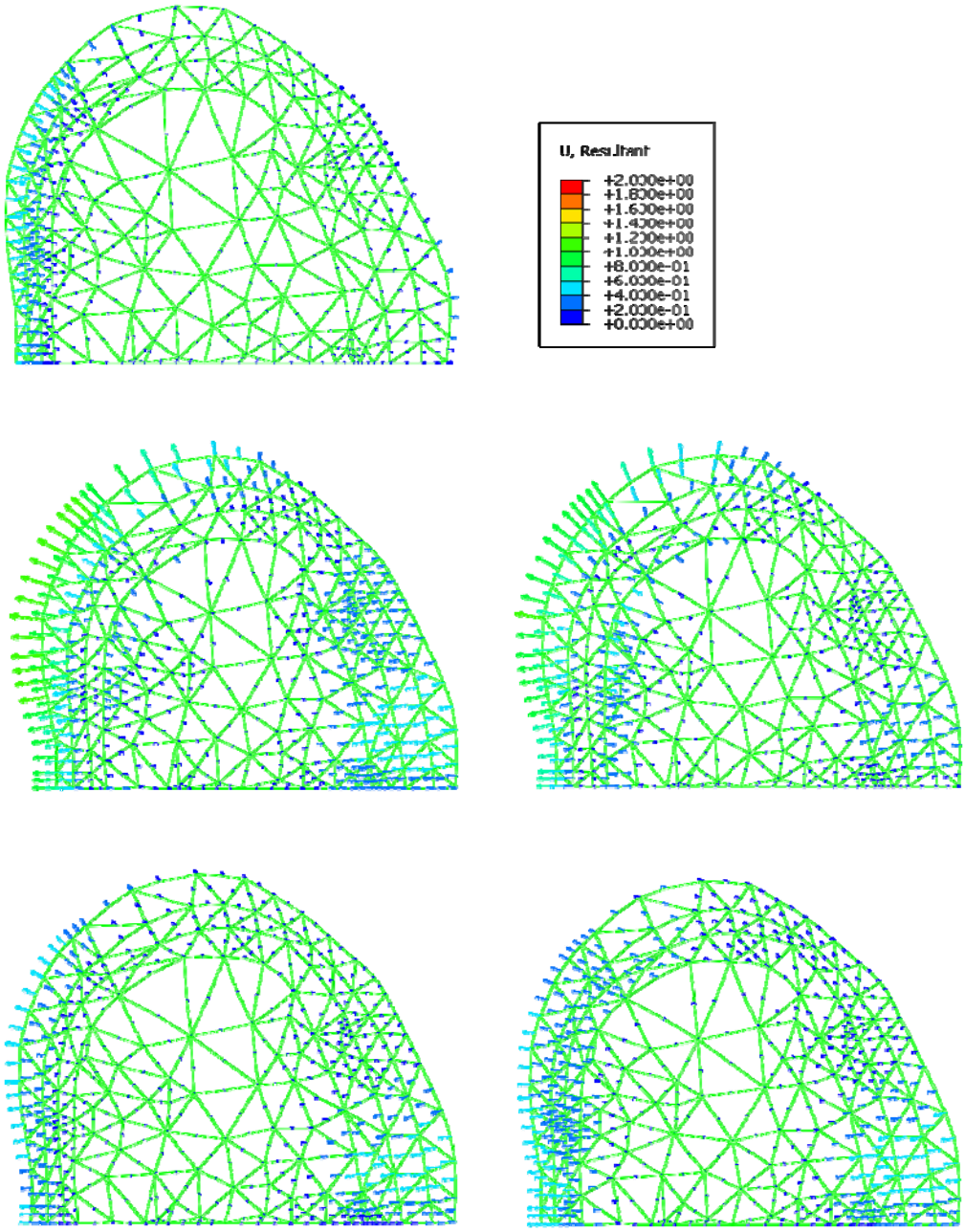

Figure 3.16. Vector plots of ***extension*** total displacement (a) single zone, Mooney Rivlin; (b) 1 zone annulus, linear elastic nucleus; (c) 1 zone annulus, Mooney Rivlin nucleus; (d) 4 zone annulus, linear elastic nucleus; (e) 4 zone annulus, Mooney Rivlin nucleus

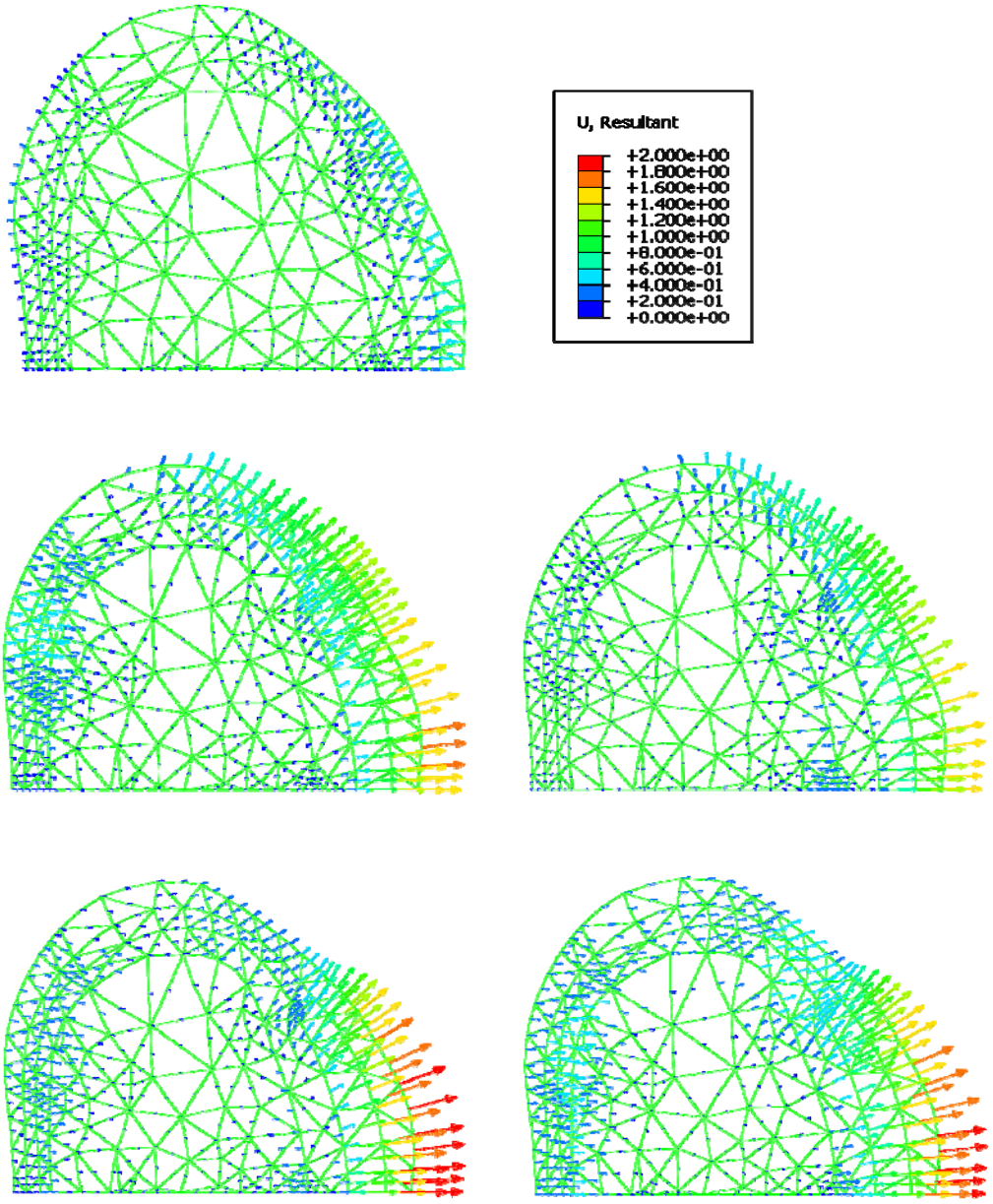

Figure 3.17. Vector plots of ***flexion*** total displacement (a) single zone, Mooney Rivlin; (b) 1 zone annulus, linear elastic nucleus; (c) 1 zone annulus, Mooney Rivlin nucleus; (d) 4 zone annulus, linear elastic nucleus; (e) 4 zone annulus, Mooney Rivlin nucleus

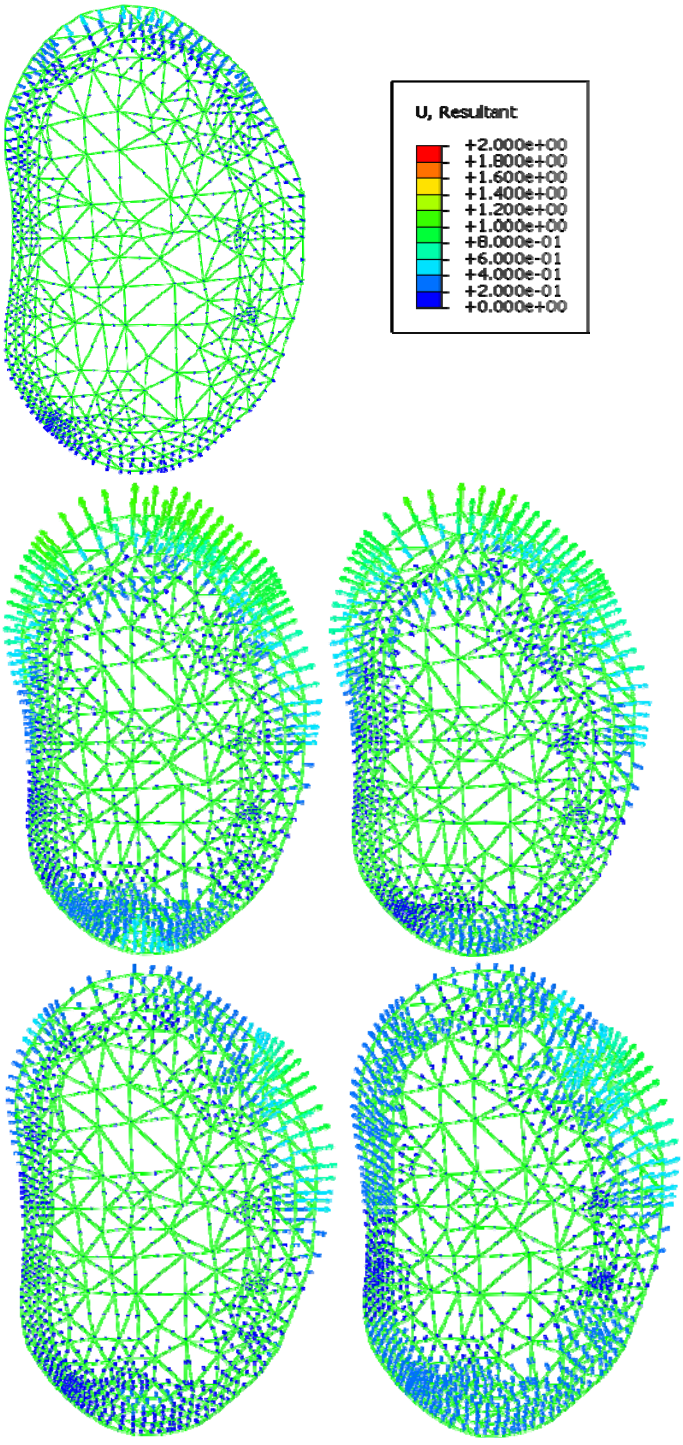

Figure 3.18 Vector plots of ***lateral bend*** total displacement (a) single zone, Mooney Rivlin; (b) 1 zone annulus, linear elastic nucleus; (c) 1 zone annulus, Mooney Rivlin nucleus; (d) 4 zone annulus, linear elastic nucleus; (e) 4 zone annulus, Mooney Rivlin nucleus

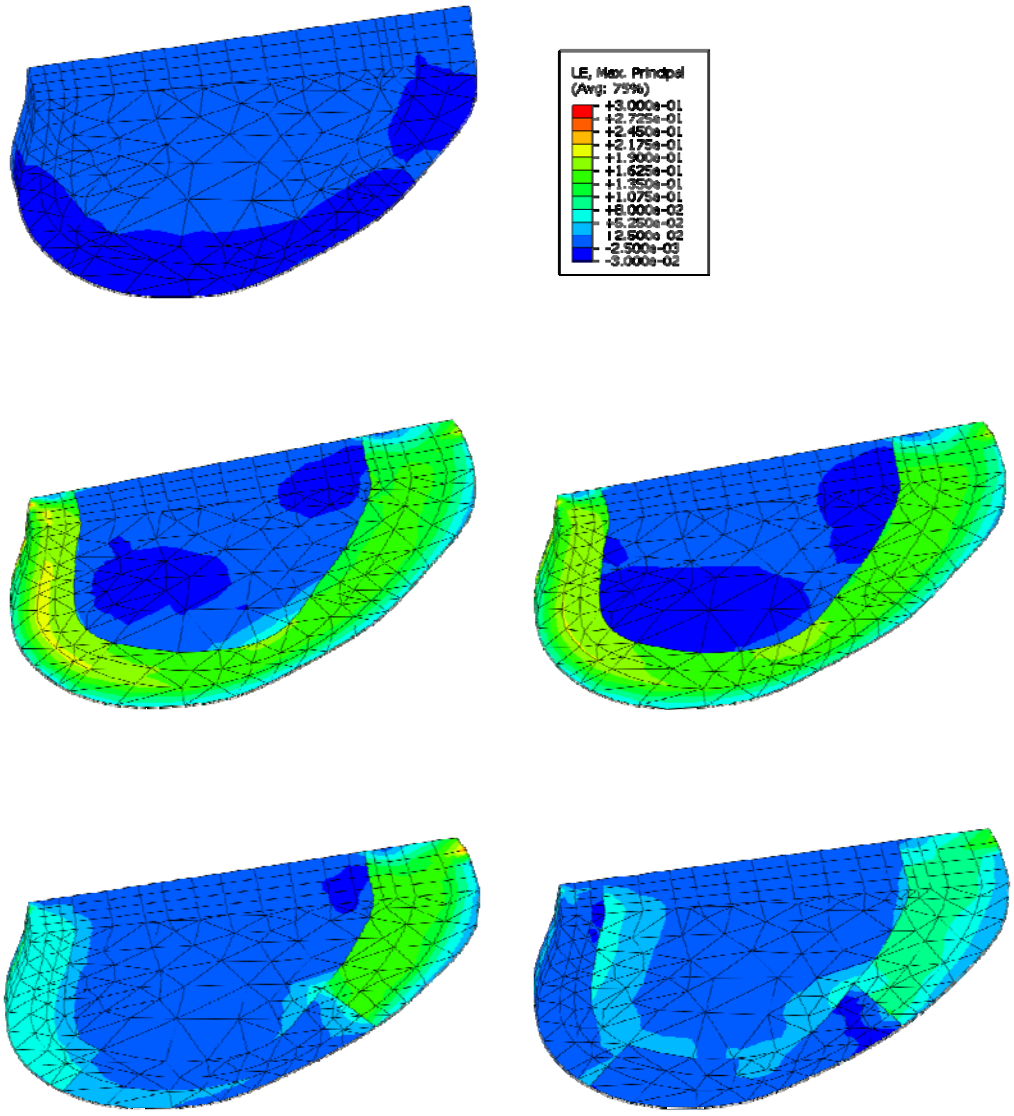

Figure 3.19. Fringe plots of ***compression*** maximum principal strain (a) single zone, Mooney Rivlin; (b) 1 zone annulus, linear elastic nucleus; (c) 1 zone annulus, Mooney Rivlin nucleus; (d) 4 zone annulus, linear elastic nucleus; (e) 4 zone annulus, Mooney Rivlin nucleus

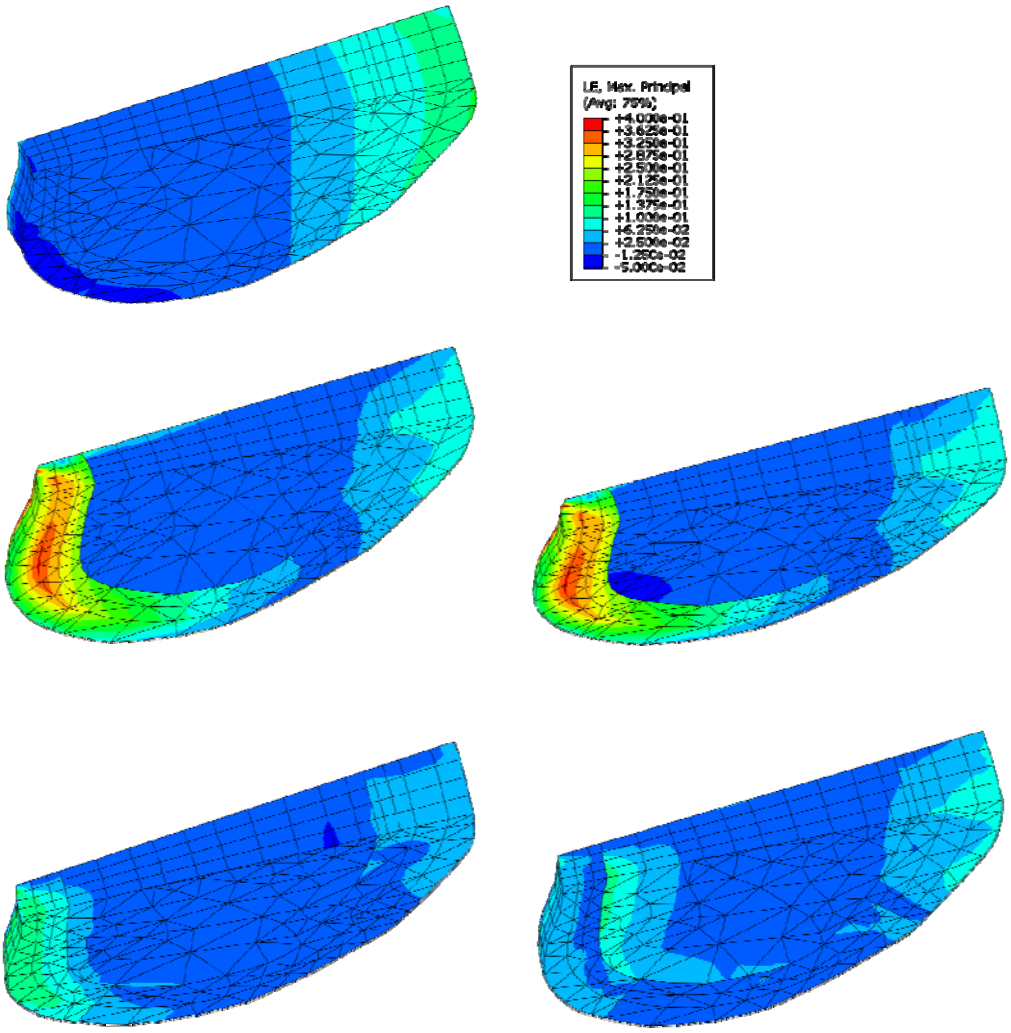

Figure 3.20. Fringe plots of ***extension*** maximum principal strain (a) single zone, Mooney Rivlin; (b) 1 zone annulus, linear elastic nucleus; (c) 1 zone annulus, Mooney Rivlin nucleus; (d) 4 zone annulus, linear elastic nucleus; (e) 4 zone annulus, Mooney Rivlin nucleus

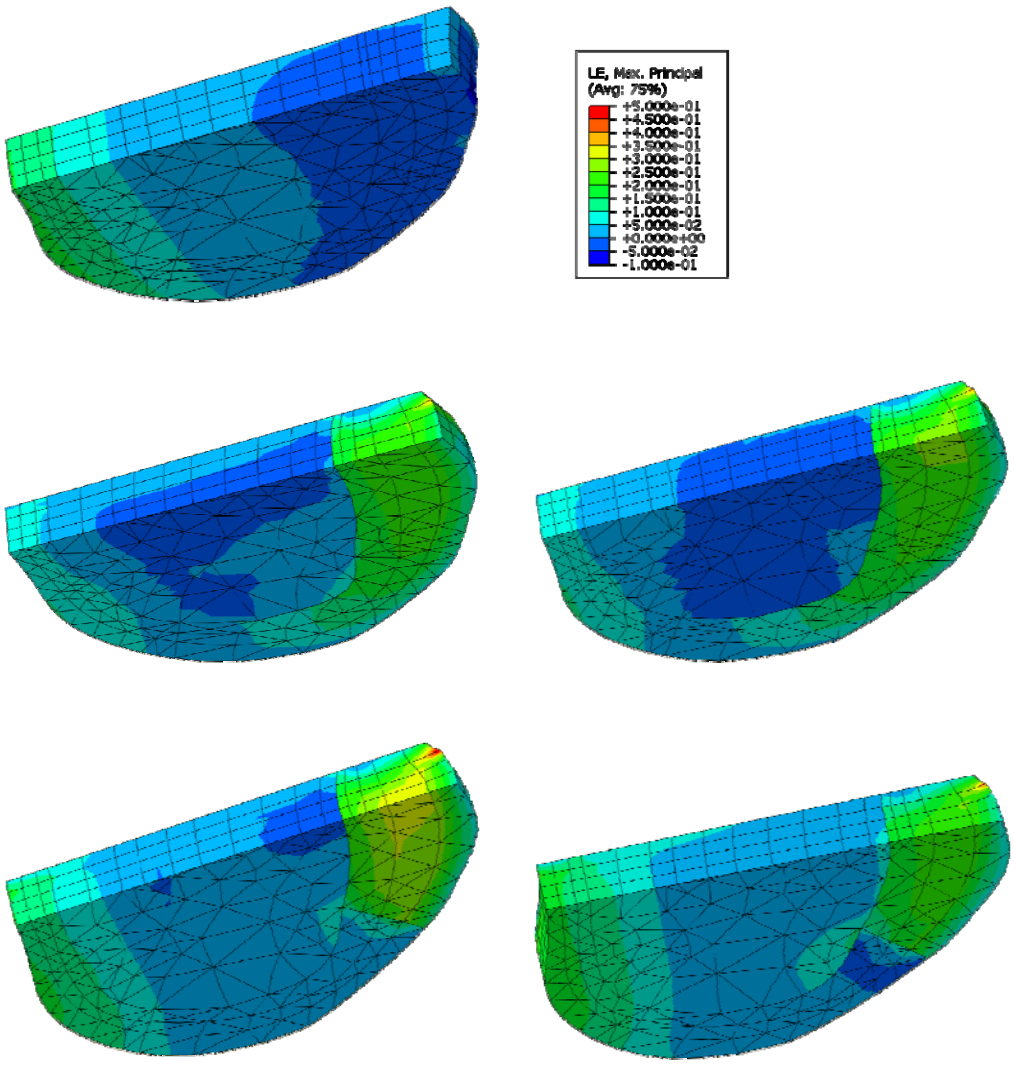

Figure 3.21. Fringe plots of ***flexion*** maximum principal strain (a) single zone, Mooney Rivlin; (b) 1 zone annulus, linear elastic nucleus; (c) 1 zone annulus, Mooney Rivlin nucleus; (d) 4 zone annulus, linear elastic nucleus; (e) 4 zone annulus, Mooney Rivlin nucleus

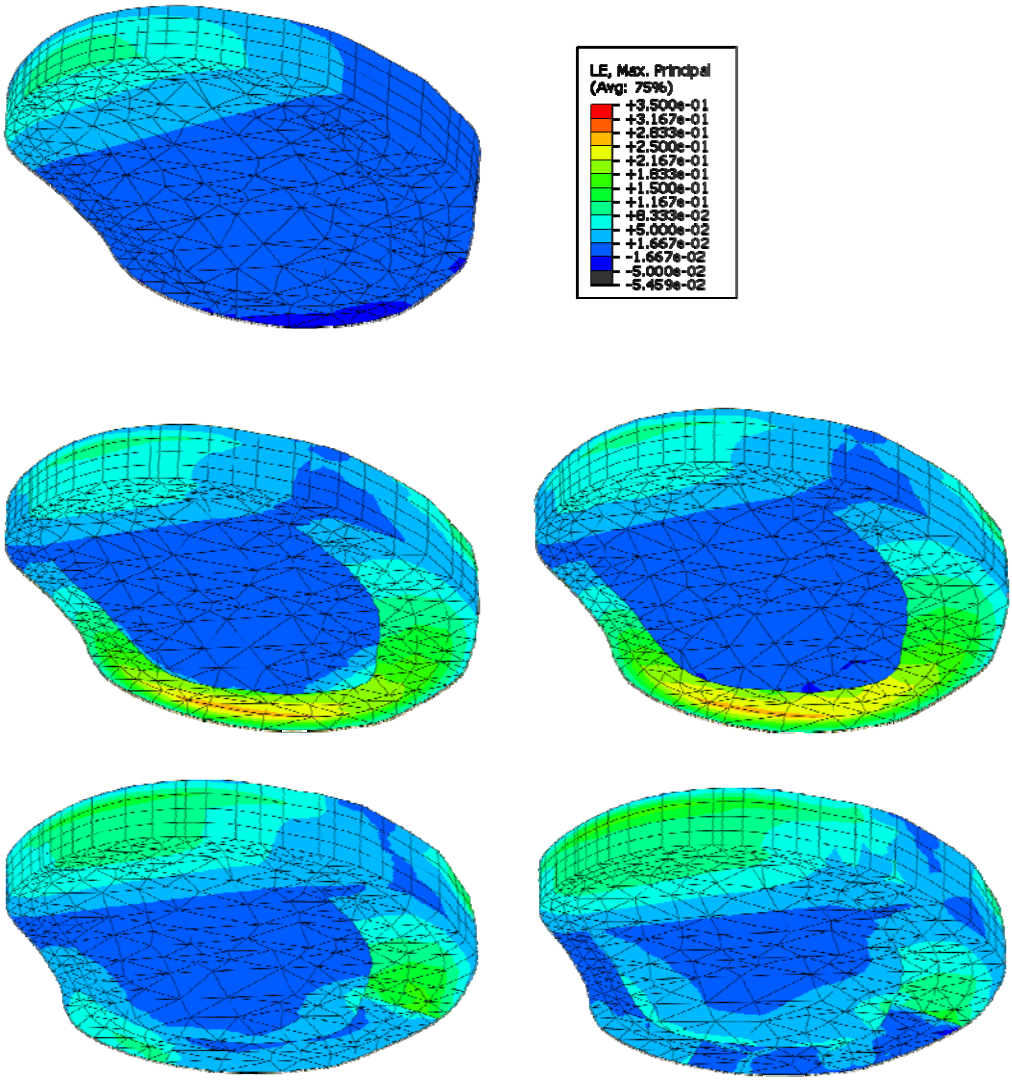

Figure 3.22. Fringe plots of ***lateral bend*** maximum principal strain (a) single zone, Mooney Rivlin; (b) 1 zone annulus, linear elastic nucleus; (c) 1 zone annulus, Mooney Rivlin nucleus; (d) 4 zone annulus, linear elastic nucleus; (e) 4 zone annulus, Mooney Rivlin nucleus

Table 3.1. Loading Conditions of full and symmetric disc FE models

Loading	Full Model	Symmetry Model	Mechanical Test
Compression (Z)	NA	-500N	-1000N
Compression (Z) Extension (Y)	NA	-250N -5Nm	-500N -10Nm
Compression (Z) Flexion (Y)	NA	-250N +5Nm	-500N 10Nm
Compression (Z) Lateral Bend Left (X)	-500N -10Nm	NA	-500N -10Nm

Table 3.2. Constitutive model combinations for disc FE models

Nucleus		Annulus			Total Params
Model	Params	Model	Zones	Params	
Mooney Rivlin, 1 zone					3
Linear Elastic	2	Holzapfel-Gasser-Ogden	1	4	6
Mooney Rivlin	3	Holzapfel-Gasser-Ogden	1	4	7
Linear Elastic	2	Holzapfel-Gasser-Ogden	4	12	14
Mooney Rivlin	3	Holzapfel-Gasser-Ogden	4	12	15

Table 3.3. Summary results of objective function and penalty

Nucleus Model	Annulus Model		Total Parameters	Objective (mm^2)	Penalty (deg^2)
	Model	Zones			
Mooney Rivlin, 1 zone			3	116.75	680.367
Linear Elastic	Holzapfel-Gasser-Ogden	1	6	64.60	332.475
Mooney Rivlin	Holzapfel-Gasser-Ogden	1	7	66.17	327.583
Linear Elastic	Holzapfel-Gasser-Ogden	4	14	63.08	0.353
Mooney Rivlin	Holzapfel-Gasser-Ogden	4	15	63.99	0.260
Optimized using Target Angles Only					
Linear Elastic	Holzapfel-Gasser-Ogden	4	14	68.82	NA

Table 3.4. Summary of resulting constitutive model parameters (best combination highlighted in green)

Nucleus		Annulus			
Model	Parameters	Model	Anterior Zone Parameters	Posterior Zone Parameters	Lateral Zone Parameters
Mooney Rivlin, 1 zone C_{10}=2.164 C_{01}=0.915 D_1=13.82					
Linear Elastic	E=0.891 ν=0.353	Holzapfel-Gasser-Ogden	C_{10}=0.670 D=0.140 k_1=4244.154 k_2=3447.690		
Mooney Rivlin	C_{10}=0.449 C_{01}=0.188 D_1=2.477	Holzapfel-Gasser-Ogden	C_{10}=0.602 D=0.137 k_1=3209.385 k_2=3422.131		
Linear Elastic	E=2.157 ν=0.309	Holzapfel-Gasser-Ogden	C_{10}=0.599 D=0.021 k_1=2471.502 k_2=4038.602	C_{10}=0.820 D=0.563 k_1=673.162 k_2=2102.363	C_{10}=1.073 D=0.747 k_1=2529.938 k_2=1136.286
Mooney Rivlin	C_{10}=0.532 C_{01}=0.035 D_1=0.348	Holzapfel-Gasser-Ogden	C_{10}=0.724 D=0.070 k_1=5806.976 k_2=42.082	C_{10}=0.837 D=0.947 k_1=1659.986 k_2=701.009	C_{10}=0.948 D=1.993 k_1=4848.033 k_2=4836.927

Table 3.5. Linear Elastic and Mooney Rivlin Material Properties from Literature

Nucleus Pulposis			Annulus Fibrosis				Ref.
Linear Elastic			Linear Elastic				
E (MPa)		ν	E (MPa)	ν	Fibers E (MPa)	Fiber ν	
$1x10^{-6}$ to 4.0		0.5	1.2 to 50	0.4 to 0.45	175 to 550	0.3 to 0.5	Dooris et al. 2001 Goel et al. 2005 Bono et al. 2007 Lu et al. 1996 Tuang et al. 2009 Evans et al. 2003
Mooney Rivlin			Mooney Rivlin				Ref.
C10	C01	D1	C10	C01	D1	Fibers E (MPa)	Fiber ν	
0.12 to 0.19	0.03 to 0.09	1	0.18 to 0.56	0.045 to 0.14	1	Non linear	NA	Xiao et al. 2012 Shmidt et al. 2006 Shmidt et al. 2007 Smit 1996

CHAPTER 4 – QUANTIFYING VARIABILITY IN LUMBAR L4-L5 SOFT TISSUE PROPERTIES FOR USE IN FINITE ELEMENT ANALYSIS

4.1 Background and Motivation

Chapter 4 summarizes a comprehensive review of the properties of the L4-L5 structures to develop a probabilistic representation and characterize variability in the stiffness of spinal ligaments and parameters of a Holzapfel-Gasser-Ogden constitutive material model of the disc. Soft tissue structures of the L4-L5 level of the human lumbar spine are represented in finite element models, which are used to evaluate spine biomechanics and implant performance. These models typically use average properties; however, experimental testing reports variation up to 40% in ligament stiffness and even greater variability for annulus fibrosis properties. Probabilistic approaches enable consideration of the impact of intersubject variability on model outputs. However, there are challenges in directly applying the variability in measured load-displacement response of structures to a finite element model. The resulting probabilistic representation can be utilized to include intersubject varability in biomechanics evaluations.

4.2 Introduction

Computational representations of the human lumbar spine have been developed to investigate spine biomechanics (Guan et al., 2006, Schmidt et al., 2007, Wong et al.,

2003, Eberlein et al., 2004, Ayturk et al., 2011, Ezquerro et al., 2011) and spinal implant performance (Dooris et al., 2001, Rohlmann et al., 2005, Chiang et al., 2006, Bono et al., 2007, Xiao et al., 2012, Bowden et al., 2008). The biomechanics measures assessed typically include torque-rotation response, facet contact, disc pressure, and annulus strain. Most of these studies have used a deterministic model with subject-specific anatomic geometry from medical image data. In some cases, the soft tissue representation is based on tissue tests from the same subject; but in many cases, the soft tissue properties are defined from other data found in literature.

Previous studies have used probabilistic techniques, such as a Monte Carlo method, to capture the impact of variability in spinal biomechanics. In general, the approach represents all of the input parameters as distributions and predicts output distributions and bounds of performance, while also identifying the sensitivity factors indicating which input parameters were most influential. Lee and Teo (Lee and Teo, 2005) defined variability of the soft tissue properties by summarizing values from other finite element (FE) models found in literature. Barnes et al. used statistical shape modeling to define variability in the anatomic geometry and also used published FE models to define soft tissue variability (Barnes et al., 2011). Work has also been done on modeling the failure of a vertebral body based on the variability of stress measures in the bone (Rohlmann et al., 2010, Ahmad et al., 2010). In addition, probabilistic studies have been performed by varying the location of a total disc replacement (TDR) in the disc space and key geometric features of the TDR (Rohlmann et al., 2009). Probabilistic representations of soft tissue structures have not been previously developed for the

ligaments and intravertebral disc, but have been implemented in other joints, such as the structures of the knee (Baldwin et al., 2009).

Average experimental results are typically applied in FE models. While experimental data captures intersubject variability (via standard deviations), in some cases, there is not a direct way to apply the variability in a finite element model. For example, in the annulus fibrosis, the load-displacement behavior is a function of multiple input parameters. Accordingly, the objective of this study was to perform a comprehensive review of the properties and their variability for the soft tissue structures of the L4-L5 level of the lumbar spine and to develop a probabilistic representation describing variation in the ligaments and annulus fibrosis (AF) that can be implemented in FE models. The approach utilized published data based on direct mechanical testing of these soft tissue structures. The data was based on heathy subjects and the L4-L5 level as much as possible. FE models replicating the experiments were employed to develop material representations that reproduced the scatter in the experimental data. The novel aspects of this study are the comprehensive summary of the mechanical properties of the various structures and the intermediate modeling of the annulus test specimens to enable variability in measured test results to be considered in the material representations required for a FE analysis. Importantly, the demonstrated probabilistic framework enables consideration of the impact of intersubject variability in a variety of joint mechanics and implant evaluations.

4.2 Methods

A literature search was performed to summarize direct mechanical test measurements of spinal ligaments and the AF. The focus was on the L4-L5 level of the human lumbar spine. In some cases (as noted), data from other levels were used if the L4-L5 was not available.

4.2.1 Ligament Properties

The seven spinal ligaments were considered: anterior lateral ligament (ALL), posterior lateral ligament (PLL), ligamentum flavum ligament (LFL), facet capsular ligament (FCL), intertransverse ligament (ITL), interspinous ligament (ISL), superspinous ligament (SSL). A mean and standard deviation of the force-displacement curves was determined from several sources. For ligaments with data from multiple literature sources, the mean was weighted based on the number of specimens in each source. The standard deviation also accounted for the number of specimens by calculating a pooled variance. For convenience, each ligament was defined by a single stiffness parameter, which was used to define the slope of the load-displacement behavior. Two inflection points were added to describe the toe-in region. The inflection points were defined to adjust as a function of the single stiffness parameter. The stiffness was defined using ligament lengths from a previous FE model, which was based on a healthy L4-L5 FSU from a 33 year old male subject, with none to mild disc degeneration. The ligament lengths for this model were 12.2mm, 11.1mm, 21.4mm, 1.4mm, 30.2mm, 13.3mm, and 23.7mm for the ALL, PLL, LFL, FCL, ITL, ISL and SSL, respectively. In

some cases, test specimens were much longer or shorter than the model ligaments and the stiffness was adjusted for this FE model as described below.

The ALL was defined from three sources. The first source (Neumann et al., 1992) tested 6 healthy ligaments as summarized in Table 4.1. The stress-strain data was converted to load-displacement data from the most linear portion of the data using the cross sectional area of the ligaments and initial length based on the mean segment height. The stiffness was then calculated. The second source (Pintar et al., 1992) tested 25 ligaments at the L4-L5 level and reported stiffness directly. The third source (Chazal et al., 1985) tested 2 ligaments at the L4-L5 level (80 and 63 years) and reported a mean and standard deviation of the force and displacement of the inflection point and a point past the inflection point. This data for the inflection point was used to calculate the inflection point of the other two sources.

The PLL was defined from two sources. The first source (Pintar et al., 1992) tested 25 ligaments at the L4-L5 level and reported stiffness directly. The second source (Chazal et al., 1985) tested 2 ligaments at the L3-L4 level (80 and 63 years) and reported a mean and standard deviation of the force and displacement of the inflection point and a point past the inflection point. This data for the inflection point was used to calculate the inflection point of the other source.

The LFL was also defined from the same two sources. The first source (Pintar et al., 1992) tested 22 ligaments at the L4-L5 level and reported stiffness directly. The second source (Chazal et al., 1985) tested only 1 ligament at the L3-L4 level (60 years) and reported the force and displacement of the inflection point and a point past the

inflection point. Again, this data for the inflection point was used to calculate the inflection point of the other source.

The FCL was only defined from one source (Pintar et al., 1992), which tested 24 ligaments at the L4-L5 level and reported stiffness directly. The toe was defined as 0.75mm and the toe in stiffness and secondary stiffness ratio was 32/98.86 = 0.32N/mm (White and Panjabi, 1990).

Only one source was found for the ITL that reported data measured directly from testing, but the ITL is not reported to be biomechanically significant in the lumbar spine (White and Panjabi, 1990). Chazal et al. (Chazal et al., 1985) tested 2 ligaments of the thoracic spine at the T7-T8 level (30 years) and at the T9-T10 level (30 years) and reported a mean and standard deviation of the force and displacement of the inflection point and a point past the inflection point. The stiffness was adjusted based on the ITL length of 30.24mm for the subject-specific FE model. However, other lengths could be used based on the anatomy of the subject.

The ISL was defined from three sources. The first source (Pintar et al., 1992) tested 18 ligaments at the L4-L5 level and reported stiffness directly. The second source (Chazal et al., 1985) tested 5 ISL and SSL combined ligaments at the L4-L5 level (40, 40, 60, 63 and 73 years) and reported a mean and standard deviation of the force and displacement of the inflection point and a point past the inflection point. The stiffness was assumed to be equally shared by the ISL and SSL. The third source (Iida et al., 2002) also tested 24 ISL and SSL combined ligaments at the L4-L5 level (18 to 85 years) and reported stiffness directly. The stiffness was adjusted based on the ligament length in

the model compared to ligament length of the test specimens. This was necessary because the ISL is shorter than the SSL when modeled separately.

The SSL was defined from four sources. The first source (Pintar et al., 1992) and the second source (Chazal et al., 1985) were identical to the ISL data because the stiffness was assumed to be half from the ISL and half from the SSL. The third source (Iida et al., 2002) also tested 24 ISL and SSL combined ligaments at the L4-L5 level (18 to 85 years) and reported stiffness directly. The stiffness was adjusted based on the ligament length in the model compared to ligament length of the test specimens. The fourth source (Robertson et al., 2013) tested 3 specimens at the L4-L5 level (50, 56, 67 years) and reported stiffness directly.

4.2.2 Annulus Fibrosis Properties

The test data of the AF was grouped into four quadrants: anterior, posterior, and left and right lateral. The left and right lateral quadrants were assumed to be identical. Again, literature was selected based on direct mechanical testing of the AF. The data was selected based on healthy specimens. Available data at the L4-L5 level was somewhat limited, so data for other disc levels were also considered. Guerin and Elliott (Guerin and Elliott, 2006) reported a mean and standard deviation for modulus and strain data, with transition strain at toe in, based on circumferential loading in the outer anterior part of the AF based on 8 healthy lumbar discs at the L3-L4 and L4-L5 levels (average 49 years, range 25 to 76 years). Guerin and Elliott (Guerin and Elliott, 2006) also directly measured the total fiber included angle (2ϕ) and reported the variation across the 8 discs as $2\phi = 50.87° \pm 8.43°$. Wagner and Lotz (Wagner and Lotz, 2004) reported a stress-

strain function with statistical values for the function parameters based on 11 lumbar discs in circumferential loading in the anterior location at the L2-L3, L3-L4, and L4-L5 levels (6 donors, 16 to 38 years). Fujita et al. (Fijuta et al., 1997) also reported a stress-strain function with statistical values for the function parameters based on 8 lumbar discs in radial loading for the anterior and posterior lateral locations at the L1-L2, L2-L3, L3-L4, and L4-L5 levels (50 to 70 years, grade I). Holzapfel et al. (Holzapfel et al., 2005) reported the mean and standard deviation of a low, medium, and high modulus based on 11 lumbar discs with single lamellar AF specimens loaded along the fiber direction in the anterior-lateral and posterior locations at the L1-L2 level (57.9 ± 15.4 years, 6 grade I and 5 grade II). The specimens were taken from the inner and outer surfaces of the AF and the data was combined in this study. Because a low, medium, and high modulus was reported based on similar loads (and therefore similar stress), the +/-1 standard deviation of strain at that stress level was not symmetric about the mean strain. O'Connell et al. (O'Connell et al., 2009) reported the mean and standard deviation of the toe-in modulus and secondary modulus with a transition strain based on 7 lumbar discs at the L3-L4 and L4-L5 levels (36 to 53 years, grade = 2.2 ± 0.3). The specimens were taken from the anterior area and loaded radially, axially, and circumferentially. Ebara et al. (Ebara et al., 1996) reported a stress-strain function with mean and standard deviation values for the function parameters based on 15 lumbar discs in circumferential loading in the anterior, outer location and the posterior-lateral inner and outer locations at the L3-L4 level (26 to 53 years, grade I and II). When using the -1 standard deviation values of the stress-strain function parameters, the stress became negative. The stress data was truncated at 0 for the -1 standard deviation curves. Some of the literature data was taken from locations

that span two quadrants in the model. For example, data based on a posterior-lateral location was used for the posterior quadrant and the lateral quadrants. Table 4.2 summarizes how each data source was used in the model.

In order to combine the data for each quadrant and for each loading direction, specimen geometry was defined which matched or was in the range of the specimen geometry used in the literature in the cases when several literature sources were used. The lateral and posterior specimens represented the narrow region of the dog bone specimens tested in the literature since the data was based on the gage marks at the ends of this region. The thickness of the single lamellar specimens was defined by Holzapfel et al. (Holzapfel et al., 2005). Table 4.3 summarizes the specimen sizes. The stress-strain data from the literature was then converted to load-displacement data, which was then combined using the same approach for the ligament data. The mean data accounted for the number of specimens in each source. The standard deviation also accounted for the number of specimens by calculating a pooled variance. In all of the data (circumferential, posterior radial, and lateral radial), the load-displacement curve representing -1 standard deviation contained negative load values and was truncated at 0.

4.2.3 Finite Element Modeling of the Annulus Fibrosis

Abaqus (Dassault Systemes, Johnston, RI) FE models were defined for a series of 10 specimens representing combinations of locations and loading directions in the AF (Fig 4.1, Fig. 4.2 and Table 4.3). An orientation was defined in the models for the AF fiber angle, which was 25.4° from the anatomical transverse plane (Guerin and Elliott, 2006) with the exception of the single lamellar models which had fibers aligned along the

specimen in the loading direction. All of the models used hexahedral C3D20 elements. The models were defined with boundary conditions to replicate the testing from the literature sources. The anterior axial, anterior circumferential and all radial models were fully constrained on one end and were displaced on the other end with a kinematic coupling. The lateral and posterior circumferential models had a constraint on one end, which allowed the specimen to shrink or expand along the end surface, and were displaced on the opposite end with a kinematic coupling, which also allowed the end surface to shrink and expand. This simulated the central region of a dog bone specimen between the gage marks measured in the literature. The single lamellar specimens were fully constrained on one end and a load was applied to the opposite end through a kinematic coupling. Displacement was enforced on the specimens and the reaction force was measured except for the single lamellar specimens, which had an applied load and displacement was measured. The Holzapfel-Gasser-Ogden anisotropic, hyperelastic constitutive model was used (Holzapfel et al., 2000, Gasser et al., 2006). The constitutive model has the advantage of mathematically representing the fiber stiffness, direction, and dispersion and has been used in other FE models of the spine (Coombs et al., 2013).

An Isight (Dassault Systemes, Johnstown, RI) workflow was defined to determine the Holzapfel-Gasser-Ogden parameters using direct optimization by minimizing the squared error between the model-predicted load-displacement curves and the literature curves (Fig 4.2). Using a simulated annealing algorithm, the workflow optimized the material parameters for all loading directions in each quadrant. The optimization was performed for the mean curves and the +/- 1 standard deviation curves for a total of 9 workflows. The Holzapfel-Gasser-Ogden constitutive model is defined by five

parameters (C10, D, K1, K2, κ). C10, K1, and K2 were optimized for each quadrant to match the load-displacement curves. C10 represents the stiffness of the ground substance. K1 represents the stiffness of the fibers in the material. K2 determines the nonlinearity of the fiber stiffness. The compressibility parameter, D, was defined as 1/(20*C10), which is equivalent to defining the initial bulk modulus as twenty times the initial shear modulus. This is similar to a Poisson's Ratio of 0.475 or nearly incompressible (Abaqus Users Guide, 2012). The fiber dispersion parameter, κ, was set to 0 assuming the fibers are perfectly aligned to the fiber direction. Therefore, there were three parameters used for this optimization for each quadrant.

A Monte Carlo simulation, with simple random sampling, was then used to account for the parameter distribution and the interaction between parameters. The optimized parameter values (from above) were used as the initial values for a Monte Carlo simulation. Guided by the parameter values from the +/- 1 standard deviation curves, several Monte Carlo simulations, with 100 iterations, were performed to converge on the single set of input parameters to match the mean and +/1 standard deviation force-displacement curves for all of the specimens (loading directions) associated with a specific annulus location (e.g. anterior). The C10 parameter was defined as a lognormal distribution to account for the -1 standard deviation curve being truncated at a force of 0N. An Isight workflow was defined to execute these simulations for each quadrant using a random sampling method, for a total of 3 workflows (Fig. 4.2).

4.3 Results

4.3.1 Ligaments

The largest coefficient of variation (CV) of the stiffness parameter was 0.85 for the PLL, using the +1 standard deviation data by Chazal et al. (Chazal et al., 1985), but was only based on two specimens. Next largest CV was 0.75 for the ISL by Pintar et al. (Pintar et al., 1992), with 18 specimens. The smallest CV was 0.05 for the FCL based on data from Pintar et al. (Pintar et al., 1992). Pintar et al. (Pintar et al., 1992) had data for the most amount of ligament types with a total of 118 specimens. The ITL had the least amount of data with only 2 specimens (Table 4.4). The stiffness +1 standard deviation and -1 standard deviation were reported because the standard deviation was not always symmetric about the mean due to how the data was reported. When combining the mean and standard deviation data, the ALL had the greatest stiffness of 55.36 N/mm, which is between 1.7 and 2.7 times stiffer than the other ligaments. The PLL has the largest CV of 0.64 and the FCL has the smallest CV of 0.05 (Table 4.5).

The force-displacement data can be graphed to visually show the variation for each ligament along with the toe in region. The combined force-displacement data was graphed for the ALL, PLL, LFL, FCL, ITL, ISL and SSL (Fig. 4.3 through 4.10). The solid line represents the mean data and the dashed lines represent +/- 1 standard deviation of the data.

4.3.2 Annulus Fibrosis

For each AF quadrant, the results of the combined load-displacement graphs from the literature showed the variability with the mean and +/- 1 standard deviation curves

(Fig.4.11 through 4.14). The +/- 1 standard deviation curves for the circumferential loading is not exactly symmetric about the mean curve. This is because the -1 standard deviation curves based on the equations from Ebara et al. (Ebara et al., 1996) were truncated at 0 load to prevent the load from becoming unrealistically negative. In addition, the single lamellar +/- 1 standard deviation curves are not symmetric about the mean curves. This is because Holzapfel et al. (Holzapfel et al., 2005) reported mean and standard deviation for a low, medium, and high modulus at the same load levels. The calculated displacement at the same load is not linearly related to the modulus. The resulting Holzapfel-Gasser-Ogden parameters for each quadrant based on the Monte Carlo approach indicate that the load-displacement behavior was most sensitive to the C10 parameter and the anterior quadrant has lowest stiffness (Table 4.6). The final mean and standard deviation parameter values for each quadrant were the best match between the Monte Carlo load-displacement curves and the curves defined by literature (Fig. 4.15 through 4.17).

The root mean squared (RMS) error was greatest for circumferential loading, but this data had greatest load and qualitatively looks best on the load-displacement graphs. The -1 standard deviation curves had lower RMS error than the +1 standard deviation curves in circumferential and radial loading. The opposite was true for single lamellar loading. The graphs show that the posterior quadrant is most stiff and the anterior is least stiff. The C10 parameter indicates this as a representation of the matrix stiffness and the K1 parameter also indicates this as a representation of the fiber stiffness.

Guerin and Elliott (Guerin and Elliott, 2006) reported the fiber included angle (2ϕ) as $2\phi = 50.87° \pm 8.43°$ from the transverse plane.

4.4 Discussion

The objective of this study was to comprehensively represent the variability of soft tissue properties of the L4-L5 level of the lumbar spine and to facilitate its use in FE models. Specifically, a comprehensive summary of mechanical testing was performed and probabilistic representations of the spinal ligaments and AF, including specific regions, were established. The results of this study can be directly applied to FE models of spine mechanics at the L4-L5 level with the potential for the demonstrated probabilistic approach to be implemented at other levels and for other joints.

Best practice in specimen-specific modeling is to use geometry and experimentally measured material properties from the same specimen. However, this is not always practical. For models of living subjects, mechanical property test data is not available. Many studies have merged geometries from one subject or specimen with properties from another specimen or the literature. So, when creating a subject-specific model, the probabilistic representations developed in this study allow a quantitative consideration of the potential impact of intersubject differences in the mechanical properties. The ligament force-displacement data summary can be used directly in FE models by defining the ligaments as non-linear springs. The ALL is the stiffest ligament (Neumann et al., 1992), which agrees with the summarized data.

One of the limitations of this data is that not all ligaments were tested at the L4-L5 level. However, ligaments from other levels were used by assuming similar material and adjusting the stiffness based on the initial ligament length at L4-L5 compared to the other levels. The ligament length should also be considered for FE models and stiffness could be adjusted accordingly.

The donors tested in this study spanned 18 to 85 years, which captures the variability for a large span of ages. Care should be taken when combining the ligament data with the AF data because it was based on healthy discs and the stiffness of ligaments tend to become less stiff with age (Iida et al., 2002). There was little data available for the ITL and only from the thoracic spine. However, the ITL is not as significant as other ligaments (White and Panjabi, 1990).

The AF data was summarized from healthy (grade I and II) lumbar discs with a focus on the L4-L5 level. The data was used to determine variability in parameters for an anisotropic, hyperelastic Holzapfel-Gasser-Ogden constitutive model. This model can be used directly in FE models and provides the benefit of mathematically representing the AF fibers rather than discretely modeling them as elements. Based on a manual optimization approach, using Monte Carlo simulations, it was qualitatively observed that C10 had the greatest effect on the overall force-displacement stiffness. There was also a trade off in matching the curves for each loading direction. For example, in order to improve the single lamellar results, the circumferential results would not match as well. One of the limitations of this data is that other levels were used because data at the L4-L5 level was not always available. Another limitation to the AF data is that the parameters must be treated as independent because the test data was not grouped such that the quadrants could be correlated based on stiffness. A third limitation is that the AF properties are for a healthy normal population. Further work could be done to also characterize properties of degenerated discs and their variation, which may be useful when developing spinal implants. Rohlmann et al. (Rohlmann et al., 2006) showed that

the range of motion generally decreases with increasing degeneration use FE models with correlation to biomechanical testing.

4.4 Conclusion

Variability of the stiffness, defining the force-displacement data, of the ligaments and the parameters of the Holzpafel Gasser-Ogden constitutive model has been summarized based on direct mechanical test data and FE modeling of these soft tissue structures. These parameters can be used to define these structures in an FE model, which represents intersubject variation. The probabilistic representations can be used to perform probabilistic FE studies to assess the variability in output measures such as spine kinematics, implant stress, implant deformation, and other measures. This study focused on soft tissues, which is a key to spine biomechanics. Future studies could also include variability of bony structures to define a more robust probabilistic FE model.

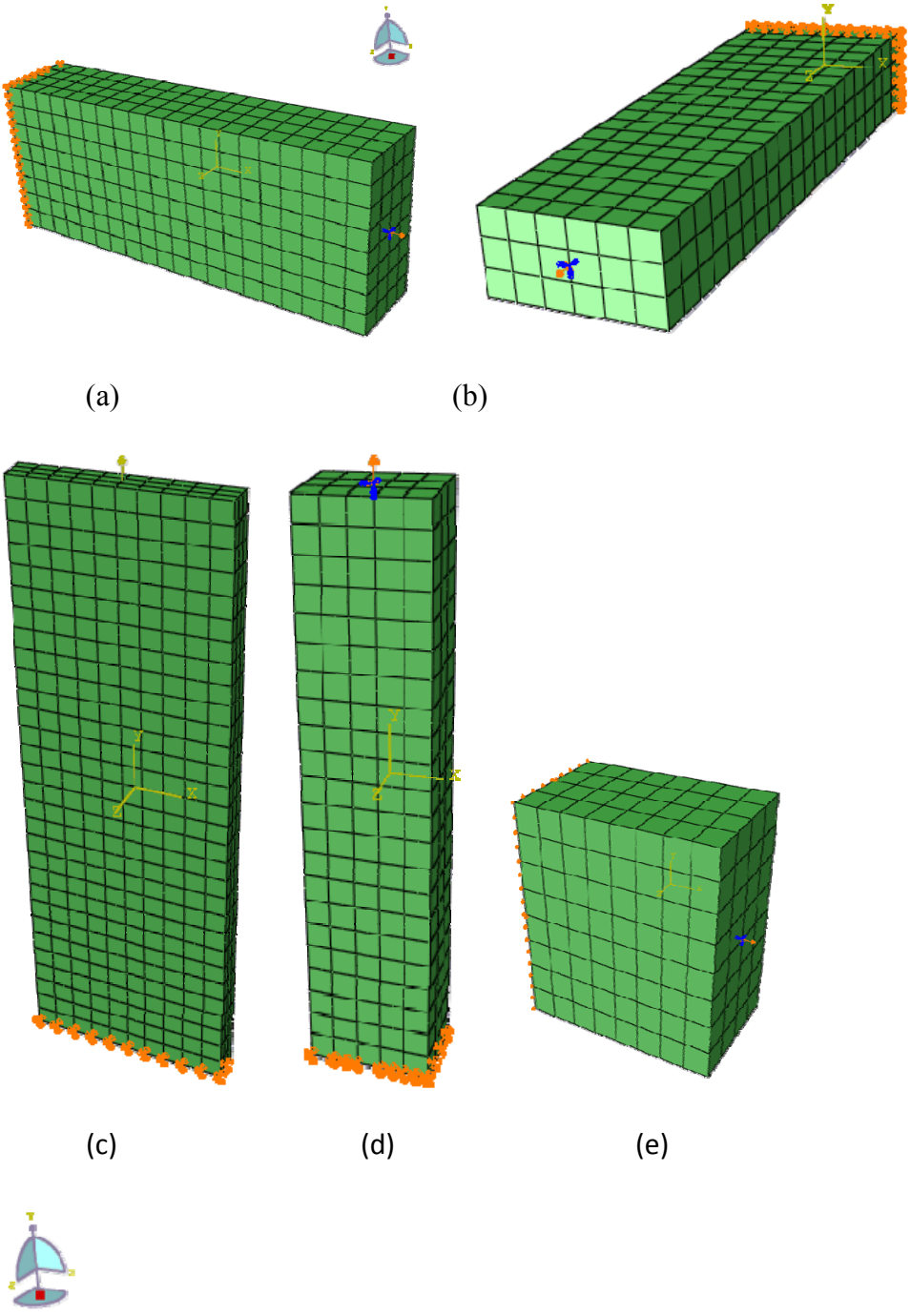

Figure 4.1. Finite element models of annulus fibrosis specimens based on loading direction (a) circumferential; (b) radial; (c) single lamellar; (d) axial; (e) circumferential dog bone specimen

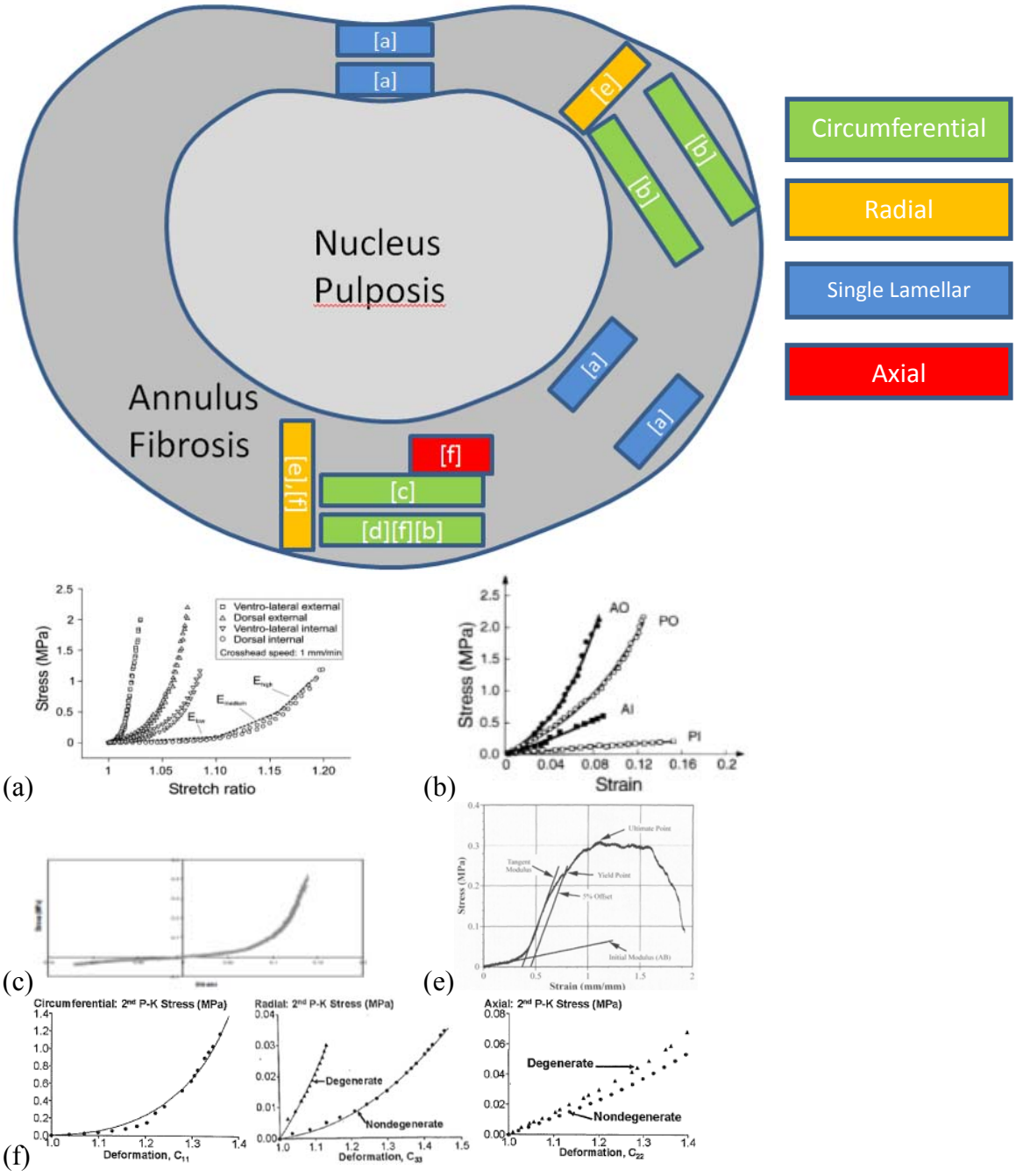

Figure 4.2. Location and loading direction of annulus fibrosis specimens (a) Holzapfel et al. 2005, Posterior inner and outer Anteriolateral inner and outer Single Lamellar Load; (b) Ebara et al., 1996, Anterior Outer Posteriolateral inner and outer Circumferential Load; (c) Wagner et al., 2004, Anterior Circumferential Load; (d) Guerin et al., 2006, Anterior Circumferential Load; (e) Fujita et al., 1997, Anterior Posterolateral, Radial Load; (f) O'Connell et al., 2009, Anterior outer Circumferential Load, Radial Load, Axial Load

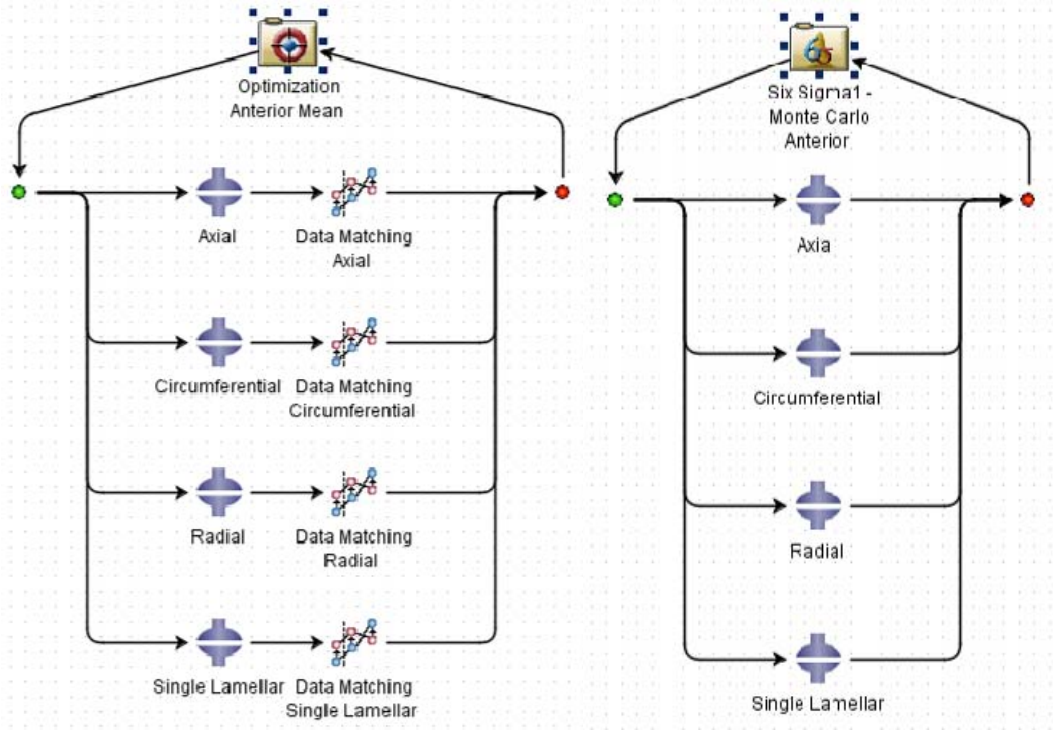

(a) (b)

Figure 4.3. Representative Isight workflows for annulus specimens of the anterior quadrant (a) optimization workflow; (b) Monte Carlo workflow

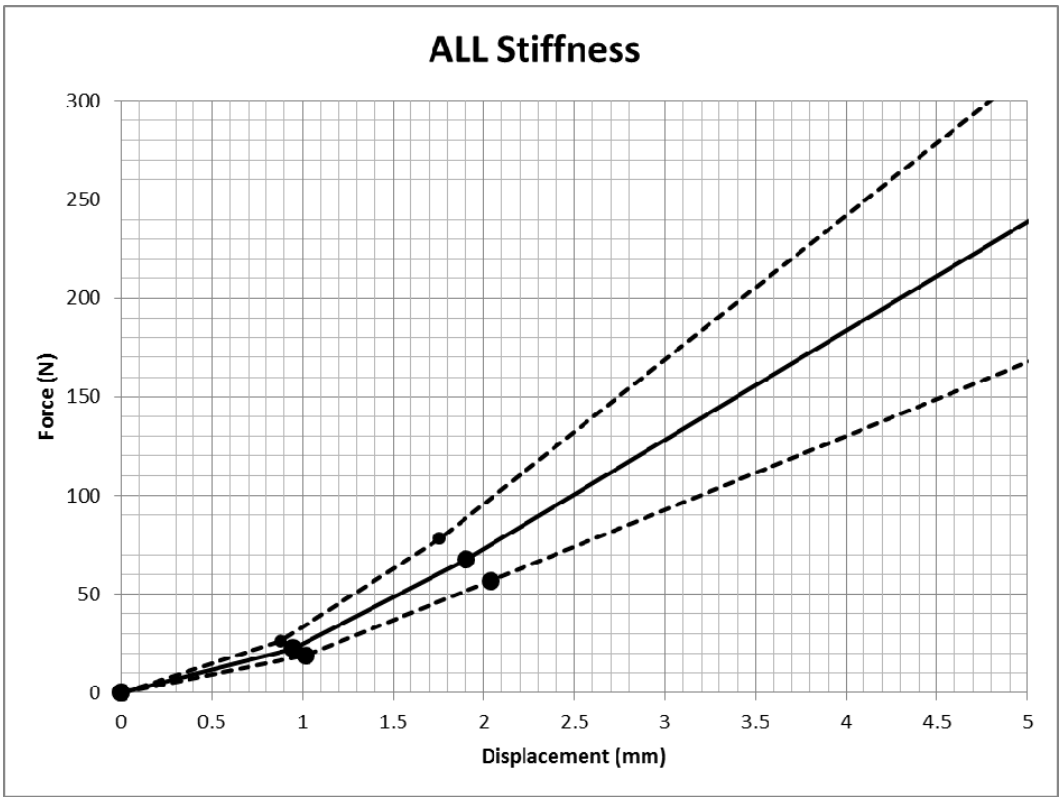

Figure 4.4. Force- displacement graph for ALL with mean and +/-1 standard deviation

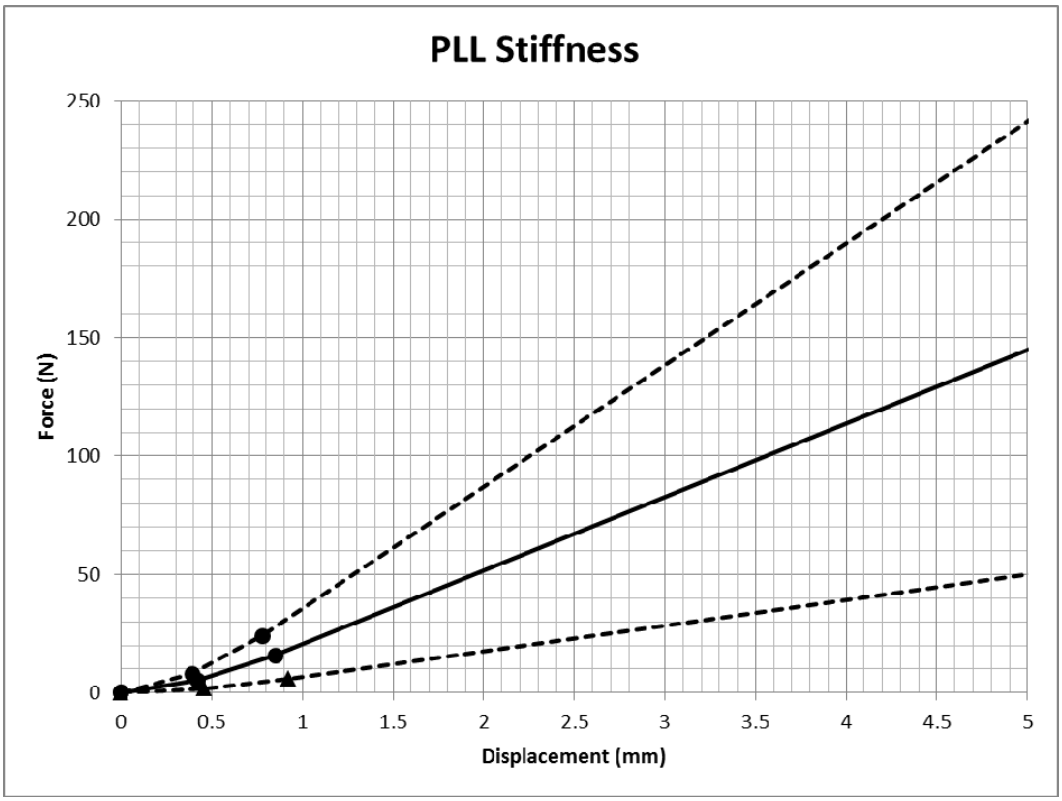

Figure 4.5. Force-displacement graph for PLL with mean and +/-1 standard deviation

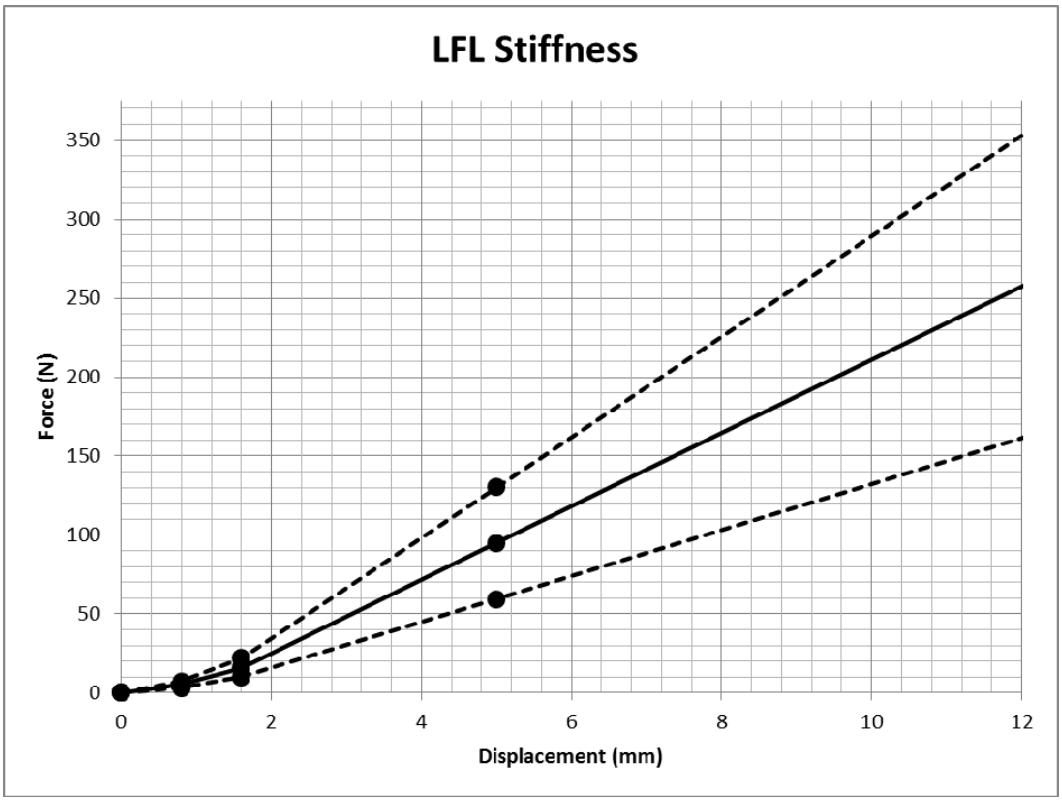

Figure 4.6. Force-displacement graph for LFL with mean and +/-1 standard deviation

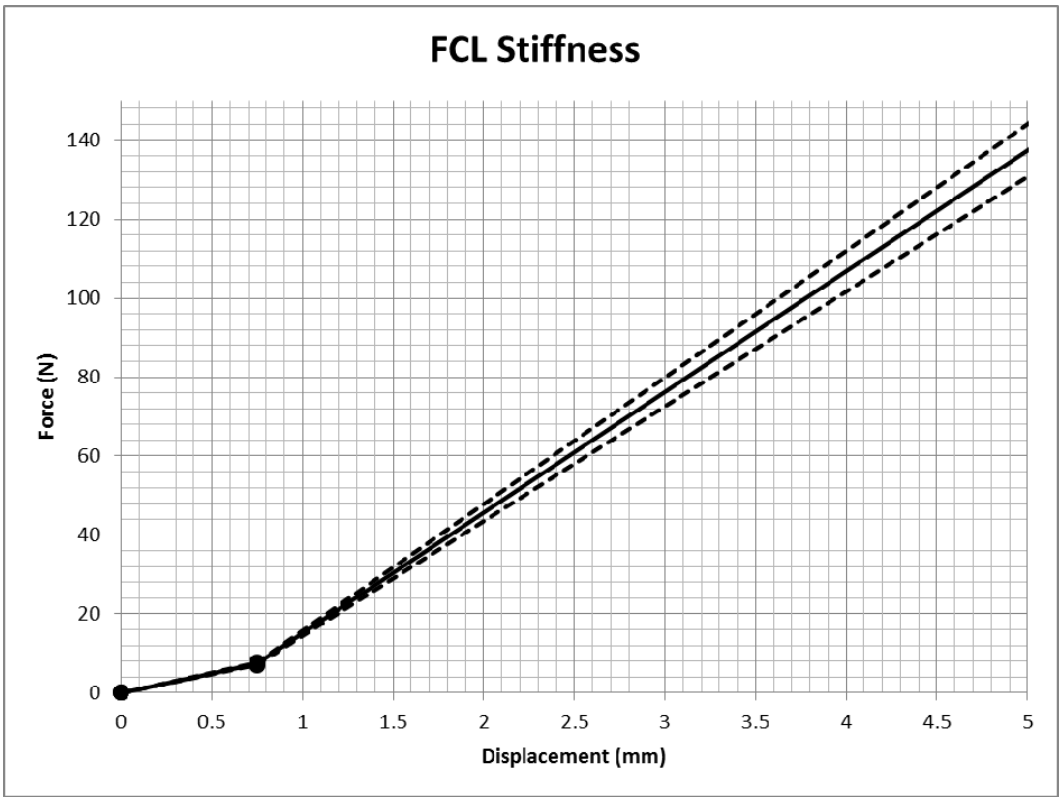

Figure 4.7. Force-displacement graph for FCL with mean and +/-1 standard deviation

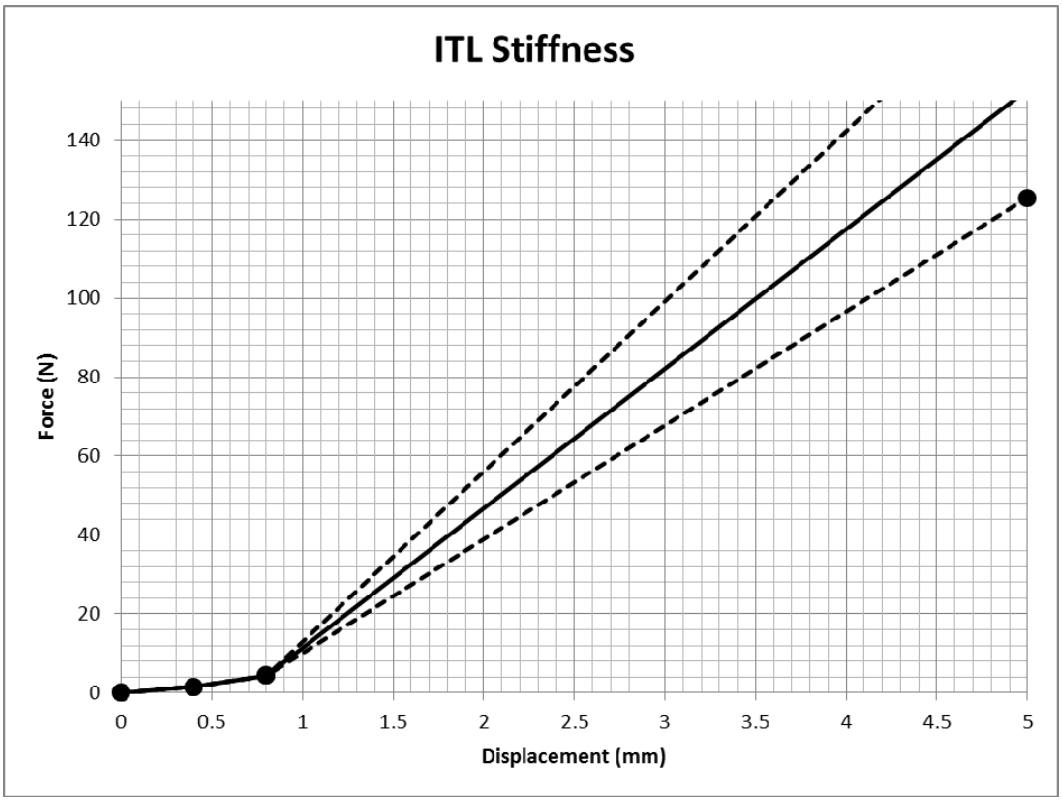

Figure 4.8. Force-displacement graph for ITL with mean and +/-1 standard deviation

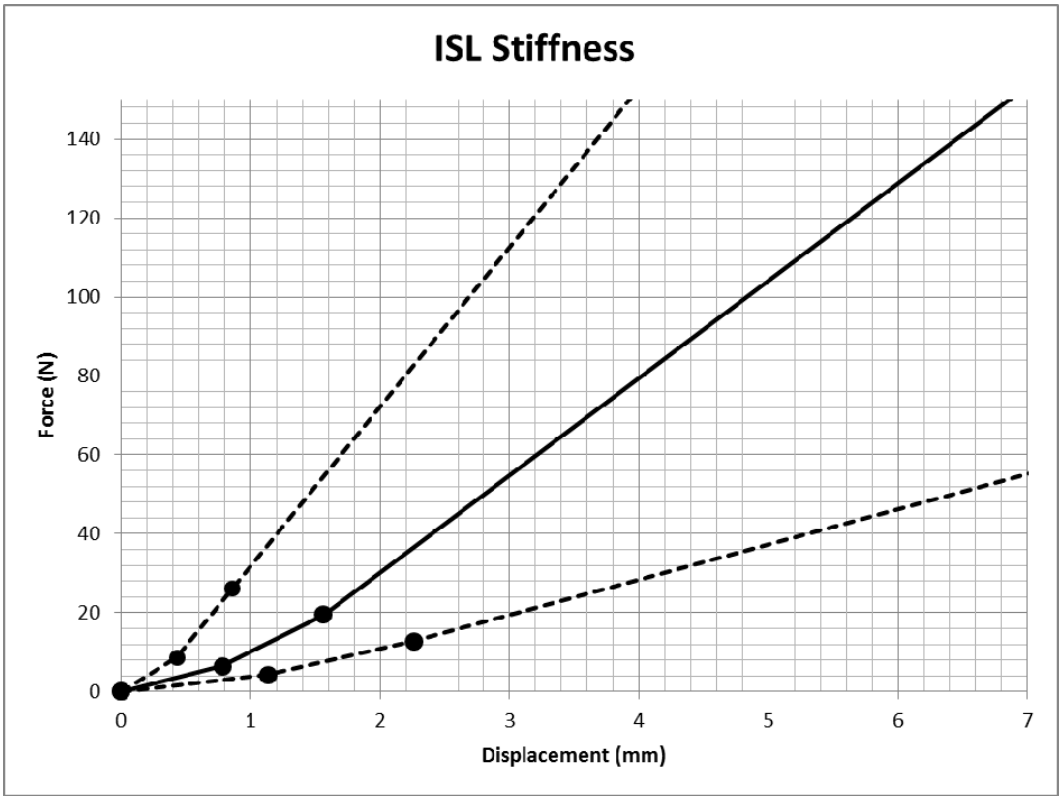

Figure 4.9. Force-displacement graph for ISL with mean and +/-1 standard deviation

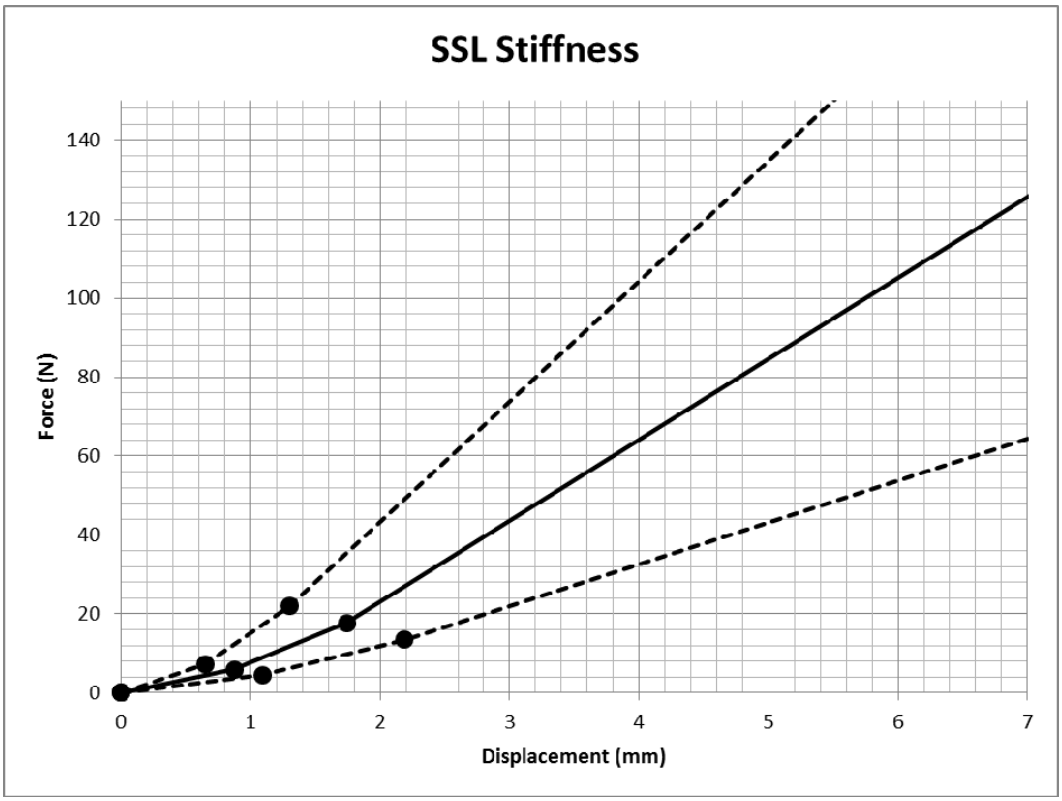

Figure 4.10. Force-displacement graph for SSL with mean and +/-1 standard deviation

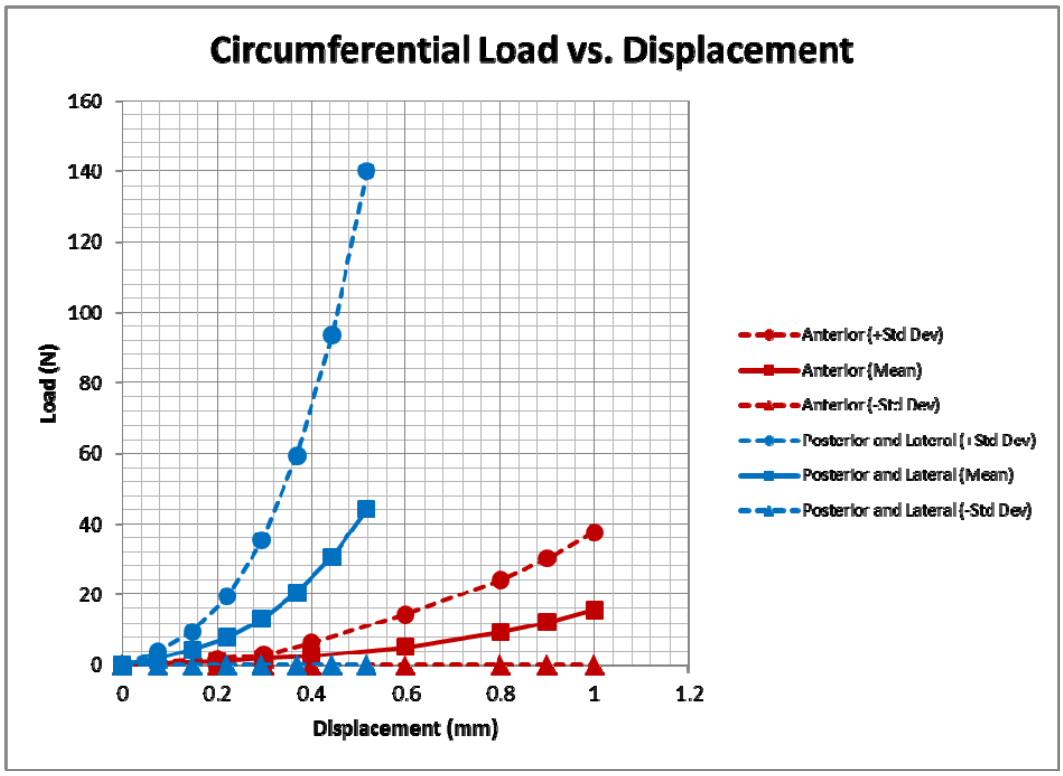

Figure 4.11. Combined force-displacement graph for circumferential loading, anterior and posterior quadrant, mean and +/-1 standard deviation

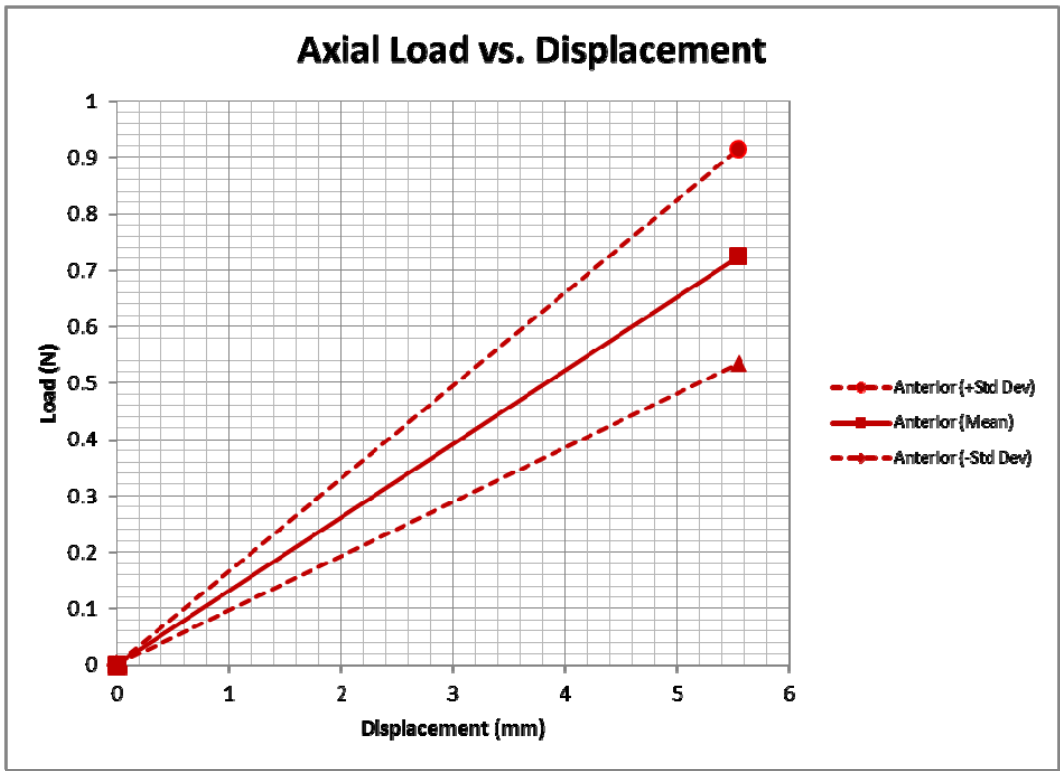

Figure 4.12. Combined force-displacement graph for axial loading, anterior quadrant, mean and +/-1 standard deviation

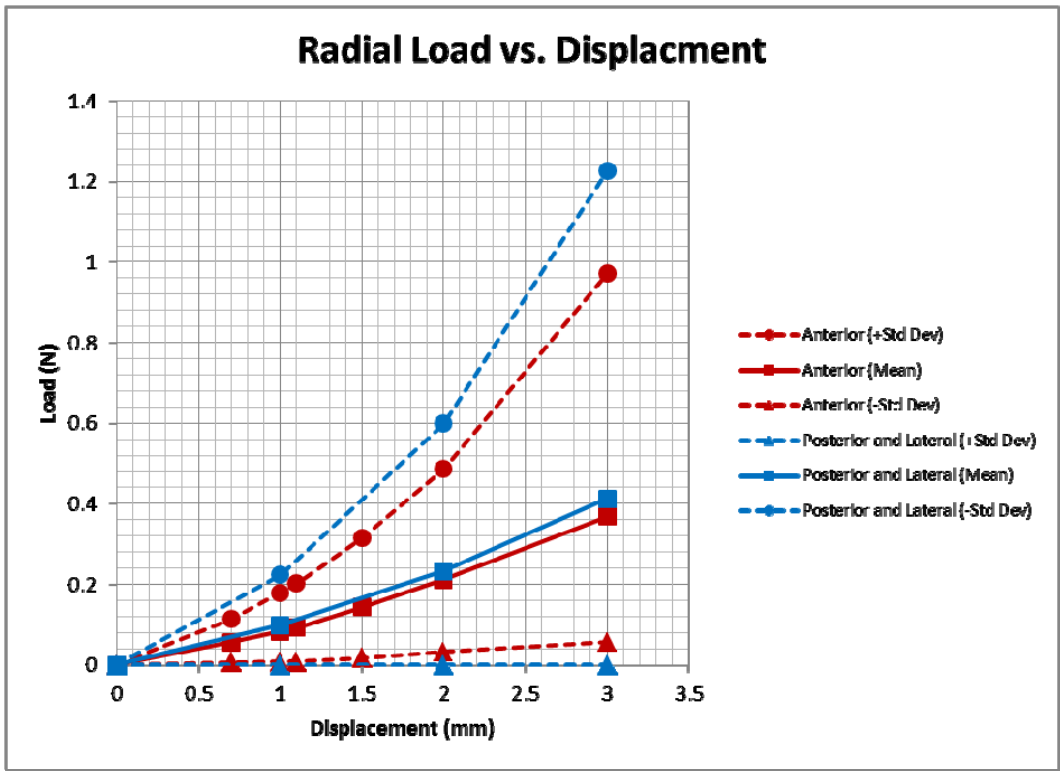

Figure 4.13. Combined force-displacement graph for radial loading, anterior and posterior quadrant, mean and +/-1 standard deviation

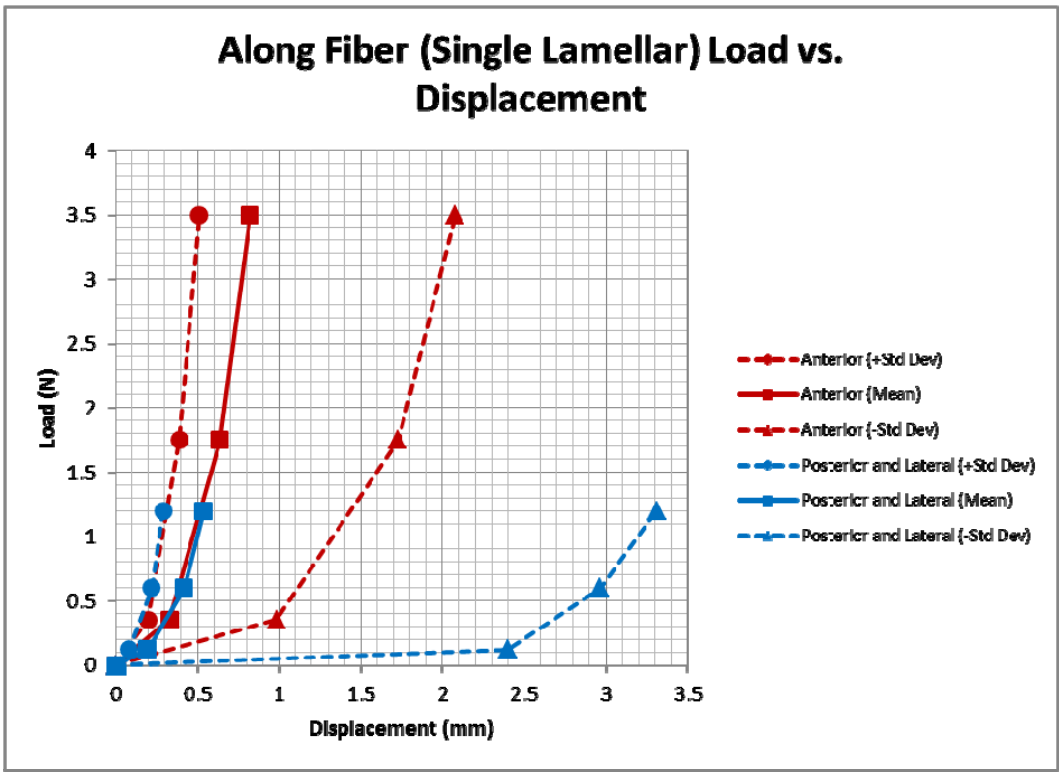

Figure 4.14. Combined force-displacement graph for single lamellar loading, anterior and posterior quadrant, mean and +/-1 standard deviation

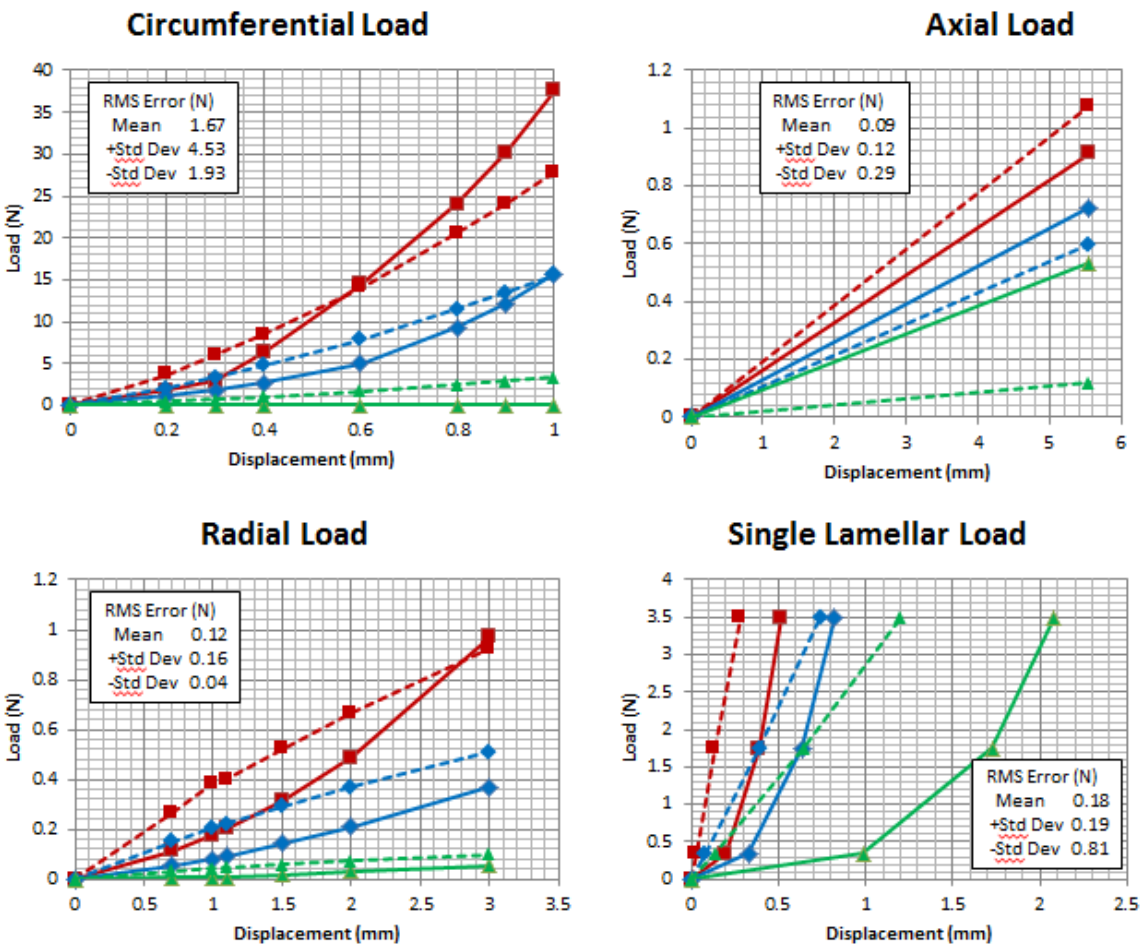

Figure 4.15. Monte Carlo results compared to combined literature curves, anterior quadrant

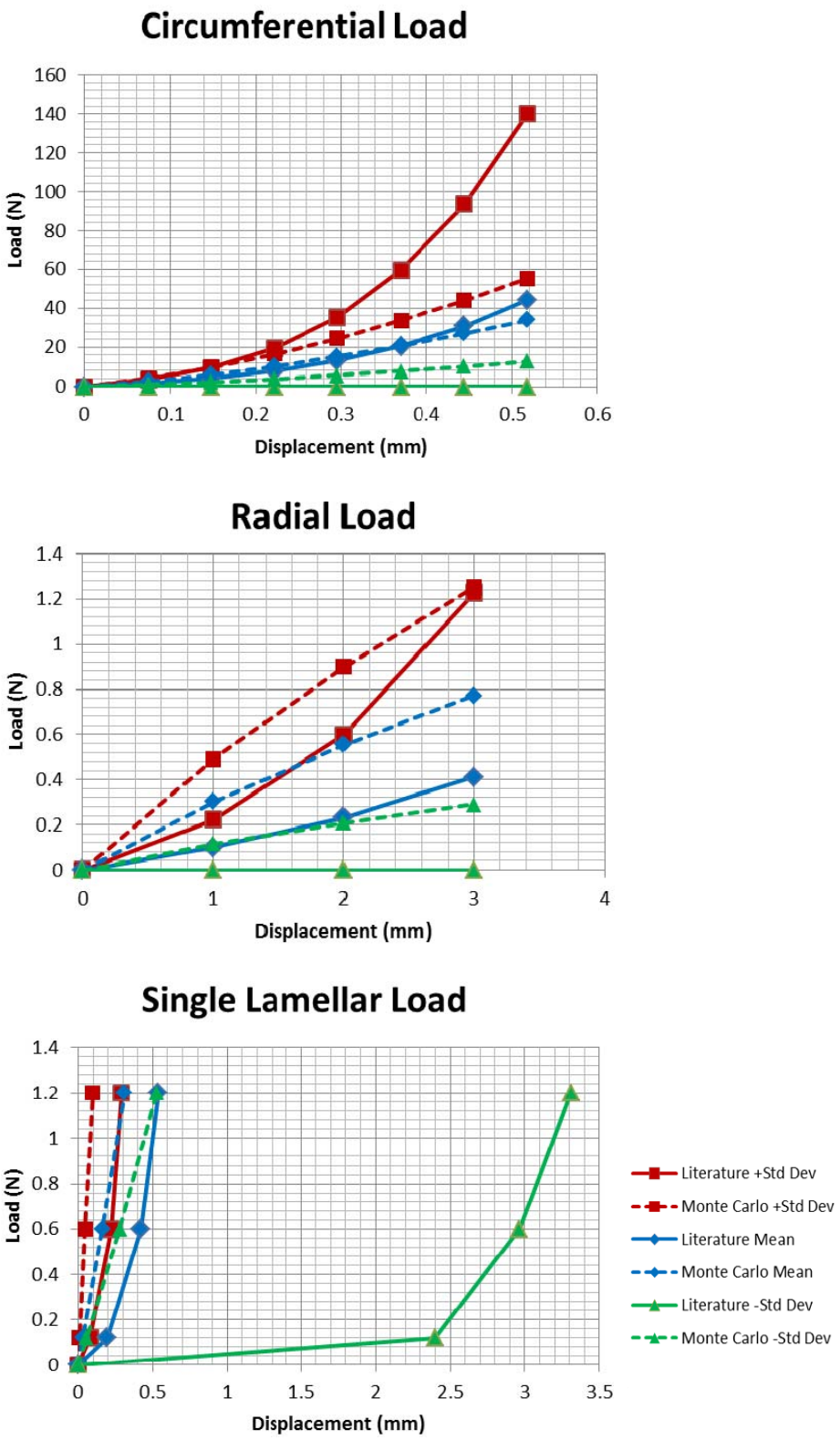

Figure 4.16. Monte Carlo results compared to combined literature curves, posterior quadrant

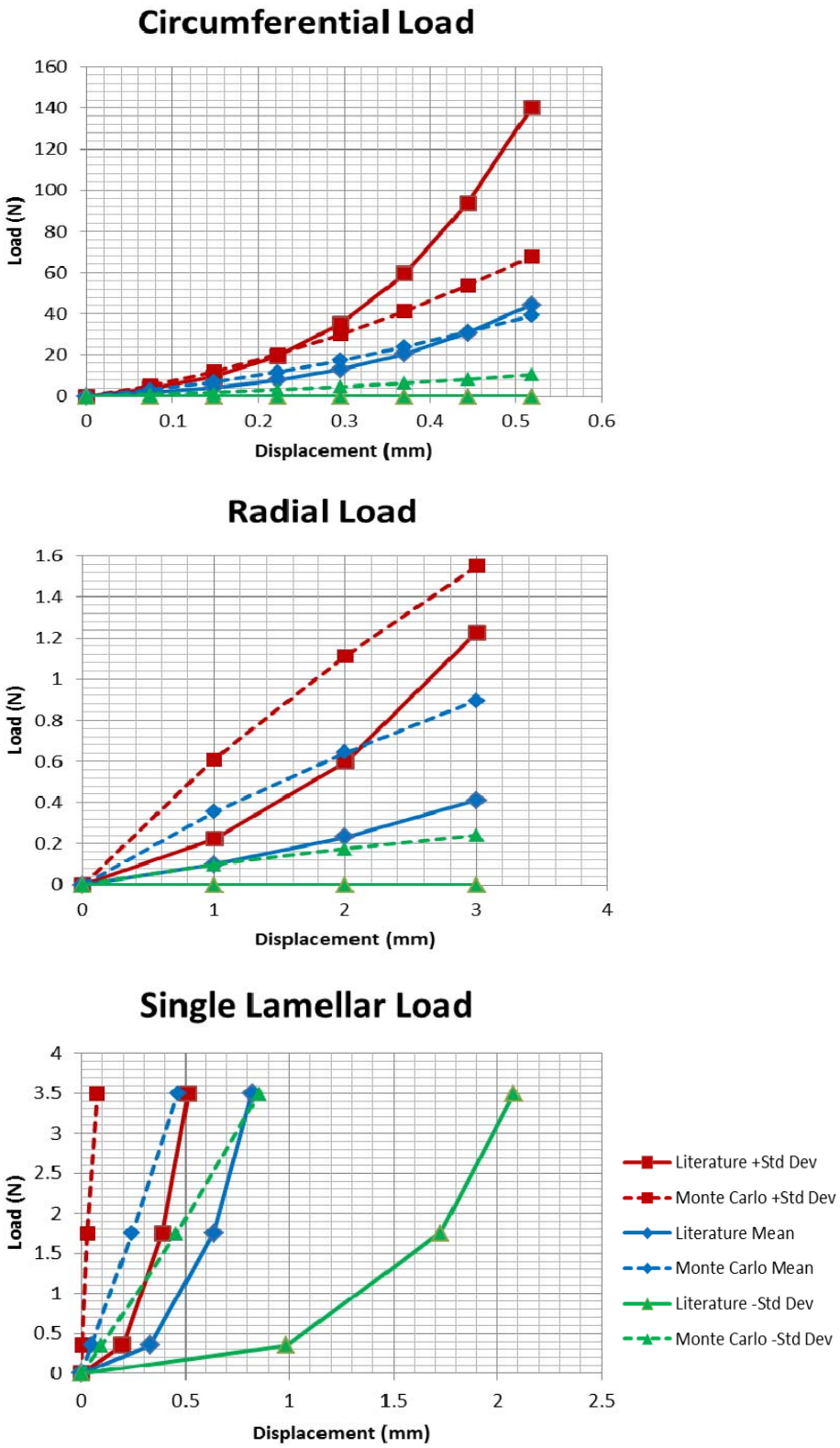

Figure 4.17. Monte Carlo results compared to combined literature curves, lateral quadrant

Table 4.1: ALL ligaments specimens tested by Neumann et al. 1992

Level	Ligament Length	Cross sectional Area	Donor and Age
T12-L1	77.0 mm	36.5 mm^2	21 years
L2-L3	76.0 mm	39.8 mm^2	
L4-L5	73.8 mm	43.5 mm^2	
L1-L2	78.4 mm	43.5 mm^2	29 years
T12-L1	73.0 mm	39.5 mm^2	43 years
L2-L3	83.0 mm	36.5 mm^2	

Table 4.2. Summary of annulus fibrosis data based on literature and location

Source	n	FSU Level	Loading				Location	AF Quadrant		
			Circ	Axial	Radial	Single Lamellar		Ant	Post	Lat
Guerin et al. [32]	8	L3-L4 L4-L5	✓				Anterior	✓		
Wagner et al. [33]	11	L2-L3 L3-L4 L4-L5	✓				Anterior	✓		
Fujita et al. [34]	8	L1-L2 L2-L3 L3-L4 L4-L5			✓		Anterior, Posterior-lateral	✓	✓	✓
Holzapfel et al. [35]	11	L1-L2				✓	Anterior-Lateral, Posterior	✓	✓	✓
O'Connell et al. [36]	7	L3-L4 L4-L5	✓	✓	✓		Anterior	✓		
Ebara et al. [37]	15	L3-L4	✓				Anterior, Posterior-lateral	✓	✓	✓

Table 4.3. Annulus fibrosis specimen sizes used for FE models

	Anterior	Posterior	Lateral
Circumferential	10.0x4.00x2.00 mm	3.70x4.40x2.30 mm	3.70x4.40x2.30 mm
Axial	11.1x2.30x1.50 mm	NA	NA
Radial	10.0x3.00x1.50 mm	10.0x3.00x1.50 mm	10.0x3.00x1.50 mm
Single Lamellar	15.0x5.00x0.700 mm	10.0x3.00x0.400 mm	15.0x5.00x0.700 mm

Table 4.4. Summarized ligament stiffness data based on literature

Ligament		Neumann et al., 1992	Pintar et al., 1992	Chazal et al., 1985	Iida et al., 2002	Robertson et al., 2013
ALL	Specimens	n=6 T12-L1 L1-L2 L2-L3 L4-L5	n=25 L4-L5	n=2 L4-L5		
	K mean	91.39 N/mm	40.50 N/mm	133.10 N/mm		
	K+Std Dev	114.8 N/mm	54.80 N/mm	185.90 N/mm		
	K-Std Dev	67.95 N/mm	26.20 N/mm	99.90 N/mm		
PLL	Specimens		n=25 L4-L5	n=2 L3-L4		
	K mean		25.80 N/mm	97.80 N/mm		
	K+Std Dev		41.60 N/mm	180.5 N/mm		
	K-Std Dev		10.00 N/mm	51.70 N/mm		
LFL	Specimens		n=22 L4-L5	n=1 L3-L4		
	K mean		19.30 N/mm	109.1 N/mm		
	K+Std Dev		28.00 N/mm	NA		
	K-Std Dev		10.70 N/mm	NA		
FCL	Specimens		n=24 L4-L5			
	K mean		30.6 N/mm			
	K+Std Dev		32.1 N/mm			
	K-Std Dev		29.1 N/mm			
ITL	Specimens			n=2 T7-T8 T9-10		
	K mean			35.35 N/mm		
	K+Std Dev			43.20 N/mm		
	K-Std Dev			28.80 N/mm		
ISL	Specimens		n=18 L4-L5	n=5 L4-L5	n=24 L4-L5	
	K mean		8.700 N/mm	38.10 N/mm	33.88 N/mm	
	K+Std Dev		15.20 N/mm	49.30 N/mm	54.40 N/mm	
	K-Std Dev		2.200 N/mm	26.70 N/mm	13.36 N/mm	
SSL	Specimens		n=18 L4-L5	n=5 L4-L5	n=24 L4-L5	n=3 L4-L5
	K mean		18.00 N/mm	38.10 N/mm	19.00 N/mm	19.20 N/mm
	K+Std Dev		24.90 N/mm	49.30 N/mm	30.50 N/mm	29.30 N/mm
	K-Std Dev		11.10 N/mm	26.70 N/mm	7.500 N/mm	9.100 N/mm

Table 4.5. Summary of combined ligament stiffness data

Stiffness	ALL	PLL	LFL	FCL	ITL	ISL	SSL
K mean (N/mm)	55.36	31.13	23.23	30.60	35.35	24.68	20.55
K Std Dev (N/mm)	17.87	20.33	8.67	1.50	7.20	15.75	9.97
Coefficient of variance	0.32	0.65	0.37	0.05	0.20	0.64	0.49

Table 4.6. Annulus fibrosis Holzapfel-Gasser-Ogden parameter values

	Anterior	Posterior	Lateral
C10 (Lognormal)	0.0670 ± 0.050 MPa	0.134 ± 0.100 MPa	0.130 ± 0.100 MPa
K1 (Normal)	1000.0 ± 500.0 MPa	2000.0 ± 1000.0 MPa	1500.0 ± 750.0 MPa
K2 (Normal)	4809.5 ± 2113.9	5296.3 ± 3208.7	5849.2 ± 3119.7

CHAPTER 5 – EFFICIENT PROBABILISTIC FINITE ELEMENT ANALYSIS OF THE LUMBAR SPINE

5.1 Background and Motivation

Finite element models of the lumbar spine are useful in assessing biomechanics and the performance of implants. Models are often developed based on geometry and experimental testing for an individual subject or specimen. The mechanical properties of the annulus and other soft tissue structures have significant variability among the population. Probabilistic methods can be used to assess the impact of soft tissue property variability on spine mechanics; however, they often require lengthy computation times. The objective of this study was to determine efficient variance reduction methods to perform Monte Carlo simulations of a Finite Element model of the L4 L5 functional spinal unit based on the variability of the soft tissue structures. Distributions for the soft tissue input parameters included the stiffness of spinal ligaments and parameters of a Holzapfel-Gasser-Ogden constitutive material model of the disc.

5.2 Introduction

Computational models of the human lumbar spine have been developed to evaluate spine biomechanics (Ayturk et al. 2011, de Visser et al. 2007, Eberlein et al. 2004, Ezquerro et al. 2004, Ezquerro et al. 2011, Guan et al. 2006, Lu et al. 1996,

Schmidt et al. 2007, Wong et al. 2003) and spinal implant performance (Bono et al. 2007, Bowden et al. 2008, Chiang et al. 2006, Dooris et al. 2001, Goel et al. 2005, Polikeit et al. 2003, Rohlmann et al. 2005, Tsuang et al. 2009, Vadapalli et al. 2006, Xiao et al. 2012, Zhong et al. 2009). The biomechanics measures are typically torque-rotation response, facet contact force, disc pressure, and annulus fibrosis (AF) strain. Most of these studies have used deterministic models with patient-specific anatomy generated from medical image data. In some cases, the soft tissue representation is based on the same patient-specific tissue tests, but in most cases the ligaments are defined from other data found in literature using the average values in literature.

A probabilistic approach provides an understanding of the variability in spine biomechanics and implant performance based on input variability. Previous studies have used the Monte Carlo method (MC), to capture the variability in the spinal biomechanics based on the variability of the soft tissue properties (Lee and Teo, 2005) and the combination of soft tissue and anatomic geometry (Barnes et al. 2011). Work has also been done on modeling the failure of a vertebral body based on the variability of stress measures in the bone (Ahman et al. 2010, Rohlmann et al. 2010). In addition, probabilistic studies have been performed by varying total disc replacement (TDR) locations in the disc space and key geometric features of the TDR (Rohlmann et al. 2009). The approach represents all of the input parameters as distributions and predicts output distributions and bounds of performance while also identifying the sensitivity factors indicating which input parameters, or combination of parameters, were most influential. This study used a comprehensive summary of literature, which focused on

direct mechanical test data, to define the variability in the AF tissue and the spinal ligaments (Coombs et al. 2015).

As the traditional MC method uses a random sampling technique, it typically requires 100s to 1000s of trials and is thereby computationally expensive. Other variance reduction sampling techniques, like the Descriptive Sampling (Isight Component Guide, Saliby 1990) and Sobol Sampling (Burhenne, et al., 2011, Isight Component Guide) can predict the same distributions for the output parameters in less iteration. Although efficient probabilistic methods have been applied to the cervical spine (Thacker et al. 2001), this has not been done for the lumbar spine with a robust definition of input variability.

Accordingly, the objectives of this study were to determine if the descriptive sampling or Sobol sampling techniques would efficiently predict the same distribution of output torque-rotation curves as the random sampling technique using an FE model of a L4-L5 functional spinal unit (FSU). This was determined by comparing the differences and determining which method is most efficient with the least number of Monte Carlo iterations. The probabilistic framework enabled the prediction of the distribution and bounds of torque rotation curves based on flexion, extension, axial rotation, and lateral bending.

5.3 Methods

An Abaqus (Simulia, Dassault Systemes, Johnston, RI) Finite Element (FE) model was used (Fig. 5.1), which was based on a healthy L4-L5 FSU from a 33 year old male subject, with none to mild disc degeneration (Rao 2012, Coombs et al. 2013). The

vertebral geometry was segmented using ScanIP (Simpleware, Exeter, UK) and bones were considered rigid and represented by 3-noded triangular rigid elements (Element type=R3D3). The disc geometry was defined by transversely sectioning the disc and measuring the perimeter and the transition between the AF and the nucleus pulposis (NP). The AF was meshed with 8-noded hexahedral elements (Element type=C3D8R) and the NP was represented with an 8 noded fluid-filled membrane (Element type= SFM3D4R). The AF was modeled using the Holzapfel-Gasser-Ogden (Holzapfel et al., 2000) anisotropic, hyperelastic constitutive model. This constitutive model was chosen because the embedded fibers are mathematically represented, which allows the stiffness, fiber direction, and fiber dispersion to be modified with parameters. The AF was divided into four quadrants representing an anterior quadrant, posterior quadrant, and right and left lateral quadrants due to the variation in material properties in the AF (Kurtz et al. 2006). The orientation of the elements in the AF was defined using the normal direction of the outer surface of the disc for the radial direction, the interior / superior direction, and the remaining tangential direction was derived. The articulating facet surfaces were considered rigid and represented by 8-noded hexahedral elements (Element type=C3D8R) to improve computational efficiency (Rao et al. 2009). Seven passive ligaments were defined in the model using non-linear tension only connector elements. The ligaments included the anterior longitudinal ligament (ALL), posterior longitudinal ligament (PLL), supraspinous ligament (SSL), intraspinous ligament (ISL), intertransverse ligament (ITL), facet capsular ligament (FCL) and ligamentum flavum (LFL). Most of the ligament attachment sites were based on dissection performed after testing and from literature based descriptions (Panjabi et al., 1991). The ALL and PLL

were defined with 26 rows of connectors in parallel with each row containing 7 connectors in series. The LFL was defined with 3 connectors in parallel, the FCL was defined with 4 in connectors in parallel on the left and right side, the ITL was defined with 2 connectors in parallel, the ISL was defined with 5 connectors in parallel, and the SSL was defined with 1 connector.

The model was driven by rotations of 5.92° in extension, 8.66° in flexion, 6.01° in lateral bending, and 1.75° in axial rotation. This was the resulting rotation from 10Nm applied in previous testing used to develop the FE model (Rao 2012, Coombs et al., 2013). The reaction moment was a measured output from the model.

5.3.1 Ligaments

Each ligament stiffness was represented as distributions from a comprehensive summary of literature, which focused on direct mechanical test data, to represent the distribution of stiffness in the spinal ligaments (Coombs et al. 2015). The focus of this summary was on the L4 L5 level of the human lumbar spine. In some cases, other levels were used if the L4 L5 was not available. For convenience, a single stiffness parameter was defined for the stiffness of the linear load displacement behavior for each ligament. Two inflection points were defined to represent the toe in region and the location of the points was defined as a function of the stiffness parameter. Table 5.1 summarizes the mean and standard deviation of the stiffness parameters for all seven ligaments used as inputs in this probabilistic study.

5.3.2 Annulus Fibrosis

The test data of the AF was grouped into four quadrants; anterior, posterior, and left and right lateral. The left and right lateral quadrants were assumed to be identical. Again, a comprehensive summary of literature was used, which focused on direct mechanical test data to define the variability in the AF (Coombs et al. 2015) for healthy subjects. Probabilistic analyses were performed to determine the distribution of parameters for the Holzapfel-Gasser-Ogden anisotropic, hyperelastic constitutive model (Holzapfel et al., 2000) to match the distribution found in the literature summary. The model is defined by five parameters (C10, D, K1, K2, κ). C10 represents the stiffness of the ground substance. K1 represents the stiffness of the fibers in the material. K2 determines the nonlinearity of the fiber stiffness. The compressibility parameter, D, was defined as 1/(20*C10), which is equivalent to defining the initial bulk modulus as twenty times the initial shear modulus. This is similar to a Poisson's Ratio of 0.475 or nearly incompressible (Abaqus Users Guide Chapter 22.5.1, release 6.12). The fiber dispersion parameter, κ, was set to 0 assuming the fibers are perfectly aligned to the fiber direction. Therefore, there were three input parameters used for each quadrant. The resulting mean and standard deviation for the Holzapfel-Gasser-Ogden parameters, for each quadrant, is summarized in Table 5.1. Note that the C10 parameter is defined as a lognormal distribution.

5.3.3 Probabilistic Methods

Monte Carlo simulation methods were implemented in Isight (Simulia, Dessault Systemes, Johnston, RI) to determine the uncertainty of the torque-rotation curves for

flexion, extension, axial rotation, and lateral bending based on the uncertainty of the soft tissue parameters (Fig. 5.2).

The first variance reduction technique used was Descriptive Sampling (Saliby 1990). The Descriptive Sampling technique is similar to the Latin Hypercube technique in that the space defined by each random input parameter is divided into subsets of equal probability and the analysis is performed with each subset of each random parameter only once.

The second variance technique used was Sobol Sampling (Burhenne et al., 2011). The Sobol technique uses a quasi-random sequence to generate samples of input parameters more uniformly than random and descriptive sampling while considering previously sampled points to avoid clusters and gaps. The Sobol sequence generates numbers as binary fractions of appropriate length from a set of special binary fractions.

The random sampling technique was done for 500 iterations and error and convergence was calculated to determine the quality of results. The Descriptive Sampling and Sobol Sampling techniques were used with 50 and 25 iterations and compared to the random sampling technique. The comparisons were based on the 10th percentile and 90th percentile torque rotation curves. Presenting a comparison at these bounds describes the variability in a way that is useful for the audience and shows a comparison at the tails of the distribution. It is also more challenging to compare the data at the tails of the distribution rather than using +/- 1 standard deviation. The choice of 10th and 90th percentile is arbitrary, but is a common approach to presenting and comparing probabilistic data. The 5th and 95th percentile or 1st and 99th percentile could also be presented depending on the application.

5.3.4 Sensitivity Analysis

A sensitivity study was also performed to determine which input parameters affected the reaction torque most. This was done using the Parameter Study in Isight, which independently modifies each parameter at 3 intervals. In addition, a correlation study was done with the 500 random sampling data points using the Pearson Product-Moment Correlation Coefficient for two sets of values. The 500 data points were also used to determine important non-linear relationships between the input parameter and the reaction torques.

5.4 Results

5.4.1 Probabilistic Methods

The Monte Carlo simulation was performed using a random sampling technique and 500 iterations. Each iteration required about 70 minutes, which ran two FE models in parallel on one core each based on the available software licenses. Therefore, 500 iterations took about 24 days which shows the need to evaluate variance reduction techniques. The uncertainty was calculated for the 10th and 90th percentile torque rotation graphs based on 500 iterations (Haldar et al., 2000). The uncertainty at the end of the applied rotation is summarized in Table 5.3.

Convergence error was evaluated by calculating the cumulative 10th and 90th percentile of the reaction moment at the end of the applied rotation and then calculating the percent error between the current iteration cumulative percentile and the previous iteration. The convergence error for flexion, extension, axial rotation, and lateral bending

was less than 0.5% at 500 iterations (Fig. 5.3). Knowing these quality measures, this was used as a baseline to compare the variance reduction sampling techniques.

The descriptive sampling and Sobol sampling techniques were run with 25 and 50 iterations. The torque rotation curves at the 10th and 90th percentile were compared to the random sampling technique. This was done for the flexion, extension, axial rotation, and lateral bend motions for each sampling technique and the curves based on mean input parameter values were included in the graphs (Fig. 5.4 through 5.6). The sum of the squared error for each time point of the torque rotations were calculated relative to the random sampling technique with 500 iterations for all bending motions (Table 5.4 and Fig. 5.7). When combining the 10^{th} and 90^{th} percentile squared error for flexion-extension, the descriptive sampling technique performed best at 50 iterations with a total error of 4.383 Nm^2. When combining the 10^{th} and 90^{th} percentile squared error for axial rotation, the descriptive sampling technique performed best at 25 iterations with a total error of 11.526 Nm^2 and the Sobol sampling technique performed best at 50 iterations for lateral bending. However, when combining the 10^{th} and 90^{th} percentile squared error for axial rotation and lateral bending, the best sampling technique was the descriptive sampling technique at 50 iterations with a total error of 21.876 Nm^2.

The % change in angular rotation was also determined between the random sampling technique and the descriptive sampling technique with 50 iterations at relevant torque levels. There was less than a 3% difference in rotation for flexion at 10Nm at the 10^{th} and 90^{th} percentile. There was less than a 2% difference in rotation for extension at 3Nm at the 10^{th} and 10Nm at the 90^{th} percentile. There was a 10.4% difference in rotation for axial rotation at 3.5Nm at the 10^{th} and less than 1% at 10Nm at the 90^{th}

percentile. Finally, there was less than a 5% difference in rotation for lateral bending at 7Nm at the 10^{th} and 10Nm at the 90^{th} percentile.

5.4.2 Sensitivity Study

The sensitivity results generally made sense based on the location of the soft tissue structures and the flexion, extension, axial rotation, and lateral bending (Fig. 5.8a). For example, during flexion the stiffness of the SSL and ISL had the greatest impact on sensitivity. During extension, the stiffness of the ALL and the C10 parameter of the anterior disc quadrant was significant. During lateral bending, the stiffness of the ITL and C10 parameter of the lateral disc quadrant were significant. However, the fiber angle parameter had the greatest impact on sensitivity for the extension, axial rotation, and lateral bending motions. This was unexpected, so the 500 data points from the random sampling technique was used to do a correlation study and also look at the relationship of fiber angle to the reaction torque for each motion. They generally match the parameter study (Fig. 5.8b). The reaction moments as a function of fiber angle for each motion was determined (Fig. 5.9 and 5.10). Although the data is cloudy since the other parameters were varying, a similar trend is obvious for extension and axial rotation. The trend appears to be an exponential increase in reaction moment as fiber angle increases so fiber angle has a greater impact on sensitivity as the value increases. The graph for lateral bending shows an increase in reaction moment, but the relationship is not as obvious and the graph for flexion appears to simply be a cloud of data with no clear relationship.

5.5 Discussion

The objectives of this study were to determine if the descriptive or Sobol sampling techniques would efficiently predict the same distribution of output torque-rotation curves as the random sampling technique using a Monte Carlo simulation of a L4-L5 FSU FE model. This study focused on the variability in torque rotation due to the variability in the soft tissue representation, which was statistically defined from literature based on direct mechanical test measurements. Soft tissue variability is useful because it can be used in subject specific models with upper and lower bounds to evaluate biomechanics and implant performance. Additional output measures could be considered such as disc pressure, facet contact forces, and annulus strain.

One limitation is that the AF properties were based on a healthy normal population. Further work could be done to also characterize properties of degenerated discs and their variation, which may be useful when developing spinal implants. Work has been done showing that the range of motion generally decreases with increasing degeneration use FE models with correlation to biomechanical testing (Rohlmann et al. 2006).

Another limitation is that this study assumed that the boney anatomy was rigid but the kinematic output of this model should not be sensitive to the stiffness of the vertebral bodies. This has been show in cervical spine sensitivity studies (Thacker et al. 2001). Although the variability of soft tissue was considered, a future study could build on this work by including variability in the bony anatomy and facet cartilage geometry. For example, statistical shape models based on a set of radiographic data could be used to

define the geometry of the vertebrae. Change in anatomy such as height and body weight could also change the loading conditions.

Since the boney anatomy was based on a single subject (33 years, male, 59 kg), this anatomy was compared to statistical measurements from 157 healthy spines with a mean age of 26.8 years (Gilad et al. 1986). Table 5.2 summarizes the comparison of the FE model measurements to the literature using the L4-L5 data. The anterior / posterior (A/P) width of the endplates is less than 1 standard deviation of the literature values with the exception of the superior L5 end plate, which is still less than the mean. The anterior and posterior FE model disc height is greater than the mean disc height. Therefore, the disc in the FE model is taller and narrower than the literature means. This would make the disc more flexible in flexion and extension, which could explain why the model is less stiff with mean parameter values than the typical torque rotation curves. Furthermore, the height of the donor used to define the FE model was 177.8cm tall compared to the mean height of 174.7cm from Gilad et al. 1986.

To further compare the FE model to literature, the Monte Carlo simulation data was compared to ranges of motion measured in the literature. Guan et al. 2006 statistically reported torque rotation curves for 10 L4-L5 FSU's (50.6 +/- 13.2 years old, max 68, min 27) loaded with a pure moment in flexion, extension, lateral bending and axial rotation. Campbell et al. 2011 reported similar data with 9 L4-L5 FSU's (mean 65.5 years old, max 75, min 48). Qualitatively, the mean data falls between the experimental ranges of +/- 1 standard deviation for all degrees of freedom with the exception of extension (Fig. 5.11 through 5.13). For lateral bending and axial rotation the model was only run in one direction and symmetric behavior was assumed. The spread

between the +/- 1 standard deviations torque rotation curves, based on the Monte Carlo data, were generally less than the literature curves. However, this may be because the Monte Carlo simulation in this study only includes soft tissue variability and does not include boney anatomy variability. Another way to compare the model to literature was to use the total range of motion at a given moment. Campbell et al. 2011 also statistically reported range of motion at 10Nm for flexion, extension, lateral bending, and axial rotation. Yamamoto et al. 1989 reported similar data based on 10 L4-L5 FSU's (25 to 63 years). Panjabi et al. 1994 reported range of motion at 4Nm for flexion, extension, and lateral bending based on 9 FSU's (35 to 62 years) and Guan et al. 2006 reported similar data based on 10 L4-L5 FSU's (mean 50.6 +/- 13.2 years). The FE data was within 1 standard deviation for one literature source except for flexion-extension at 10Nm (Fig. 5.14). Although the flexion-extension range of motion was not within 1 standard deviation of a single literature source, it was between the means of two literature sources. The standard deviation for total range of motion based on the Monte Carlo data was greater than the literature for the flexion-extension data. However, it was less for lateral bending and axial rotation. Again, this could be due to not including the variation on the boney anatomy. The variability in facet orientation and location would most likely increase the variability in the axial rotation data. There was not a literature source to compare axial rotation at 4Nm.

A Monte Carlo simulation was performed using a random sampling technique with 500 iterations. This required about 24 days. However, descriptive sampling and Sobol sampling techniques were used to reduce the time required to run a Monte Carlo simulation. It has been shown that the descriptive sampling technique with 50 iterations

was the best overall match to 500 iterations using the random sampling technique based on the sum of squared error. 50 iterations would only require 2 ½ days or about a 90% reduction in computation time.

A sensitivity analysis was also performed. As expected, the reaction moment was generally most sensitive to ligaments that had the greatest moment arms in line with the direction of motion. This is also true with the quadrants of the disc. Surprisingly, the reaction moment was most sensitive to the AF fiber angle for extension and axial rotation. The fiber angle parameter had the greatest impact on sensitivity for each applied rotation. This was unexpected and there appeared to be an exponential increase in reaction moment as fiber angle increases so fiber angle has a greater impact on sensitivity as the value increases. This could be further studied through cadaveric biomechanical studies to better understand the relationship between AF fiber angle and the torque rotation response. This should also be measured when creating subject specific FE models.

Using variance reduction sampling methods enables probabilistic analyses to be done in a more feasible amount of time. Monte Carlo simulations of intact and instrumented spine models can be done in 10% of the time required for a traditional random sampling technique. This could allow spinal implant designs to be efficiently evaluated over a population based on measures related to the implants. Examples include stress or strain in the implant, kinematic evaluation for motion preserving implants, and positioning of the implant in the spinal anatomy.

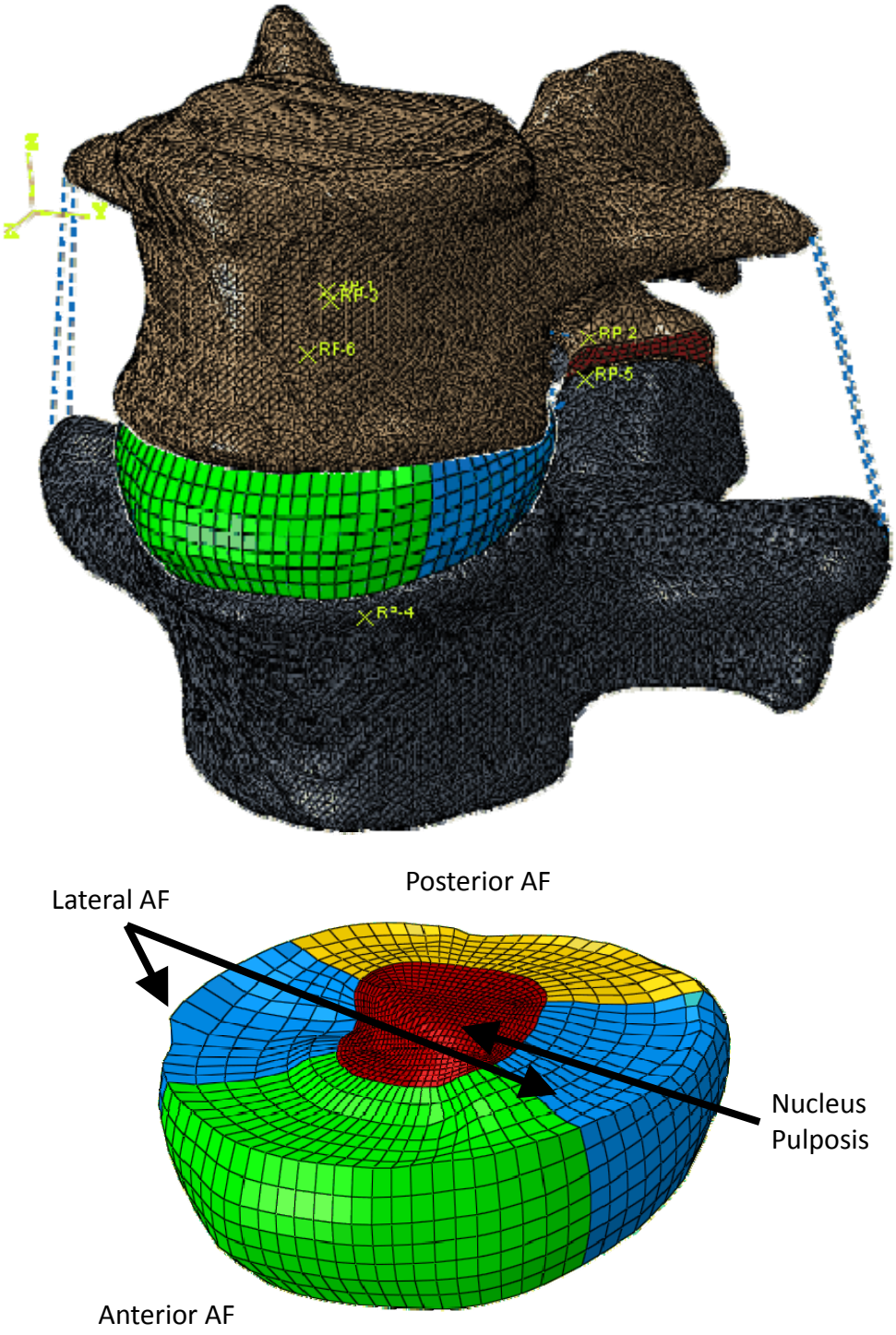

Figure 5.1. Finite element model of L4-L5 FSU model

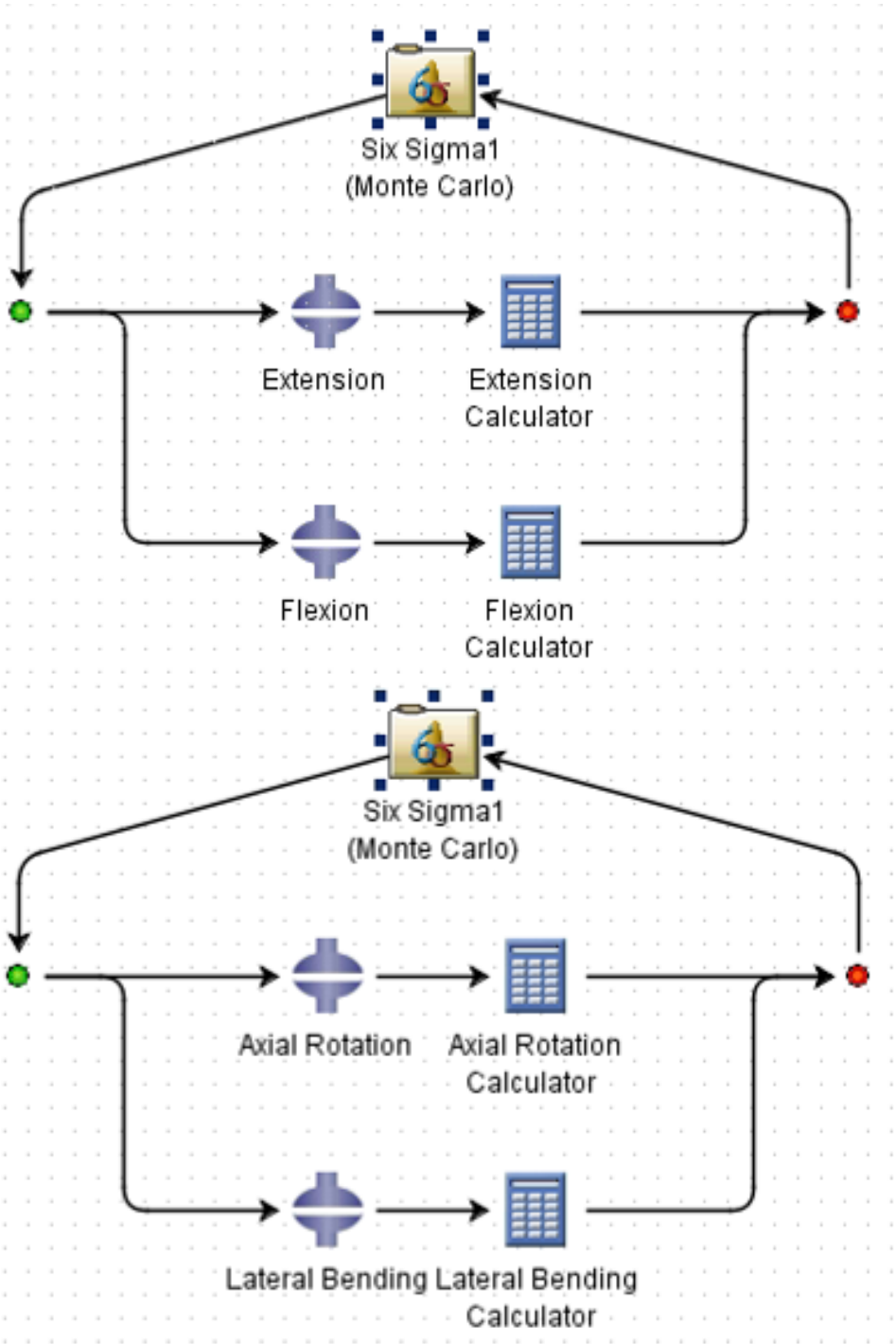

Figure 5.2. Isight workflows, Monte Carlo simulations for flexion and extension, and for axial rotation and lateral bending

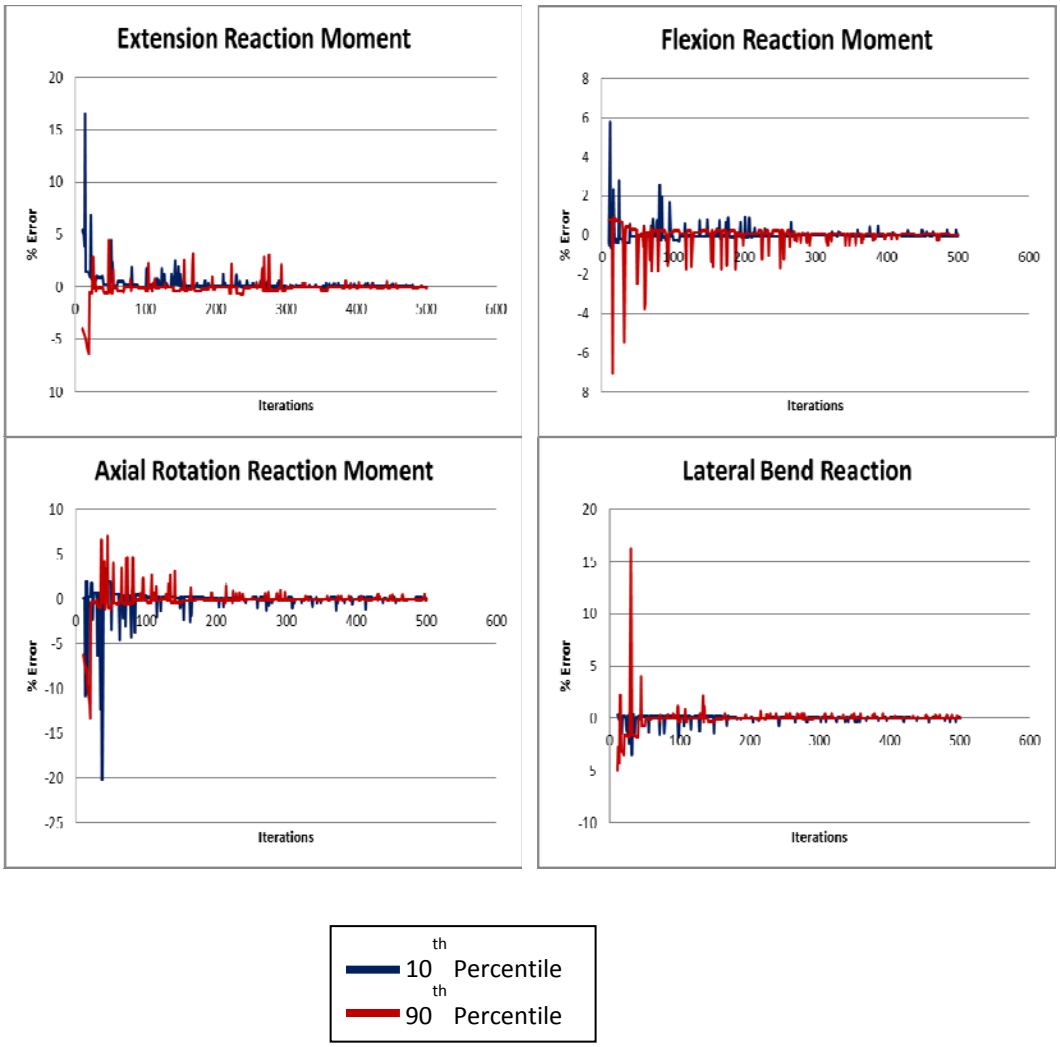

Figure 5.3. Monte Carlo %error convergence, 500 iterations with simple random sampling

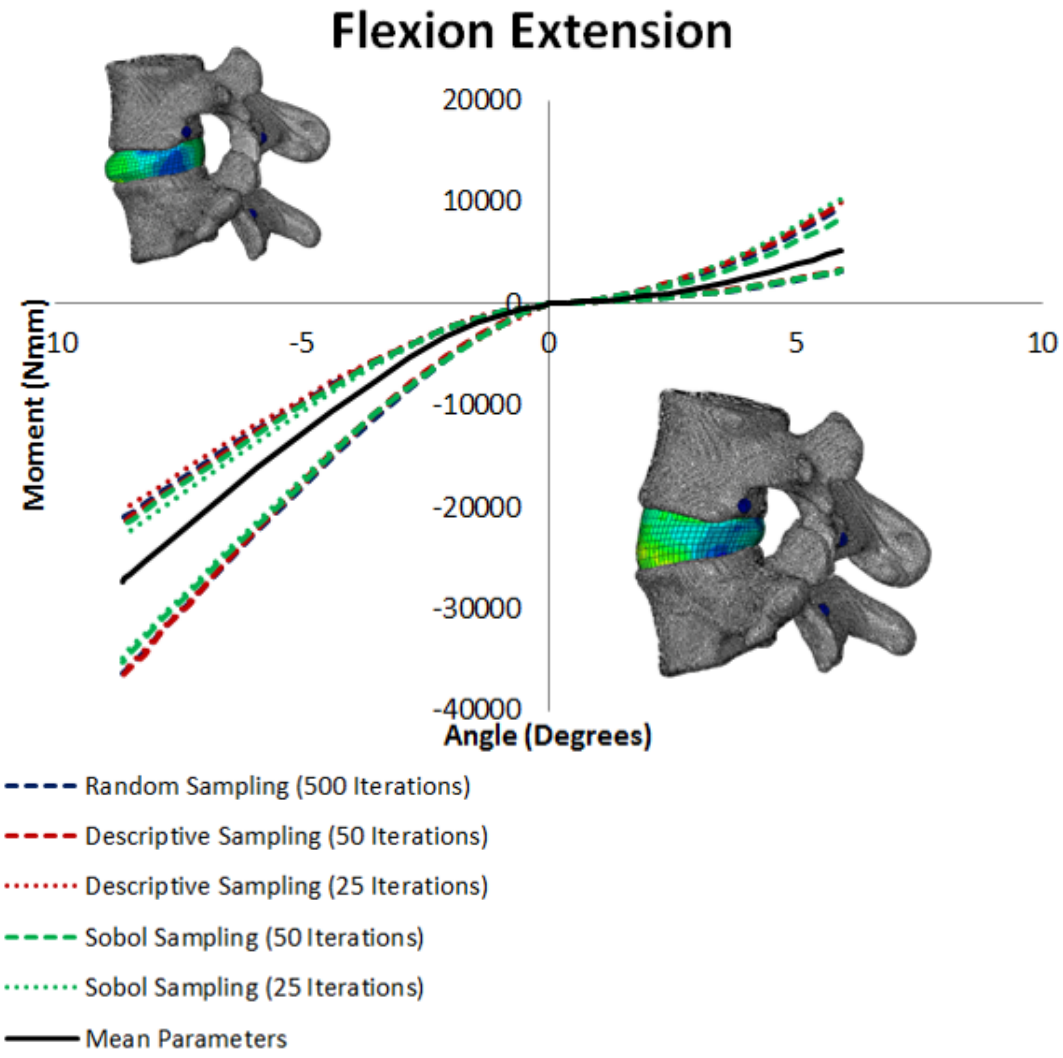

Figure 5.4. Torque rotation comparisons for flexion and extension, Monte Carlo results at 10^{th} and 90^{th} percentile

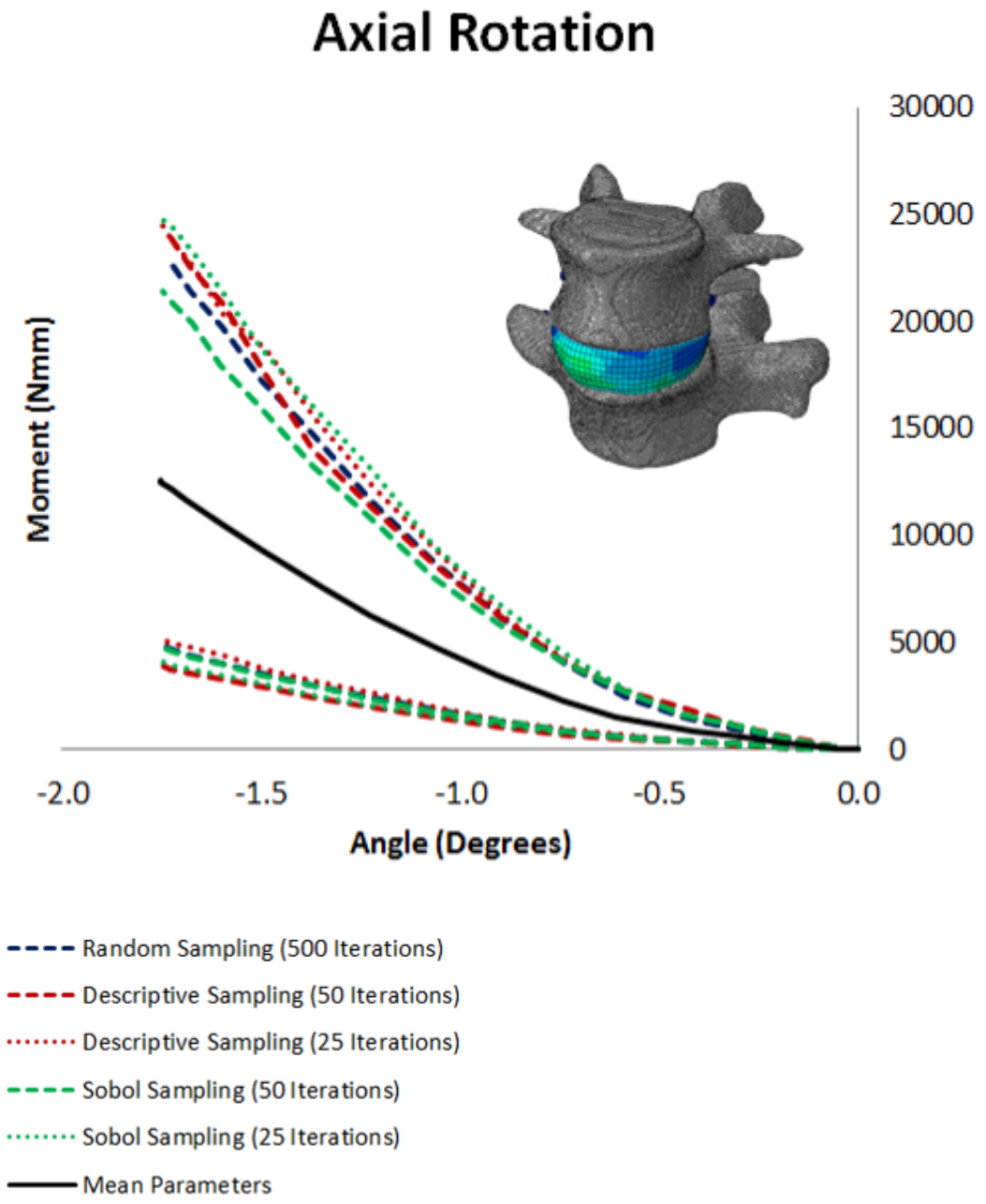

Figure 5.5. Torque rotation comparisons for axial rotation, Monte Carlo results at 10th and 90th percentile

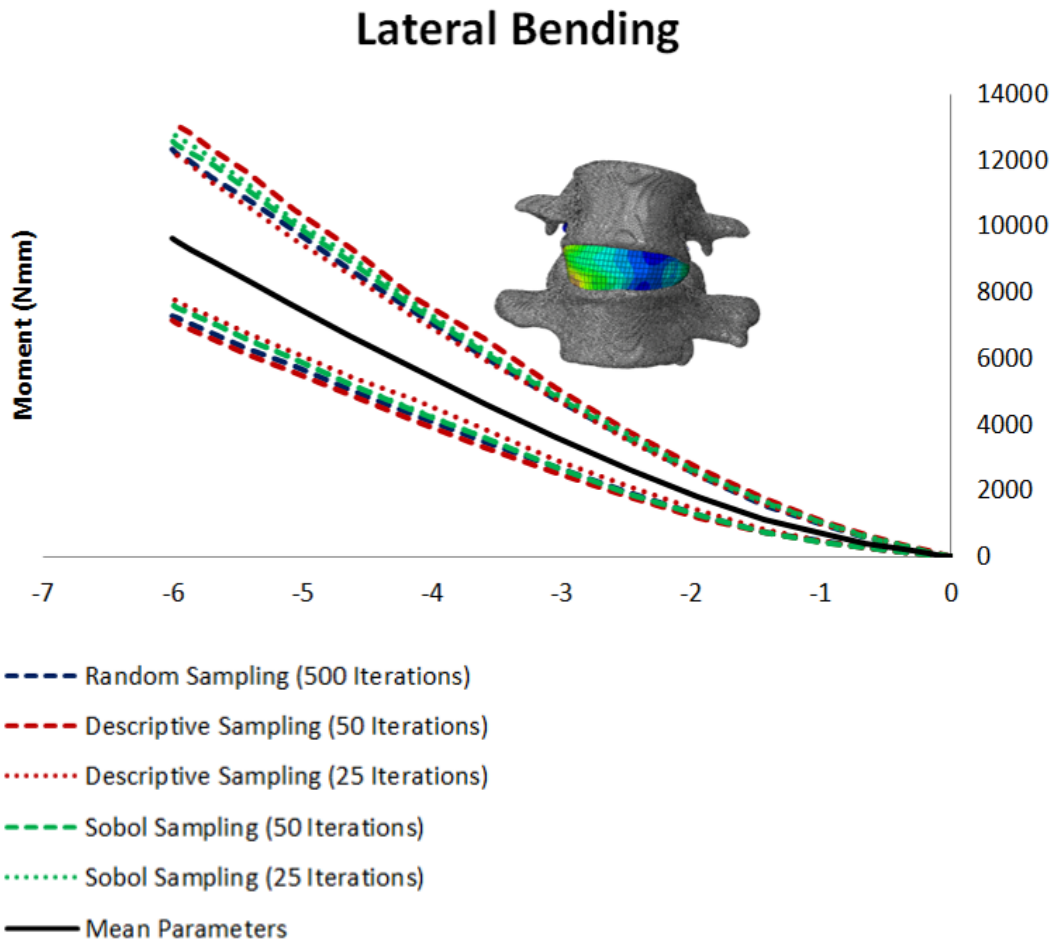

Figure 5.6. Torque rotation comparisons for lateral bending, Monte Carlo results at 10th and 90th percentile

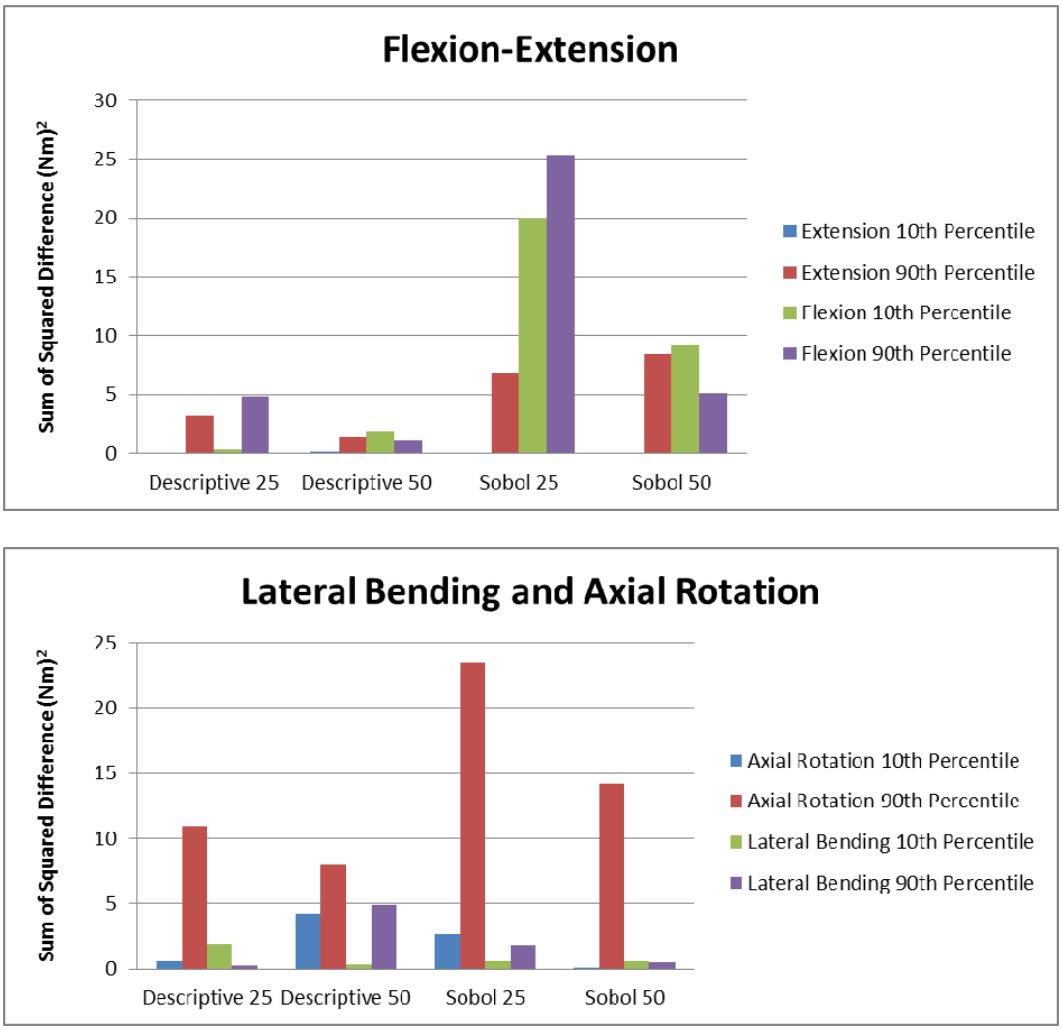

Figure 5.7. Sum of squared difference, descriptive sampling and Sobol sampling compared to simple random sampling for (a) flexion and extension; (b) lateral bending and axial rotation

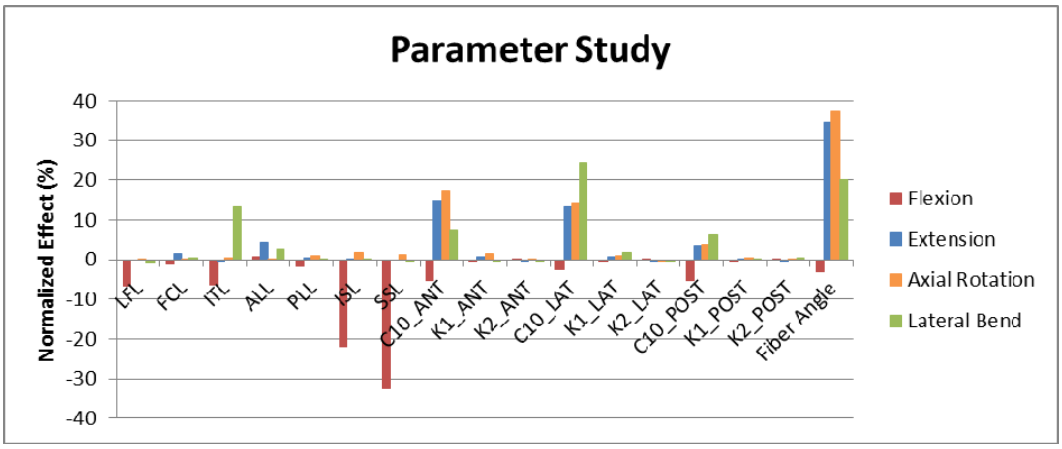

(a)

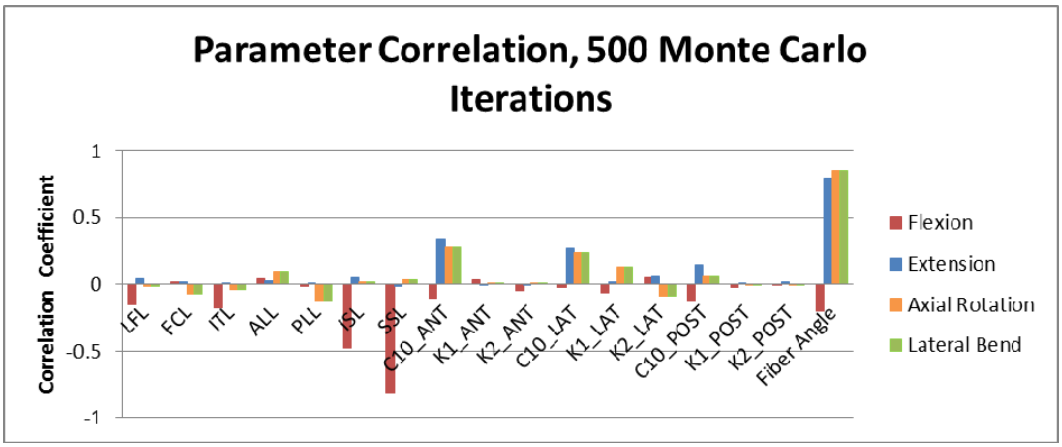

(b)

Figure 5.8. Parameter sensitivity (a) parameter study in Isight; (b) parameter correlation based on Monte Carlo simulation data

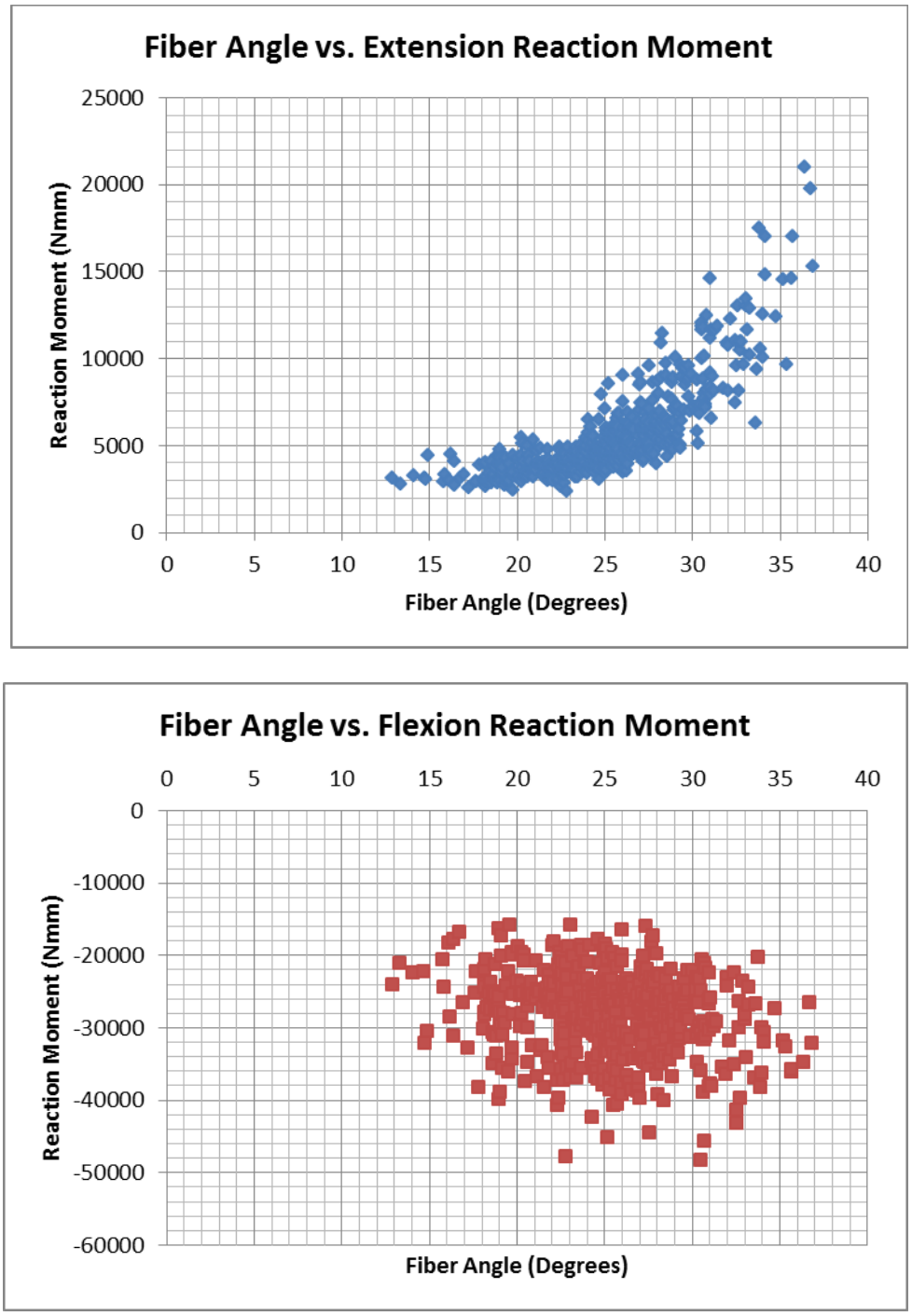

Figure 5.9. Fiber angle vs. reaction moments for flexion and extension, 500 Monte Carlo iterations

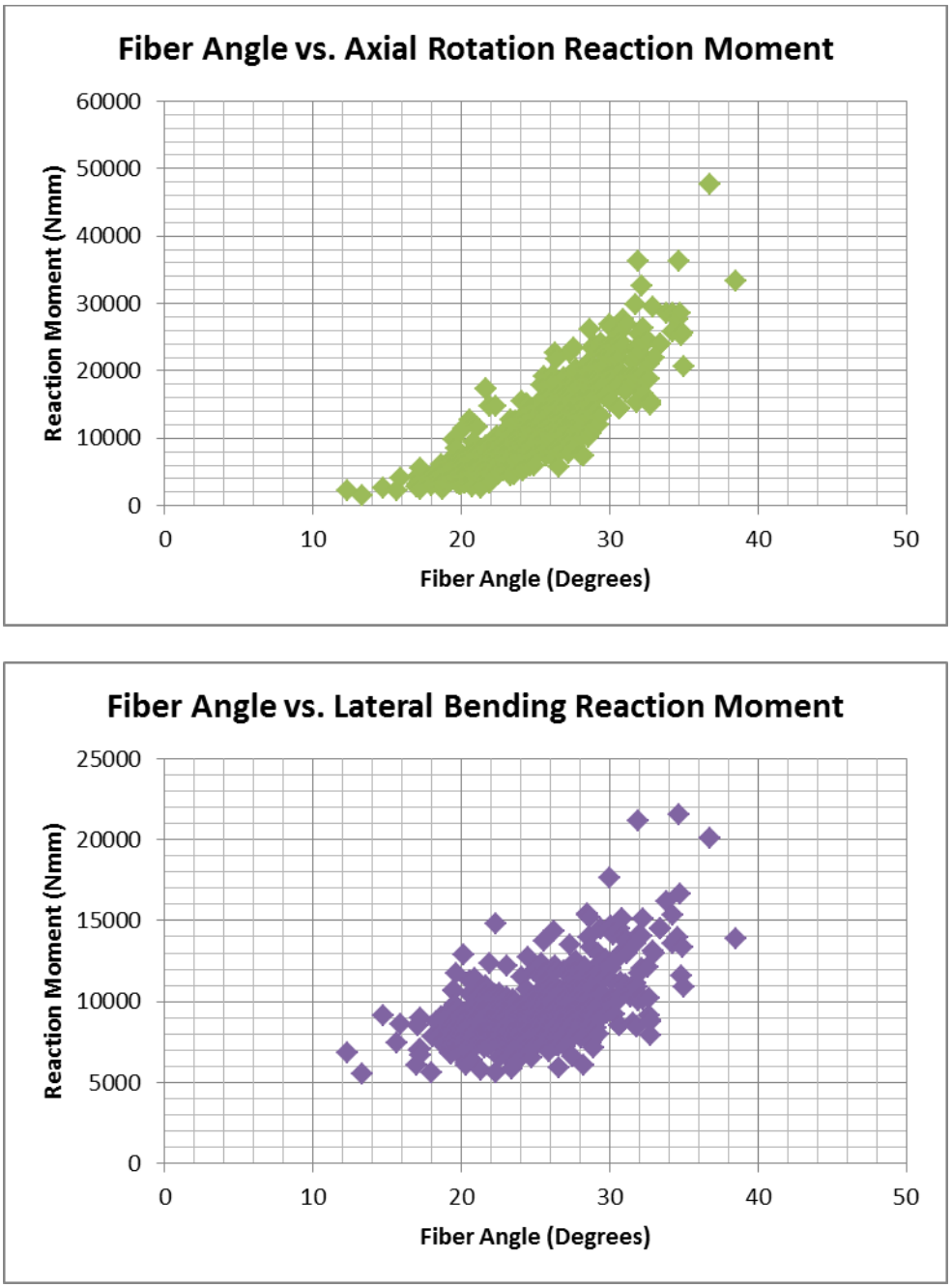

Figure 5.10. Fiber angle vs. reaction moments for axial rotation and lateral bending, 500 Monte Carlo iterations

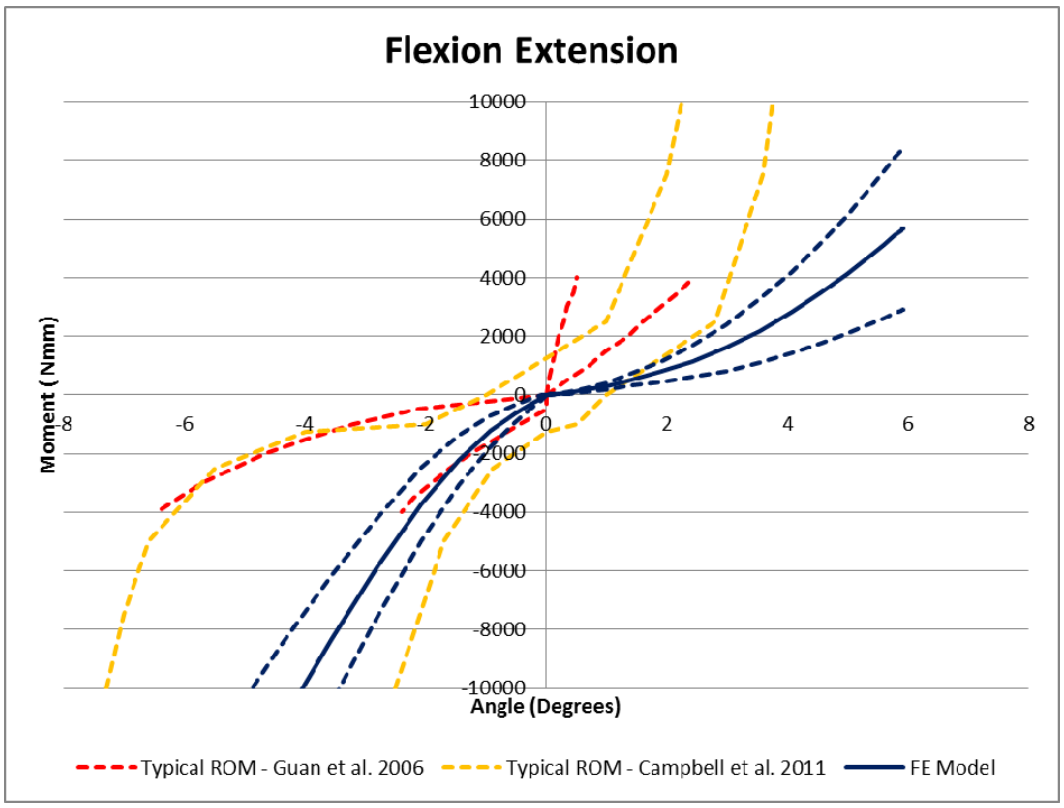

Figure 5.11. Mean torque rotation curves compared to range of curves from literature, flexion and extension

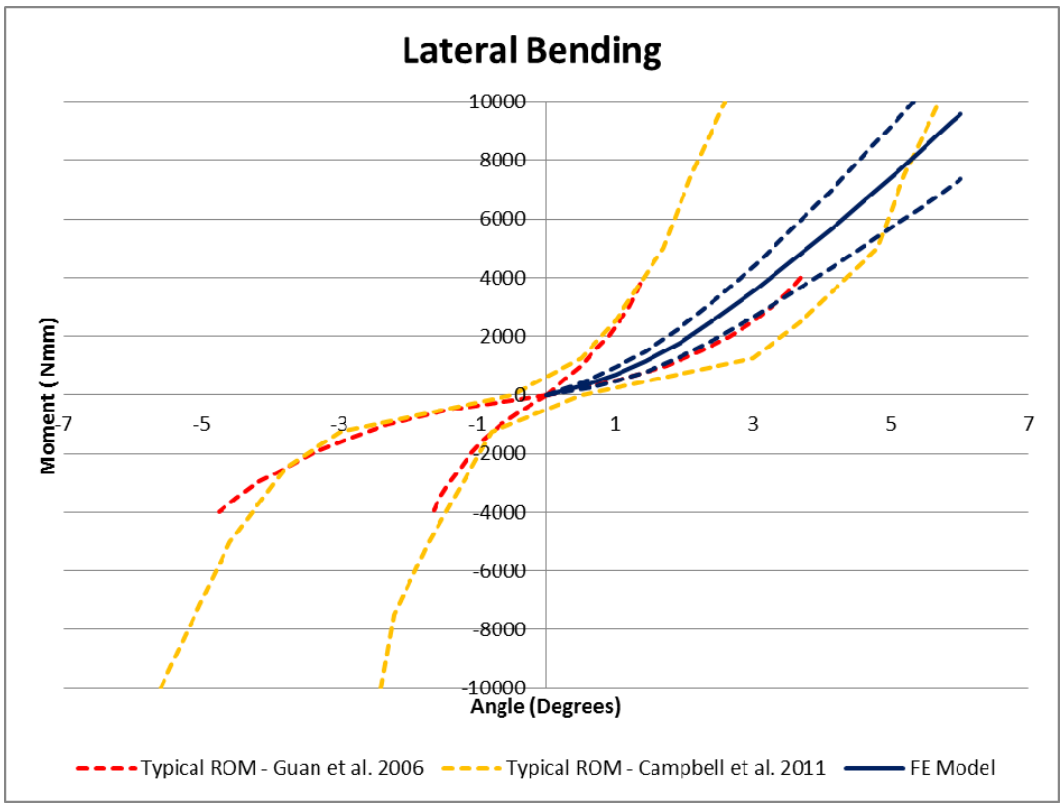

Figure 5.12. Mean torque rotation curves compared to range of curves from literature, lateral bending

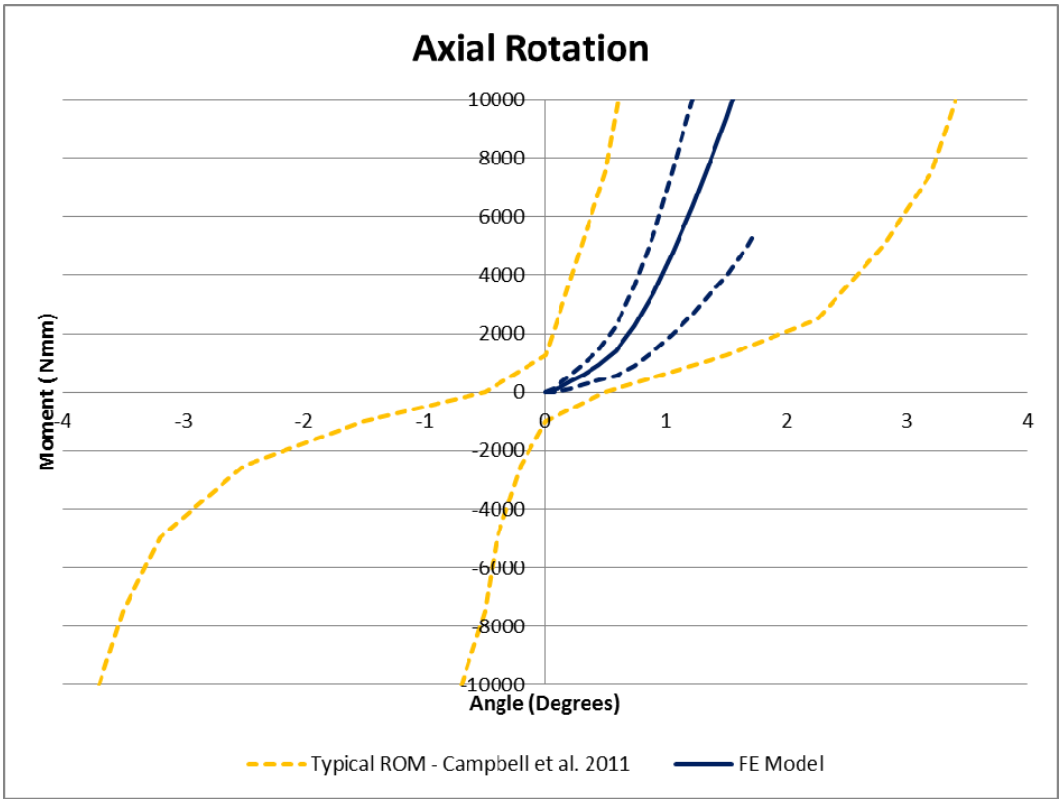

Figure 5.13. Mean torque rotation curves compared to range of curves from literature, axial rotation

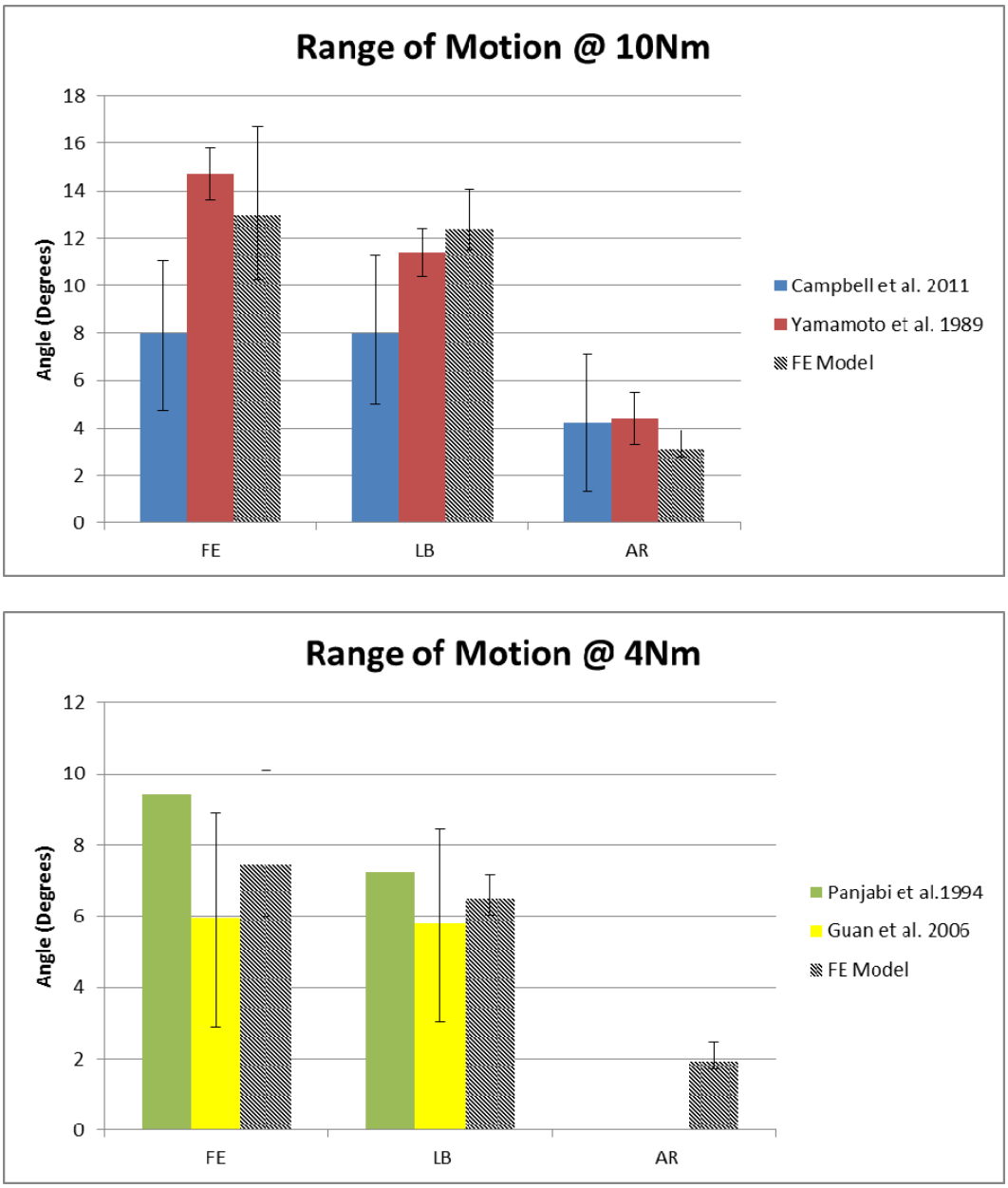

Figure 5.14. Total range of motion compared to literature at 4Nm and 10Nm

Table 5.1. Summary of Input Parameters Representing Ligaments and Annulus Fibrosis (Coombs et al. 2015)

Parameter	Distribution	Mean	Standard Deviation
Ligaments			
ALL Stiffness (N/mm)	Normal	55.39	17.87
PLL Stiffness (N/mm)	Normal	31.30	22.48
LFL Stiffness (N/mm)	Normal	23.23	8.67
FCL Stiffness (N/mm)	Normal	30.60	1.50
ITL Stiffness (N/mm)	Normal	35.35	7.20
ISL Stiffness (N/mm)	Normal	24.68	15.75
SSL Stiffness (N/mm)	Normal	20.55	9.96
Anterior Annulus Fibrosis Holzapfel-Gasser-Ogden parameters			
C10 (MPa)	Lognormal	0.0670	0.050
K1 (MPa)	Normal	1000.0	500.0
K2	Normal	4809.5	2113.9
Posterior Annulus Fibrosis Holzapfel-Gasser-Ogden parameters			
C10 (MPa)	Lognormal	0.134	0.100
K1 (MPa)	Normal	2000.0	1000.0
K2	Normal	5296.3	3208.7
Lateral Annulus Fibrosis Holzapfel-Gasser-Ogden parameters			
C10 (MPa)	Lognormal	0.130	0.100
K1 (MPa)	Normal	1500.0	750.0
K2	Normal	5849.2	3119.7
Annulus Fibrosis Fiber angle from transverse plane			
ϕ	Normal	25.44°	4.22°

Table 5.2. Anatomy comparison of FSU to statistical measurements based on Gilad et al.

Measurement (mm)	FE Model			Gilad et al. 1986		
	L4	L5	Disc	L4	L5	Disc
Inferior A/P width of endplate	32.7	30.5	NA	34.9 ± 2.8	33.9 ± 2.7	NA
Anterior height of vertebral body	28.9	26.2	NA	27.4 ± 2.2	28.3 ± 2.1	NA
Superior A/P width of endplate	31.5	32.4	NA	34.3 ± 2.7	34.2 ± 2.7	NA
Posterior height of vertebral body	27.3	24.0	NA	27.1 ± 2.3	25.7 ± 2.5	NA
Anterior disc height	NA	NA	14.1	NA	NA	12.0 ± 1.8
Posterior disc height	NA	NA	8.23	NA	NA	7.7 ± 1.5

Table 5.3. Uncertainty in the bounds of the reaction moment (Nmm)

Applied Motion	10th Percentile		90th Percentile	
	Upper Bound	Lower Bound	Upper Bound	Lower Bound
Extension	3350.17	3151.02	10301.94	8802.15
Flexion	-35458.76	-37265.38	-20476.12	-22147.70
Axial Rotation	5195.70	4515.15	23919.32	20358.58
Lateral Bending	7442.69	7027.41	13196.23	12035.53

Table 5.4: Sum of Squared Error $(Nm)^2$, Comparison of Descriptive and Sobol Sampling to Random Sampling, Flexion-Extension, Axial Rotation, and Lateral Bending

Sampling Technique	Extension Percentile $(Nm)^2$		Extension Percentile $(Nm)^2$		Axial Rotation Percentile $(Nm)^2$		Lateral Bending Percentile $(Nm)^2$		Total Error $(Nm)^2$
	10^{th}	90^{th}	10^{th}	90^{th}	10^{th}	90^{th}	10^{th}	90^{th}	
Descriptive 25 iterations	0.09	3.22	0.38	4.81	0.58	10.95	1.93	0.25	22.20
Descriptive 50 iterations	0.15	1.31	1.88	1.04	4.28	7.98	0.33	4.91	21.88
Sobol 25 iterations	0.06	6.78	20.07	25.33	2.67	23.48	0.62	1.82	80.85
Sobol 50 iterations	0.04	8.46	9.18	5.15	0.04	14.16	0.56	0.53	38.10

CHAPTER 6 - CONCLUSIONS AND RECOMMENDATIONS

6.1 Conclusion

Calibrating constitutive models of an L4-L5 disc was presented in chapter 3. This calibration process was a more accurate way to define constitutive models for spine disc models by using displacement of intradiscal markers with kinematic data rather than using kinematic data alone. To the author's knowledge, this has not previously been done. A four zone AF was needed to reduce rotational displacement error in addition to the internal displacement error, using a Holzapfel-Gasser-Ogden constitutive model. A linear elastic constitutive model was sufficient to model the NP. These models can be used to more accurately measure strain in the AF. Some potential applications for these models are predicting which activities of daily living could cause a failure of AF tissue, modeling damaged tissue after using suturing techniques for an AF repair, and developing nucleus replacement materials to better match the strain behavior of a healthy disc.

Quantification of uncertainty of the parameters that define the disc and ligaments for an FE model of an L4-L5 FSU was presented in chapter 4, which was based on a comprehensive summary of direct mechanical test measurements across several test specimens. Variability of soft tissue structures has been presented in the literature in FE probabilistic studies. However, it has not been based on a comprehensive summary. Efficient probabilistic analysis of an FE model of the L4-L5 FSU was presented in

chapter 5. Quantification of soft tissue parameter uncertainty represents intersubject variation. The probabilistic representations can be used to perform probabilistic FE studies to assess the variability in output measures such as spine kinematics, implant stress, implant deformation, and other measures. A Monte Carlo simulation was performed using a random sampling technique with 500 iterations. However, descriptive sampling and Sobol sampling, variance reduction sampling techniques, were used to reduce the time required to run a Monte Carlo simulation by 90%. The descriptive sampling technique, with 50 iterations, was the best overall match to the random sampling technique based on the sum of squared error. This allows a more efficient way evaluate spinal implant designs over a population. Model outputs can include stress or strain in the implant, kinematic evaluation for motion preserving implants, and positioning of the implant in the spinal anatomy. Although probabilistic studies have published for the lumbar spine, there have not been studies using a comprehensive representation of all the soft tissue variability while evaluating efficient methods.

Using the Holzapfel Ogden Gasser constitutive model to represent the AF is a novel approach which was applied throughout all topics in this dissertation. Several other FE models of the lumbar disc have been developed with discrete elements representing the fibers in the AF. Using the Holzapfel Ogden Gasser model enabled fiber stiffness and orientation parameters to be used in optimization, Monte Carlo, and sensitivity studies. The fiber orientation could not be included with models using discrete elements unless the mesh was redefined for each iteration.

6.2 Future Work

As discussed in chapter 3, there are several limitations in the process presented to calibrate constitutive models of the NP and AF using displacement data of intradiscal points across the mid-transverse plane of a level 4-5 lumbar spine disc. This study was based on one specimen. It would be much more robust to use several specimens and determine a range of parameter values that define the constitutive models. Constitutive models could also be determined for degenerated discs. Tsantrizos et al. (Tsantrizos et al., 2005) tested several healthy and several degenerated spines of varying Thomson grades. Three dimensional displacement data may improve calibration which has been experimentally collected (Costi et al., 2007). The disc model assumed flat end plates with a lordotic angle. However, if further testing could be performed, three dimensional geometry of the disc could be obtained and modeled. MRI data could be used to segment the actual 3 dimensional geometry. The angles of the discs were measured after the load was applied. If further testing could be performed, the rotation should be measured as the loads are applied and the torque-rotation curves could be used to improve the calibration. The calibration process could be expanded to include the fiber dispersion and fiber angle, which would add two more parameters to each AF zone.

Chapter 4 discusses the uncertainty quantification of parameters that define soft tissue structures of the L4-L5 FSU. However, there was little data reported for the ITL and it was based on thoracic specimens. Further testing could be conducted on ITL specimens. It has been reported that the ITL is not a significant contributing ligament for spine biomechanics (White and Panjabi, 1990). However, based on the results from the sensitivity study in chapter 5, the lateral bending reaction moments are more sensitive to

the ITL stiffness than other ligaments, but not as much as other structures such as lateral quadrant of the disc or the angle of the annular fibers.

Chapter 5 discussed efficient probabilistic methods using an FE model of an FE model of an L4-L5 FSU. Range of motion was compared to literature, but this model could also be used to compare the strains in the ligaments to strains reported by White and Panjabi (White and Panjabi, 1990). The parameters used to define the AF and NP constitutive models were treated independently. The number of parameters could be reduced by relating the uncertainty of the parameters to a single standard normal variate. However, the data presented in the literature in chapter 4 did not contain enough information to make that determination. The specimens from each location of the AF were not grouped by donors. Further testing would need to be done. The benefit would be less input parameters and possibly using other probabilistic methods like the Most Probable Point (MPP) and the Mean Value (MV) method to perform Monte Carlo simulations (Haldar and Mahadevan, 2000). Finally, the uncertainty of boney anatomy, including facet position and orientation, could be incorporated in the probabilistic study. This would be the most logical next step since work has been done on statistical shape modeling of the boney anatomy of lumbar spine (Campbell et al., 2014, Hollenbeck et al., 2013).

LIST OF REFERENCES

Abaqus Users Guide (release 6.12), 2012, Simulia, Dessault Systemes, Hyperelastic behavior of rubberlike materials, Chapter 22.5.1

Adams, M.A., Freeman, B.J., Morrsion, H.P., Nelson, I.W., Dolan, P., 2000. Mechanical initiation of intervertebral disc degeneration. Spine 1, 1625-36.

Ahmad, Z., Akramin, M., 2010. Probabilistic stress analysis of the human lumbar spine extended finite element method. The 14th Asia Pacific Regional Meeting of International Foundation for Production Research, Melaka, December 7-10.

Ayturk, U., Puttlitz, C., 2011. Parametric convergence sensitivity and validation of a finite element model. Comput Methods Biomech Biomed Engin 14, 695-705.

Baldwin, M., Laz, P., Stowe, J., Rullkoetter, P., 2009. Efficient probabilistic representation of tibiofemoral soft tissue constraint. Computer Methods in Biomechanics and Biomedical Engineering 12, 651-659.

Barnes, K., Armstrong, J., Agarwala, A., Petrella, A., 2011. Probabilistic study of a lumbar motion segment: sensitivity to material and anatomic variability. ASME 2011 Summer Bioengineering Conference, Parts A and B, Farmington, Pennsylvania, USA, June 22–25, Paper No. SBC2011-53846, 863-864.

Bono C., Khandha, A., Vadapalli, S., Holekamp, S., Goel, V., Garfin, SR., 2007. Residual sagittal motion after lumbar fusion: a finite element analysis with implications on radiographic flexion-extension criteria. Spine (Phila Pa 1976) 32, 417-22.

Bowden, A., Guerin, H., Villarraga, M., Patwardhan, A., Ochao, J., 2008. Quality of motion considerations in numerical analysis of motion restoring implants of the spine. Clin Biomech 23, 536-44.

Burhenne, S., Jacob, D., Henze, G., 2011. Sampling based on Sobol sequences for Monte Carlo techniques applied to building simulations. In Proceedings of the 12th Conference of International Building Performance Simulation Association, Sydney.

Campbell, J.Q., Yoder, A.J., Patrella, A.J., 2014. An automated method for feature extraction and subject specific finite element modeling of the lumbar spine. 7th World Congress of Biomechanics, Boston, MA.

Campbell, JR., Imsdahl, S., Ching, RP., 2012. Evaluation of a synthetic L2-L5 spine model for biomechanical testing. In Proceeding of Canadian Biomechanics Society, Vancouver, BC, Canada.

Chazal, J., Tanguy, M., Bourges, M., Gaurel, G., Escande, G., Guilot, M., Vanneuville, G., 1985. Biomechanical properties of spinal ligaments and a histological study of the supraspinal ligament in traction. Journal of Biomechanics 18, 167-176.

Chiang, M., Zhong, Z., Chen, C., Cheng, C., Shih, S., 2006. Biomechanical Comparison of Instrumented Posterior Lumbar Interbody Fusion With One or Two Cages by Finite Element Analysis. Spine 31, E682–E689.

Coombs, D. J., Bushelow, M., Laz, P. J., Rao, M., Rullkoetter, P. J., 2013. Stepwise validated finite element model of the human lumbar spine. Proceedings of the ASME 2013 Conference on Frontiers in Medical Devices: Applications of Computer Modeling and Simulation Washington, DC, USA.

Coombs, D. J., Rullkoetter, P. J., Laz, P. J., 2015. Quantifying variability in lumbar L4 L5 soft tissue properties for use in FE analysis. ASME Journal of Verification, Validation, and Uncertainty Quantification. in review.

Costi, J.J., Sokes, I.A., Gardner-Morse, M., Laible, J.P., Scoffone, H.M., Iatridis, J.C., 2007. Direct measurement of intervertebral disc maximum shear strain in six degrees of freedom: Motions that place disc tissue at risk of injury. J Biomech 40, 2457–2466.

Guterl, C.C., See, E.Y., Blanquer, S.B.G., Pandit, A., Ferguson, S.J., Benneker, L.M., Grijpma, D.W., Sakai, D., Eglin, D., Alini, M., Iadridis, J.C., Grad, S., 2013. Challenges and strategies in the repair of ruptured annulus fibrosis. European Cells and Materials, 25, 1-21.

Dessault Systemes Simulia Corp., Johnston, RI. 2011. Abaqus 6.12 Analysis User's Manual, 2012. Section 22.5.1 Hyperelastic Behavior of Rubberlike Materials and Section 22.5.3 Anisotropic hyperelastic behaviour.

de Visser, H., Adam, C., Crozier, S., Pearcy, M., 2007. The role of quadratus lumborum asymmetry in the occurrence of lesions in the lumbar vertebrae of cricket fast bowlers. Medical Engineering & Physics 29, 877-885.

Dolan, P., Earley, M., Adams, M.A., 1994. Bending and compressive stresses acting on the lumbar spine during lifting activities. J Biomech 27, 1237-48.

Dooris, A., Goel, V., Grosland, N., Gilbertson, L., Wilder, D., 2001. Load-Sharing Between Anterior and Posterior Elements in a Lumbar Motion Segment Implanted With an Artificial Disc. Spine 26, E122-E129.

Dooris, A.P., 2001. Experimental and Theoretical Investigations into the effects of artificial disc implantation on the lumbar spine [dissertation]: University of Iowa.

Ebara, S., Iatridis, J., Setton, L., Foster, R., Mow, V., Weidenbaum, M., 1996. Tensile Properties of Nondegenerate Human Lumbar Anulus Fibrosis. Spine 21, 452-461.

Eberlein, R., Holzapfel, G., Frohlich, M., 2004. Multi-segment FEA of the human lumbar spine including the heterogeneity of the annulus fibrosus. Computational Mechanics 34, 147-163.

Elliott, D.M., Setton, L.A., 2001. Anisotropic and inhomogeneous tensile behavior of the human annulus fibrosus: experimental measurement and material model predictions. J Biomech E 123, 256–263.

Ezquerro, F., Simon, A., Prado, M., Perez, A., 2004. Combination of finite element modeling and optimization for the study of lumbar spine biomechanics considering the 3D thorax–pelvis orientation. Medical Engineering & Physics 26, 11-22.

Ezquerro, F., Vacas, G., Postigo, S., Prado, M., Simon, A., 2011. Calibration of the finite element model of a lumbar functional spinal unit using an optimization technique based on differential evolution. Medical Engineering & Physics 33, 89-95.

Fok, J., 2009. Application of a Biomechanical Finite Element Spine Model to the Vicious Cycle Scoliosis Growth Theory: Evaluation of Improved FEA Geometry and Material Assignment [dissertation]. Edmonton (AB, Canada): University of Alberta.

Fujita, Y., Duncan, N., Lotz, J., 1997. Radial tensile properties of the lumbar annulus fibrosis are site and degeneration dependent. Journal of Orthopaedic Research 15, 814-819.

Gasser, T., Ogden, R., Holzapfel, G., 2006. Hyperelastic modelling of arterial layers with distributed collagen fibre orientations. J R Soc Interface 3, 15–35.

Gerhard, A., Holzapfel, G., Gasser, T., 2000. A New Constitutive Framework for Arterial Wall Mechanics and a Comparative Study of Material Models. J Elasticity 61, 1–48.

Gilad, I., Nissan, M., 1986. A study of vertebra and disc geometric relations of the human cervical and lumbar spine, Spine (Philadelphia Pa 1976) 11, 154-157.

Goel, V., Grauer, J., Patel, T., Biyani, A., Sairyo, K., Vishnubhatla, S., Matyas, A,. Cowgill, I., Shaw, M., Long, R., Dick, D., Panjabi, M., Serhan, H., 2005. Effects of Charite artificial disc on the implanted and adjacent spinal segments mechanics using a hybrid testing protocol. Spine (Philadelphia Pa 1976) 30, 2755-2764.

Guan, Y., Yoganandan, N., Moore, J., Pintar, F., Zhanga, J., Maimana D., Laud, P., 2006. Moment–rotation responses of the human lumbosacral spinal column. Journal of Biomechanics 40, 1975–1980.

Guan, Y., Yoganandan, N., Zhang, J., Pintar, F.A., Cusick, J.F., Wolfla, C.E., Maiman, D.J., 2006. Validation of a Clinical Finite Element Model of the Human Lumbosacral Spine. Med Biol Eng Comput 44, 633-41.

Guerin, H., Elliott, D., 2006. Degeneration affects the fiber reorientation of human annulus fibrosus under tensile load. Journal of Biomechanics 39, 1410–1418.

Guerin, H.A., Elliott, D.M., 2006. Spine Technology Handbook. Elsevier Academic Press, Amsterdam/Boston. Chapter 3, Structure and properties of soft tissues in the spine; p. 35-62.

Haldar, A., Mahadevan, S., 2000. Probability, Reliability and Statistical Methods in Engineering Design, John Wiley & Sons, Inc., New York.

Hollenbeck, J.F.M., Rullkoetter, P.J., Cain, C., Fitzpatrick, C.K., Laz, P.J., 2013. Statistical shape and alignment modeling of the lumbar spine, ASME Summer Bioengineering Conference, Sunriver, Oregon.

Holzapfel, G. A., T. C. Gasser, R. W. Ogden, 2000. A New Constitutive Framework for Arterial Wall Mechanics and a Comparative Study of Material Models. Journal of Elasticity 61, 1–48.

Holzapfel, G. A., Schulze-Bauer, C. A., Feigl, G., Regitnig, P., 2005. Single lamellar mechanics of the human lumbar anulus fibrosus. Biomechan Model Mechanobiol 3, 125–140.

Humphreys S. and Eck, J., 1999. Clinical Evaluation and Treatment Options for Herniated Lumbar Disc. American Family Physician 59, 575-582.

Iida, T., Abumi, Kotani, Y., Kaneda, K., 2002. Effects of aging and spinal degeneration on mechanical properties of lumbar supraspinous and interspinous ligaments. The Spine Journal 2, 95–100.

Ingber, L., 1993. Simulated Annealing: Practice versus Theory. Mathematical Computer Modeling 18, 29-57.

Isight Component Guide (release 5.7), Simulia, Dessault Systemes, pp 561-562.

Kurtz, Steven M. Edidin, Avram A., 2006. Spine Technology Handbook, Elsevier Academic Press, Burlington, MA.

Lee, K.K., Teo, E.C., 2005. Material sensitivity study on lumbar motion segment (L2-L3) under sagittal plane loadings using probabilistic method. J Spinal Disord Tech 18, 163-170.

Lu, Y., Hutton, W., Gharpuray, V., 1996. Do bending, twisting, and diurnal fluid changes in the disc affect the propensity to prolapse? A viscoelastic finite element model. Spine (Philadelphia Pa 1976) 21, 2570-2579.

Marras, W.S., Lavender, S.A., Leurgans, S.E., Rajulu, S.L., Allread, W.G., Fathallah, F.A., Ferguson, S.A., 1993. The Role of Dynamic Three-Dimensional Trunk Motion in Occupationally-Related Low Back Disorders. Spine 18, 617-628.

Miller, J.A., Schmatz, D., Schultz, A.B., 1988. Lumbar disc degeneration: correlation with age, sex, and spine level in 600 autopsy specimens. Spine 13, 173.

Neumann, P., Keller, T.S., Ekstrom L., Perry L., Hansson, T. H., Spengler, M., 1992. Mechanical Properties of the human lumbar anterior longitudinal ligament. Journal of Biomechanics 25, 1185-1194.

O'Connell, G., Guerin, H., Elliott, D., 2009. Theoretical and uniaxial experimental evaluations of human annulus fibrosis degeneration. Journal of Biomechanical Engineering 131, 111007-1 - 111007-7.

Panjabi, M.M., Greenstein, G., Duranceau, J., Nolte, L.P., 1991. Three-dimensional quantitative morphology of lumbar spinal ligaments. Journal of Spinal Disorders 4, 54-62.

Panjabi M., Oxland T., Yamamoto I., Crisco J., 1994. Mechanical behavior of the human lumbar and lumbosacral spine as shown by three-dimensional load-displacement curves. The Journal of Bone & Joint Surgery 76, 413-424.

Pintar, F. A., Yoganandan, N., Myers, T., Elhagediab, A., Sances, A. Jr., 1992. Biomechanical properties of human lumbar spine ligaments. Journal of Biomechanics 25, 1351-1356.

Polikeit, A., Nolte, LP., Ferguson, J., 2003. The effect of cement augmentation on the load transfer in an osteoporotic functional spinal unit: finite-element analysis. Spine (Philadelphia Pa 1976) 28, 991-996.

Rao, M., 2012. Explicit finite element modeling of the human lumbar spine. PhD. Thesis, Electronic Theses and Dissertations. Paper 906. University of Denver

Rao, M., Patrella, A., Baldwin, M., Laz, P., Rullkoetter, P., 2009. Efficient Probabilistic Finite Element Modeling for Evaluation of Spinal Mechanics, 2009. In Proceeding of the 55th Annual Meeting of the Orthopedic Research Society, Las Vegas, NV.

Robertson, D., Willardson, R., Parajuli, D., Cannon, A., Anton, E., 2013. The lumbar supraspinous ligament demonstrates increased material stiffness and strength on its ventral aspect. Journal of the mechanical behavior of biomedical materials 17, 34–43.

Rohlmann, A., Boustani, H., Bergmann, G., Zander, T., 2010. A probabilistic finite element analysis of the stresses in the augmented vertebral body after vertebroplasty. Eur Spine J 19, 1585–1595.

Rohlmann, A., Mann, A., Zander T., Bergmann, G., 2009. Effect of an artificial disc on lumbar spine biomechanics: a probabilistic finite element study. Eur Spine J 18, 89–97.

Rohlmann, A., Zander, T., Bergmann, G., 2005. Effect of Total Disc Replacement with ProDisc on Intersegmental Rotation of the Lumbar Spine. Spine 30, 738-743.

Rohlmann, A., Zander, T., Schmidt, H., Wilke, H., Bergmann, G., 2006. Analysis of the influence of disc degeneration on the mechanical behaviour of a lumbar motion segment using the finite element method. Journal of Biomechanics 39, 2484–2490.

Saliby, E., 1990. Descriptive sampling: A better approach to Monte Carlo simulation. The Journal of the Operational Research Society 41, 1133-1142.

Shapiro, I.M., Risbud, M.V., 2014. The Inervertebral Disc – Molecular and Structural Studies of the Disc in Health and Disease, Springer, New York.

Schmidt, H., Heuer, F., Simon, U., Kettler, A., Rohlmann, A., Claes, L., Wilke, H., 2006. Application of a new calibration method for three-dimensional finite element model of a human lumbar annulus fibrosis. Clin Biomech 21, 337-44.

Schmidt, H., Heuer, F., Drumm, J., Klezl, Z., Claes, L., Wilke, H., 2007. Application of a calibration method provides more realistic results for a finite element model of a lumbar spinal segment. Clinical Biomech 22, 377-84.

Schmidt, H., Kettler, A., Heuer, F., Simon, U., Claes, L., PhD, Wilke, H., 2007. Intradiscal Pressure, Shear Strain, and Fiber Strain in the Intervertebral Disc under Combined Loading. Spine 32, 748 –755.

Schmidt, H., Kettler, A., Rohmann, A., Claes, L., Wilke, H.J., 2007. The risk of disc prolapses with complex loading in different degrees of disc degeneration – A finite element analysis. Clinical Biomech 22, 988-98.

Shirazi-Adl, A., 1989. Strain in fibers of a lumbar disc. Analysis of the role of lifting in producing disc prolapse. Spine 14, 96-103.

Smit. T., 1996. The Mechanical Significance of the Trabecular Bone Architecture in a Human Vertebra [dissertation]. Berlin (Germany): Technische Univeritat.

Thacker, B., Nicolella, D., Kumaresan, S., Yoganandan, N., Pintar, F., 2001. Probabilistic finite element analysis of the human lower cervical spine. American Society of Mechanical Engineers, Bioengineering Division (Publication) BED01/2000; 48, 237-238.

Tsantrizos, A., Ito, K., Aebi, M., Steffen, T., 2005. Internal strains in healthy and degenerated lumbar intervertebral discs. Spine 30, 2129-37.

Tsuang, Y.H., Chiang, Y.F., Hung, C.Y., Wei, H.W., Huang, C.H., Cheng, C.K., 2009. Comparison of cage application modality in posterior lumbar interbody fusion with posterior instrumentation - A finite element study. Med Eng Phys 31, 565-70.

Venkataraman, P., 2009. Applied Optimization with Matlab Programming. John Wiley and Sons, New Jersey.

Vadapalli, S., Sairyo, K., Goel, V., Robon, M., Biyani, A., Khandha, A., Ebraheim, N., 2006. Biomechanical Rationale for Using Polyetheretherketone (PEEK) Spacers for Lumbar Interbody Fusion–A Finite Element Study. Spine 31, E992-E998.

Wagner, D., Lotz, J., 2004. Theoretical model and experimental results for the nonlinear elastic behavior of human annulus fibrosus. Journal of Orthopaedic Research 22, 901–909.

White, A., Panjabi, M., 1990. Clinical Biomechanics of the Spine, Lippincott Williams & Wilkins.

Wong, C., Gehrchen, P.M., Darvann, T., Kiaer, T., 2003. Nonlinear Finite-Element Analysis and Biomechanical Evaluation of the Lumbar Spine. IEEE T Med Imaging 22, 742-746.

Xiao, Z., Wang, L., Gong, H., Zhu, D., 2012. Biomechanical evaluations of three surgical scenarios of posterior lumbar interbody fusion by finite element analysis. Biomedical Engineering Online 11, 31.

Yamamoto, I., Panjabi, M., Crisco, T., Oxland, T., 1989. Three-dimensional movements of the whole lumbar spine and lumbosacral joint. In Proceeding of the 12th Annual Meeting of the International Congress of Biomechanics, Los Angeles, CA.

Zhong, Z., Chen, S., Hung, C., 2009. Load and displacement controlled finite element analyses on fusion and non-fusion spinal implants. Engineering in Medicine 223, 143-157.